NUMERICAL SIMULATIONS OF ION TRANSPORT MEMBRANE OXY-FUEL REACTORS FOR CO_2 CAPTURE APPLICATIONS

by

Jongsup Hong

M.S. Mechanical Engineering
Massachusetts Institute of Technology, 2009
B.S. Mechanical Engineering
Seoul National University, 2007

SUBMITTED TO THE DEPARTMENT OF MECHANICAL ENGINEERING IN PARTIAL FULFILLMENT OF THE REQUIREMENTS FOR THE DEGREE OF

DOCTOR OF PHILOSOPHY IN MECHANICAL ENGINEERING
AT THE
MASSACHUSETTS INSTITUTE OF TECHNOLOGY

JUNE 2013

Signature of Author ....
Department of Mechanical Engineering
February 28, 2013

Certified by......................   ....
Ahmed F. Ghoniem
Ronald C. Crane Professor
Thesis Supervisor

Accepted by..
Dave E. Hardt
Chairman, Department Committee on Graduate Students

Page left intentionally blank

NUMERICAL SIMULATIONS OF ION TRANSPORT MEMBRANE OXY-FUEL REACTORS FOR CO_2 CAPTURE APPLICATIONS

by

Jongsup Hong

Submitted to the Department of Mechanical Engineering
on February 28, 2013 in partial fulfillment of the
requirements for the degree of Doctor of Philosophy in
Mechanical Engineering

ABSTRACT

Numerical simulations were performed to investigate the key features of oxygen permeation and hydrocarbon conversion in ion transport membrane (ITM) reactors. ITM reactors have been suggested as a novel technology to enable air separation and fuel conversion to take place simultaneously in a single unit. Possessing the mixed ionic and electronic conductivity, perovskite membranes or ion transport membranes permeate selectively oxygen ions from the air (feed) side to the sweep gas or reactive gas (permeate) side of the membrane, driven by the oxygen chemical potential gradient across the membrane at elevated temperature. When a fuel such as methane is introduced into the permeate side as a sweep gas, hydrocarbon oxidation reactions occur by reacting the fuel with the permeated oxygen. The fuel can be partially reformed, completely oxidized or converted to produce higher hydrocarbons. To utilize this technology more effectively, it is necessary to develop a better understanding of oxygen transport and hydrocarbon conversion in the immediate vicinity of the membrane or on its surface. In this thesis, a planar, finite-gap stagnation flow configuration was used to model and examine these processes.

A spatially resolved physical model was formulated and used to parameterize an oxygen permeation flux expression in terms of the oxygen concentrations at the membrane surface given data on the bulk concentration. The parameterization of the permeation flux expression is necessary for cases when mass transfer limitations on the permeate side are important and for reactive flow modeling. At the conditions relevant for ITM reactor operation, the local thermodynamic state should be taken into account when the oxygen permeation rate is examined, which has been neglected. To elucidate this, the dependency of oxygen transport and fuel conversion on the geometry and flow parameters including the membrane temperature, air and sweep gas flow rates, oxygen concentration in the feed air and fuel concentration in the sweep gas was discussed.

The reaction environment on the sweep side of an ITM was characterized. The spatially resolved physical model was used to predict homogeneous-phase fuel conversion processes and to capture the important features (e.g., the location, temperature, thickness and structure of a flame) of laminar oxy-fuel diffusion flames stabilized on the sweep side. The nature of oxygen permeation does not enable pre-mixing of fuel and oxidizer (i.e., sweep gas and permeated oxygen), establishing non-premixed flames. In oxy-fuel combustion applications, the sweep side is fuel-diluted with CO_2 or/and H_2O, and the entire unit is preheated to achieve a high oxygen permeation flux. This study focused on the flame structure under these conditions and specifically on the chemical effect of CO_2 dilution.

The interactions between oxygen permeation and homogeneous-phase fuel oxidation reactions on the sweep side of an ITM were examined. Within ITM reactors, the oxidizer flow rate, i.e., the oxygen permeation flux, is not a pre-determined quantity, since it depends on the oxygen partial pressures on the air and sweep sides and the membrane temperature. Instead, it is influenced by the hydrocarbon oxidation reactions that are also dependent on the oxygen permeation rate, the initial conditions of the sweep gas, i.e., the fuel concentration, flow rate and temperature, and the diluent. A parametric study with respect to key operating conditions, which include the fuel concentration in the sweep gas, its flow rate and temperature and the geometry, was conducted to investigate their interactions.

The catalytic kinetics of heterogeneous oxygen surface exchange and fuel oxidation for a perovskite membrane in terms of the thermodynamic state in the immediate vicinity of or on the membrane surface was investigated. Perovskite membranes have been shown to exhibit both oxygen perm-selectivity and catalytic activity for hydrocarbon conversion. However, a description of their catalytic surface reactions is still required. The kinetic parameters for heterogeneous oxygen surface exchange and catalytic fuel conversion reactions were inferred, based on permeation rate measurements and a spatially resolved physical model that incorporates detailed chemical kinetics and transport in the gas-phase. It is shown that the local thermodynamic state at the membrane surface should be accounted for when constructing and examining membrane permeation and heterogeneous chemistry. The significance of modeling both homogeneous and heterogeneous chemistry and their coupling when examining the results was discussed.

Thesis Supervisor: Ahmed F. Ghoniem
Title: Ronald C. Crane Professor

Acknowledgements

First of all, I would like to thank my thesis supervisor, Professor Ahmed Ghoniem, for his invaluable advice and consistent support for my PhD research. He has been always ensuring that I am on the right path and convincing me to have full of confidence. It has truly been a great honor and pleasure to work with him.

I am also grateful to Professor Patrick Kirchen for his advice, expertise and support. As a thesis committee member and friend, he has provided essential information whenever I needed inputs from others. His insights nourished my research. I would like to thank the rest of my thesis committee members, Professor Martin Bazant, Professor Alexander Mitsos and Professor Rached Ben Mansour for their critical advice and encouraging comments.

I would like to gratefully acknowledge the Kwanjeong Educational Foundation Scholarship for their generous support. King Fahd University of Petroleum and Minerals is also greatly recognized for their support.

I could not have made this work without my family's encouragement, love and support. Although I have been far away from them, they made me feel not being alone and helped me to concentrate on my research.

There are countless friends whom I counted on and shared my difficult time with: Wonyong Lee, Seunghyuk Hong, Wonjoon Choi, Jaehyung Kim, Sungmin Kim, Jaewon Cha, Sangwon Byun, Sungjoong Kim, Dongkun Lee, Howon Lee, Sungho Lee, Jooeun Ahn, Hyunglae Lee, Kushal Kedia, Lei Chen, Ray Speth, Jeff Hanna, Simcha Singer, Anton Hunt, Daniel Apo, Lorraine Rabb, and all Reacting Gas Dynamics laboratory members. I am deeply glad that I have these amazing people on my side. Thank you, all!

Page left intentionally blank

Contents

List of Figures

List of Tables

Page left intentionally blank

Chapter 1 Introduction

1.1. Motivation

Carbon capture and sequestration have been considered as important options for combating the rise of carbon dioxide concentration in the atmosphere. These technologies, as shown in **Figure 1-1**, require additional equipment and advanced processes that are cost- and energy- intensive. All carbon capture solutions need extra capital investments as well as advanced technologies [1-5]. Post-combustion capture requires massive amounts of chemicals and separation technologies that lead to significant efficiency penalties. Pre-combustion capture, using technologies such as reforming and gasification, is considered most suitable for solid fossil fuels and heavy hydrocarbons, but needs air separation units, gasifiers, reformers, and syngas treatment units. On the other hand, oxy-fuel combustion capture, which is an appropriate technology for lighter hydrocarbons and both solid and gaseous (or gasified) fossil fuels, enables the least efficiency penalty and cost effectiveness [6].

In oxy-fuel combustion, fuels are burned in a nitrogen-lean (ideally nitrogen-free) carbon dioxide/water-rich stream [6], which is achieved by feeding the reactor with an oxygen-enriched stream (i.e., oxygen separated from the air prior to combustion) and recycled flue gases [7]. The recycled gases are used to control the flame temperature [8]. Oxy-fuel combustion yields flue gases consisting of predominantly carbon dioxide and condensable water, whereas conventional air-fired combustion flue gases are nitrogen-rich with only about 15% (by volume) carbon dioxide [9, 10]. Condensing out water and cleaning up the flue gas using de-SO_x and de-NO_x processes, oxy-fuel combustion produces a carbon dioxide stream ready for transportation to an enhanced oil recovery or a sequestration site. The high carbon dioxide concentration and the significantly lower nitrogen concentration in the oxy-fuel flue gases is a unique feature that lowers the energy and capital costs of oxy-fuel carbon dioxide capture when compared to alternatives [11].

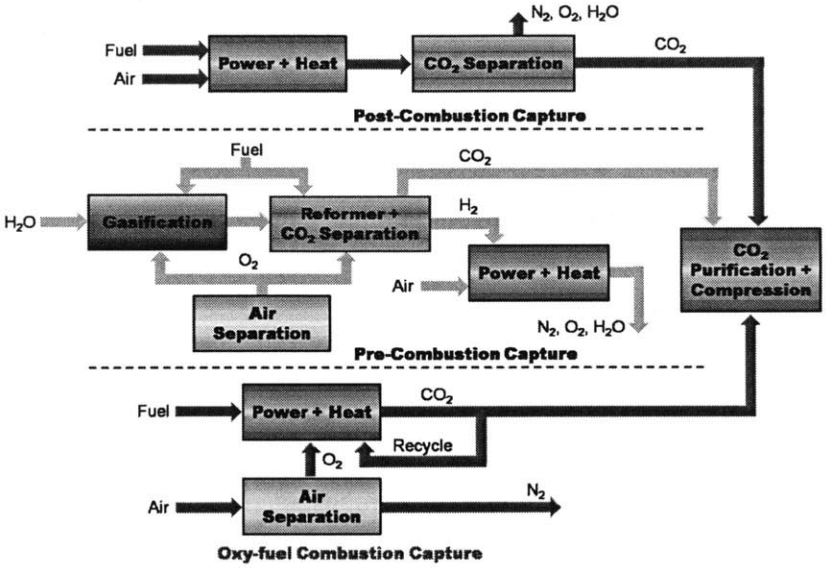

Figure 1-1 Carbon capture and sequestration technologies

To enable oxy-fuel combustion, oxygen is separated from air prior to combustion using an air separation unit. Currently, cryogenic distillation technology is the only option available for large-scale fossil-fueled power plants. However, this technology requires energy six times that of the ideal separation energy as well as large capital expenditure. Moreover, they are bulky and difficult to integrate with the rest of the power plants because of the complex thermal integration required for multi-step distillation [6]. In this thesis, a novel approach incorporating membrane technology for air separation is investigated.

Dense ceramic membranes with high ambipolar (ionic and electronic) conductivities have been proposed for separating oxygen from air. At elevated temperatures, typically above 700 °C [12], and oxygen partial pressure gradients across the membranes, oxygen ions selectively permeate from the air (feed) side to the sweep gas (permeate) side. Integrated at the front end of the power plant, the membrane unit may use a hot recycled CO_2 stream as a sweep gas on the permeate side to maintain the requisite partial pressure gradient and hence drive the oxygen permeation process. Since the 1980s when these mixed-conducting ceramic membranes were introduced [13-19], extensive research has been conducted to improve oxygen permeation rates. For this membrane technology to become more viable for air separation, control of these two factors while maintaining mechanical, thermal, and chemical stability is necessary.

To enhance oxygen permeation rates, reactive sweep gases or dilute fuel stream can be fed into the permeate side, promoting consumption of the permeated oxygen through oxidation reactions. In these configurations, as shown in **Figure 1-2**, oxygen permeation rate and hydrocarbon conversion/product selectivity are strongly coupled through the local oxygen partial pressure at the membrane surface on the permeate side, as well as the membrane temperature [20]. Given the membrane temperature and sweep gas inlet conditions, oxygen consumption maintains large partial pressure gradients, leading to increased oxygen permeation rates [20]. In addition, the heat of reaction reduces the heat input needed to maintain a sufficiently high temperature within the reactor. Larger permeation rates attributed to oxidation reactions in the permeate side of the mixed-conducting membranes result in smaller volume membrane reactors to be used for the same application.

In this regard, studies should be conducted to investigate key features related to oxygen permeation and hydrocarbon conversion processes within an ITM reactor. Most current research is focused on permeation measurements and membrane developments for the reducing environment. However, it is important to understand the coupled physical and chemical processes within the membrane reactors in order to improve their effectiveness. In-depth knowledge of these processes enables us to control fuel conversion through manipulating the hydrocarbon-oxygen ratio at the optimal operating conditions, and to achieve the desired reactor design. To meet these needs, I have conducted the detailed analysis of ITM reactors by using numerical simulations.

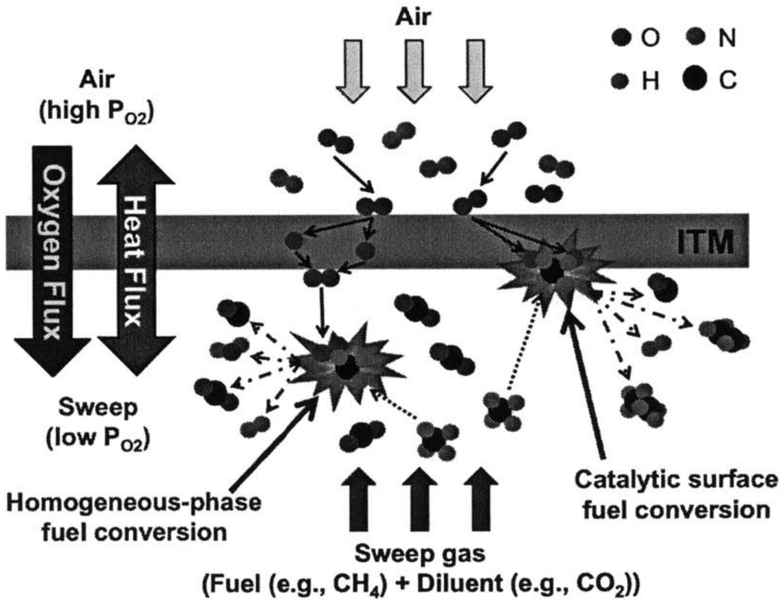

Figure 1-2 Ion transport membrane (ITM) for air separation and fuel conversion in the absence of nitrogen. Oxygen selectively permeates from the air side to the sweep side of an ITM. On the sweep side, fuel conversion takes place in a nitrogen-free environment, as the fuel approaches the membrane while the permeated oxygen transports in the opposite direction.

1.2. Background

1.2.1. Oxygen permeation

Dense and gas-tight mixed ionic-electronic conducting ceramic membranes allow only oxygen ions to move across them. Because they are gas-tight, the direct permeation of oxygen molecules is prohibited. When both the ionic and electronic conductivities are sufficiently high, oxygen ion transport through the membranes is possible, without the need of an external electrical circuit. The permeation of oxygen ions is charge compensated by a flux of electrons. The movement of these oxygen ions is driven by the difference in oxygen partial pressures across the membranes at an appropriate temperature [12]. Thus, in general, it is desirable to maximize ionic and electronic conductivities of the ITM, while maintaining proper oxygen partial pressure gradients and membrane temperature.

Based on the partial pressure difference, the membrane temperature and its ambipolar conductivity, oxygen migrates from the high pressure feed side to the low pressure permeate side, according to the overall transport processes summarized as follows [21-24]:

i. Gaseous oxygen mass transfer from the feed stream to the membrane
ii. Adsorption to the membrane and dissociation of oxygen molecules to lattice oxygen ions (surface exchange)
iii. Transport of lattice oxygen ions through the membrane (bulk diffusion)
iv. Association of lattice oxygen ions to oxygen molecules and desorption from the membrane (surface exchange)
v. Gaseous oxygen mass transfer from the membrane to the permeate stream

The gaseous mass transfer processes (i and v) can be modeled using homogenous gas species conservation equations (mass, momentum, and energy). The law of mass action, with reaction rates based on activation energy, temperature, and kinetic parameters, can be used to approximate the oxygen surface exchange kinetics (ii and iv) [25-29]. Charged-species transport mechanism shown below enables us to model the oxygen ion transport within the membranes (commonly termed bulk diffusion) [12, 30-36]:

$$J_i = -\frac{\sigma_i}{(z_i F)^2} \nabla \eta_i \qquad \textbf{Eq. 1-1}$$

where J_i is the flux of the charged-species i through the membrane; σ_i is the ionic conductivity of charged-species i; z_i is the charge number of charged-species i; F is the Faraday constant; $\nabla \eta_i$ is the electrochemical potential gradient of charged-species i. When gaseous oxygen molecules approach the feed side membranes, they adsorb onto the membranes and are dissociated/ionized to oxygen ions by available free electrons from the lattice, resulting in occupation of an oxygen vacancy and the formation of two electron holes [37]:

$$V_O^{\bullet\bullet} + \frac{1}{2} O_2 \leftrightarrow O_O^x + 2h^\bullet \qquad \textbf{Eq. 1-2}$$

where $V_O^{\bullet\bullet}$ is an oxygen vacancy; O_O^x stands for a lattice oxygen ion; $h^\bullet$ represents an electron hole. These oxygen ions are incorporated into the lattice structure and transported through the membranes, while the electron transfer occurs in the opposite direction. Thus, oxygen permeation is owing to both ionic and electronic conductivities of the membranes. Once these lattice oxygen ions reach the permeate side of the membranes, they release their electrons and are recombined to oxygen molecules. Oxygen molecules then diffuse to the bulk gas in the permeate side.

1.2.2. Fuel conversion

When the oxygen transport membrane is employed within the reactor where hydrocarbon oxidation reactions occur, it can be used as an oxygen distributor. Migration of the oxygen ions in a controlled manner (i.e., by changing sweep flow rate, temperature, etc.) results in the opportunity for reaction selectivity in ITM reactors [38]. Since oxygen is selectively added to the permeate side through ion transport (not a convective flow as in conventional reactors), it leads to a low concentration of oxygen in the reactant mixture, as compared to conventional reactors using the air. The low oxygen concentration typically drives the oxidation reactions toward partial oxidations (syngas formation) or oxidative coupling to form intermediate products [39] depending on the local oxygen/fuel ratio, rather than complete oxidation. It is also found that oxy-fuel combustion (complete oxidation of fuel) can be achieved within these membrane reactors [40].

These reactions are, in part, driven by catalytic activity of the mixed-conducting membranes. The catalytic activity is dependent on the composition of the membranes, synthesis method, surface exchange rate, surface morphology, and electronic conduction mechanism [38]. Depending on the permeation rates, reaction locations, the temperature, the pressure, and the catalytic activity of the membranes, desired oxidation reactions can occur within these ITM reactors. Oxidation reactions within these reactors can be categorized as follows.

1.2.2.1. Oxidative coupling

If the mixed-conducting membranes show catalytic activity or are covered with certain catalysts (e.g., Li/MgO) [41], methane oxidation can be routed to the formation of C_2 products, such as ethylene or ethane. Oxygen ions are supplied in a controlled way and reacted directly within the lattice structure with adsorbed methane [42]. Increasing the methane conversion rate results in a lower C_2 selectivity. The overall reactions can be modeled as follows [43],

$$\begin{aligned} &CH_4 \leftrightarrow CH_4(s) \\ &2CH_4(s) + O_O^x + 2h^{\bullet} \leftrightarrow 2CH_3 + H_2O + V_O^{\bullet\bullet} \\ &2CH_3 \leftrightarrow C_2H_6 \end{aligned} \qquad \textbf{Eq. 1-3}$$

where (s) shows the surface species. Oxidative coupling using the ITM reactors is a good method to convert methane to higher hydrocarbons or liquid fuels. However, membrane degradation should be resolved, and the high C_2 selectivity as well as the significant methane conversion rate should be achieved at the same time.

1.2.2.2. Partial oxidation

Mixed-conducting membranes may also be used for partial oxidation of fuel to CO and H_2, which is called syngas formation, depending on the permeation rate, stoichiometry, and catalytic activity of the membrane. Rh-based catalysts mounted on the membranes can enhance catalytic partial oxidation. Aided by Rh-based catalysts, methane conversion higher than 90% with greater than 90% CO selectivity is detected [44, 45]. This process whose residence time is less than 0.1s [44, 46, 47], as shown below, is much faster than conventional reforming reactions (residence time is 0.5~1.5s) and reduces the reactor size in comparison with conventional reformers.

$$\begin{aligned}&CH_4 \leftrightarrow C(s) + 4H(s)\\&C(s) + O_O^x \leftrightarrow CO(s) \leftrightarrow CO\\&2H(s) \leftrightarrow H_2\end{aligned}$$

Eq. 1-4

Moreover, higher selectivity and exothermic reactions make this partial oxidation within the ITM reactors more promising. Non-premixed reactants with a low oxygen concentration due to the oxygen permeation environment enable higher selectivity compared to conventional (co-feed) reforming reactors. In addition, the overall process could be self-sustaining by heating up the membrane using the heat of reactions, which translates into the elevated temperature for the oxygen transport. This exothermic partial oxidation process can be combined with conventional endothermic reforming processes [48] to reduce heat inputs from external sources.

1.2.2.3. Oxy-fuel combustion

Complete oxidation of fuel to form CO_2 and H_2O as products is also possible within these ITM reactors, which is called oxy-fuel combustion. Employing oxy-fuel combustion, the ITM reactors can be used in fossil-fueled power plants while reducing CO_2 emissions. Although it is a promising technology, oxy-fuel combustion in membrane reactors has not yet been explored thoroughly.

$$CH_4 + 2O_2 \rightarrow CO_2 + 2H_2O$$

Eq. 1-5

Methane can react in the gaseous phase or on the catalytic surface of the membranes. A low oxygen concentration on the permeate side of the reactor results in diffusion-limited non-premixed combustion. If catalytic oxidation is involved, it may affect the gas-phase chemistry [49]. Because of the membrane reactor operating conditions, higher hydrocarbons and carbon monoxide can also be produced along with the main products, carbon dioxide and water. Thus, operating conditions, which include both air and fuel feed flow rates, temperature, and dilution ratio in the fuel stream, should be carefully controlled to ensure complete oxidation [40].

1.3. Previous modeling study

Given the novelty of the technology, only few modeling studies on ITM supported fuel conversion and oxygen permeation so far have been performed and based on reduced chemistry and simplified transport. Tan et al. [40] and Jin et al. [50] showed the dependence of oxygen permeation and fuel conversion rates on the initial gas temperature, air and fuel flow rates and reactor geometry. They assumed a plug flow to model their reactor and used single step chemical reactions for methane oxidation and reforming. The effects of the oxidation reactions on the gas temperature were also neglected. A more detailed model was proposed by Zhang et al. [51] and Smit et al. [52], but species concentrations at equilibrium with reduced chemistry were considered, and the spatial variations of species concentrations and temperature were ignored. Tan et al. [53] considered the spatially resolved oxygen concentrations and temperature in a membrane reactor for partial oxidation of methane, and solved for the product selectivity and hydrocarbon conversion as a function of the operating parameters including temperature, methane flow rate, membrane tube diameter and membrane thickness. They implemented a three-step reaction mechanism accounting for methane combustion, steam and carbon dioxide reforming, and based their oxygen permeation model on kinetic parameters obtained using the bulk stream parameters by Xu and Thomson [31]. Mancini and Mitsos [54, 55] developed an axial, quasi two-dimensional model, which incorporates semi-empirical oxygen transport equations and simplified fuel oxidation kinetic mechanisms, to examine the dependence of ITM reactor performance on the reactor geometry, flow configuration, operating conditions and membrane material properties. Akin and Lin [56] assumed different permeation mechanisms, p-type and n-type flux expressions, and two limiting oxidation kinetics: either extremely fast reaction or no conversion. Using a simple reactor model such as a continuously stirred tank reactor (CSTR), they examined how the oxidation reaction rates, the reducing gas flow rate and the feed-side oxygen partial pressure influence the oxygen permeation rate. Based on the same CSTR model, Rui et al. [57] investigated the effect of the finite chemical kinetic rates on the oxygen permeation rate. The results from these two studies have shown that the chemical reactions and their kinetic rates have substantial influence on oxygen permeation. However, their models considered a well-stirred reactor and assumed arbitrary reaction kinetic rates. Wang and Lin [58] estimated the kinetic parameters assuming that perovskite membranes behave catalytically in a way similar to Li/MgO membranes and applied them to the CSTR model. Although some modeling studies have also been performed on membrane reactors for syngas production [50, 53, 59, 60], these considered additional catalysts mounted on the membrane surface, and hence the results are not representative of the catalytic activities of the perovskite membrane itself and do not necessarily reflect the actual impact of heterogeneous reactions on the oxygen permeation.

Numerical modeling studies conducted so far have not related the homogeneous and heterogeneous chemical kinetics to the local thermodynamic state, and have not resolved their coupling with the oxygen permeation and flow field in detail. Oxygen permeation expressions used in these modeling studies were parameterized in terms of the bulk oxygen concentrations measured outside ITM reactors. In addition, they assumed heterogeneous fuel conversion on the catalyst surface additionally mounted on the membrane and ignored the homogeneous reactions that play an important role in fuel oxidation at high temperature. However, as I show in this thesis, permeation flux models parameterized in terms of the oxygen concentration in the bulk may not be applicable in the case of a reactive flow on the permeate side. I also show that detailed chemistry is necessary to account for the reaction pathway and important phenomena such as fuel pyrolysis. We note that an ITM requires high temperature for enabling substantial oxygen permeation to facilitate fuel conversion processes [61]. While a catalyst may contribute to fuel conversion typically at low temperature [62], in this high temperature regime, it has been demonstrated that the chemical reactions in the gas-phase dominate fuel conversion even if the surface catalytic reactions take place [63, 64]. Furthermore, spatially resolved solutions in the direction normal to the membrane should be obtained to examine the key features of ITM supported fuel conversion and oxygen permeation. Thus, spatially resolved solutions with detailed gas-phase chemistry and transport are necessary to model fuel conversion processes, to characterize the heterogeneous chemical kinetics for an ITM, and to capture important phenomena on the sweep side of the ITM where the oxygen permeation rate and hydrocarbon conversion/product selectivity are strongly coupled through flow conditions and their variations in the vicinity of the membrane [20].

1.4. Approach

To investigate the key features of oxygen permeation and fuel conversion in ITM reactors, I have used an one-dimensional stagnation flow configuration that matches the experimental apparatus that has been developed and facilitated in our Lab [65]. At first, the spatially resolved physical model was used to parameterize an oxygen permeation expression in terms of the local thermodynamic state near the membrane and to study the oxygen permeation process. Then, the numerical model incorporating the detailed methane chemistry and transport was used to get a better understanding of the fuel conversion processes and phenomena arising in ITM reactors. Finally, the heterogeneous chemistry for perovskite membranes was characterized, and the catalytic reaction kinetic parameters were obtained by performing numerical simulations.

1.4.1. Model development

For the detailed numerical investigation of ITM reactors, an existing one-dimensional numerical model used for the simulation of a strained flame has been employed [66, 67]. It has been modified for a membrane reactor in which a finite-gap stagnation flow is established. The model incorporates detailed homogenous chemistry and transport and resolves spatially the flow field near the membrane. The geometry and reactor material characteristics used in the model are based on the experimental setups. Because the membrane divides the physical domain into two domains (air side and fuel side), coupling of these two domains is a challenge in the numerical simulation.

Incorporating detailed homogeneous chemistry as well as the oxygen ion transport mechanism into the model, it is possible to resolve the influence of fuel conversion on the membrane temperature and to estimate oxygen concentration at the membrane surface, both of which govern the oxygen permeation rate, and neither had been considered with much fidelity in the literature.

1.4.2. Cold flow analysis (permeation study)

Although many investigations have been conducted to measure the permeation rates for different membrane geometry, composition, temperature, pressure, and gas mass flux, limited attention has been paid to spatially resolving flow information (i.e., oxygen partial pressure profiles), as well as to numerical studies for the oxygen ion transport. Typically, global measurements are assumed to asymptotically approximate the oxygen permeation rates ignoring the spatial variation of the oxygen partial pressures in the gas phase near the membrane surface. Oxygen ion transport should be investigated in the vicinity of the membranes. In this thesis, I used the numerical model to examine oxygen permeation by considering the spatially resolved oxygen partial pressure. Focusing on the oxygen partial pressure profiles and using constitutive equations to describe the surface exchange and bulk diffusion of the oxygen ions, I was able to construct a more reliable oxygen permeation model with more detailed kinetic expressions.

1.4.3. Reacting flow analysis (hydrocarbon oxidation reactions)

The reaction environment on the sweep side of an ITM needs to be characterized, and influences of hydrocarbon conversion on the oxygen permeation rate or vice versa should be investigated. High temperature, low oxygen concentration, diffusion-limited reactions lead to a reacting environment for the mixed-conducting membrane reactors, which has not yet been well characterized. It is important to understand the fuel conversion processes in order to identify and evaluate ITM reactor control and design strategies. By employing a detailed homogeneous chemical kinetic mechanism, the operating conditions necessary to produce the desired products from ITM reactors were identified.

1.4.4. Catalytic reaction kinetics

The catalytic kinetics of oxygen surface exchange and fuel oxidation for a perovskite membrane in terms of the thermodynamic state in the immediate vicinity of or on the membrane surface was investigated. I inferred the kinetic parameters for heterogeneous oxygen surface exchange and catalytic fuel conversion reactions, based on permeation rate measurements and a spatially resolved physical model that incorporates detailed chemical kinetics and transport in the gas-phase. The conservation equations for surface and bulk species are coupled with the gas-phase species governing equations through the species production rates from surface reactions.

1.5. Conclusions

A novel membrane technology, the ITM reactor, has been demonstrated for its use in power plants with CO_2 capture, and system's studies show that it is a promising option for reducing the energy penalty and capital expenditure for air separation. Although some studies have been conducted to examine ITM reactors, lack of knowledge on the important features of oxygen permeation and hydrocarbon conversion processes still exists. To make these systems more viable, it is important to investigate the oxygen transport, thermodynamic and chemical kinetic (including thermochemistry, electrochemistry, and catalysis) processes in the gas-phase and on the catalytic membrane surface, and their interactions.

To meet these research needs, this study has been focused on the detailed analysis of oxygen permeation and hydrocarbon conversion in ITM reactors by using numerical simulations. A spatially resolved physical model has been used to understand (a) oxygen ion transport, (b) homogeneous and heterogeneous fuel conversion, and (c) chemical kinetic phenomena (such as pyrolysis). A thorough literature review has been used in the development of accurate sub-models/mechanisms for each process. The spatially resolved numerical results enhance our understanding of the coupling between oxygen permeation and fuel conversion within ITM reactors, which will ultimately enable us to identify and evaluate ITM reactor control and design strategies.

1.6. Thesis outline

In Chapter 2, the spatially resolved physical model, numerical approach, oxygen permeation flux expression and detailed gas-phase chemistry and transport employed in this thesis are described.

In Chapter 3, the oxygen permeation flux expression has been parameterized in terms of the oxygen concentrations at the membrane surface given data on the bulk concentration, which is necessary for cases when mass transfer limitations on the permeate side are important and for reactive flow modeling. At the conditions relevant for ITM reactor operation, the local thermodynamic state should be taken into account when the oxygen permeation rate is examined. To elucidate this, the dependency of oxygen transport and fuel conversion on the geometry and flow parameters including the membrane temperature, air and sweep gas flow rates, oxygen concentration in the feed air and fuel concentration in the sweep gas has been discussed.

In Chapter 4, the reaction environment on the sweep side of an ITM has been characterized. The physical model was used to predict homogeneous fuel conversion processes and to capture the important features (e.g., the location, temperature, thickness and structure of a flame) of laminar oxy-fuel diffusion flames stabilized on the sweep side. The nature of oxygen permeation does not allow pre-mixing of fuel and oxidizer (i.e., sweep gas and permeated oxygen), establishing non-premixed flames. In oxy-fuel combustion applications, the sweep side is fuel-diluted with CO_2 and/or H_2O, and the entire unit is preheated to achieve a high oxygen permeation flux. This study focuses on the flame structure under these conditions and specifically on the chemical effect of CO_2 dilution.

In Chapter 5, the interactions between oxygen permeation and homogeneous fuel oxidation reactions on the sweep side of an ITM have been examined. Within ITM reactors, the oxidizer flow rate, i.e., the oxygen permeation flux, is not a pre-determined quantity, since it depends on the oxygen partial pressures on the air and sweep sides and the membrane temperature. Instead, it is influenced by the oxidation reactions that are also dependent on the oxygen permeation rate, the initial conditions of the sweep gas, i.e., the fuel concentration, flow rate and temperature, and the diluent. A parametric study with respect to key operating conditions has been conducted to investigate their interactions.

In Chapter 6, the catalytic kinetics of oxygen surface exchange and fuel oxidation for a perovskite membrane in terms of the thermodynamic state in the immediate vicinity of or on the membrane surface was investigated. Perovskite membranes have been shown to exhibit both oxygen perm-selectivity and catalytic activity for hydrocarbon conversion. However, a description of their catalytic surface reactions is still required. The kinetic parameters for heterogeneous oxygen surface exchange and catalytic fuel conversion reactions were inferred, based on permeation rate measurements and a spatially resolved physical model that incorporates detailed chemical kinetics and transport in the gas-phase. It is shown that the local thermodynamic state at the membrane surface should be accounted for when constructing and examining membrane permeation and heterogeneous chemistry. The significance of modeling both homogeneous and heterogeneous chemistry and their coupling when examining the results was discussed.

Chapter 2 Physical Model and Solution Methodology

2.1. Overview

To examine the oxygen permeation, fuel conversion processes and associated important phenomena (e.g., the relationship between the oxygen permeation rate and the oxidation reactions, hydrocarbon pyrolysis and the formation of possible soot precursors) occurring on the sweep side of the ITM, a stagnation flow configuration has been used. The corresponding experimental reactor, whose geometry is based on a planar, finite-gap stagnation flow shown in **Figure 2-1**, has been developed [65]. The gas flow in the neighborhood of the stagnation line is self-similar, and the dimensionality of the model is reduced to one dimension. The self-similar stagnation-flow configuration is selected because detailed chemistry and species transport in the gas-phase can be implemented while keeping the computational cost at a manageable level. As pointed out by Akin and Lin [56] and Rui et al. [57], detailed analysis of the chemical reactions, the mass and heat transfer and the local thermodynamic state is necessary for the studies of ITM supported fuel conversion processes and their relationship with oxygen permeation. Note that flames described by self-similar solutions have been very useful in studies of fuel conversion processes and flame properties [68, 69]. It should be noted that such solutions are only valid in the region near the axis of symmetry in the reactor, as has been demonstrated for this reactor configuration [70]. Although the results from this study may need some geometrical translation to be applicable to other reactor systems due to the geometry, the flow field (and thus the mass transfer) and reactor dynamics, this configuration allows sufficiently detailed analysis of the fluid dynamic and thermo-chemical processes, contributing to the understanding of ITM reactors and the underlying physics in multi-dimensional, commercial reactor configurations. Furthermore, the knowledge and oxygen permeation expressions gained from such investigations can be applied for future studies considering more complex reactor configurations and geometries.

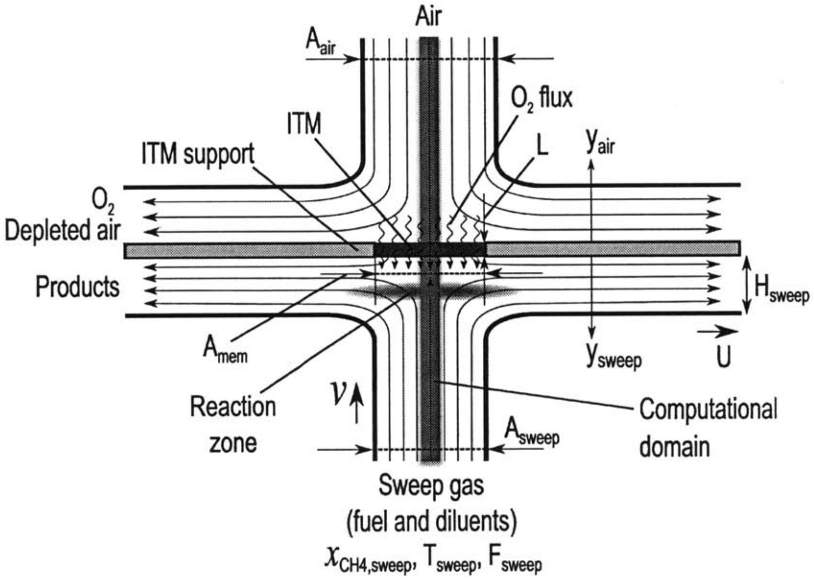

Figure 2-1 The stagnation-flow configuration considered in this investigation (v = normal velocity (y-direction), U = scaled transverse velocity (x-direction), $x_{CH_4,sweep}$ = fuel concentration in the sweep gas on a molar basis, T_{sweep} = sweep gas inlet temperature, F_{sweep} = sweep gas flow rate, H_{sweep} = sweep gas channel height, L = membrane thickness, air inlet area = $A_{air} = 5.33 \times 10^{-3} m^2$, sweep gas inlet area = $A_{sweep} = 5.81 \times 10^{-3} m^2$ = membrane area = A_{mem})

2.2. Governing equations

The flow fields in each domain, i.e., the air and sweep gas domains, are determined by the system of governing equations derived from the general three-dimensional equations of reacting flow [71], whose dimensionality is reduced one dimension. As shown in **Figure 2-1,** x is a transverse coordinate along the membrane direction, and y is an axis normal to the membrane. It is assumed that variations in the z-direction, normal to the $x-y$ plane of the flow, are negligible. The species and thermal diffusion along the x-direction are neglected with respect to those in the y-direction. A self-similar solution is obtained, in which all the normalized flow variables are functions of the direction normal to the membrane and time. In addition, a low Mach number assumption is employed because gas flow velocities are low. The thermal species diffusion (i.e., Soret effect) is taken into account because of a high temperature gradient near the membrane. The effect of viscous dissipation is assumed to be much smaller than the heat released by chemical reactions and hence is neglected. Moreover, Dufour heat flux, which is typically three orders of magnitude smaller than the Fourier heat flux, is neglected. Gas-phase radiation is also neglected. The stagnation flow formulation has been known to be valid over almost the entire range of Reynolds number with good accuracy [72]. Furthermore, using a CH_4/air flame with the inlet velocity of 5.4 cm/s, which is smaller than the velocity considered in the current study, Kee et al. demonstrated that the reaction zone shows no radial dependence, confirming that the self-similar solution is valid in this low Reynolds number regime [71]. The pressure variations are negligible in comparison with the thermodynamic pressure, and the oxygen partial pressure that determines the oxygen permeation flux [12] depends only on its mole fraction and the total pressure. The solution variables and the system of governing equations are as follows:

$V(t,y)=\rho \upsilon$: Mass flux in the y-direction; normal to the membrane [kg/m^2/s]

$U(t,y)=\frac{u}{x}$: Scaled transverse velocity in the x-direction; parallel to the membrane [1/s]

$Y_k(t,y)$: Species mass fraction

$T(t,y)$: Temperature [K]

$\Lambda_x(t)=\frac{1}{x}\frac{dp}{dx}$: Scaled transverse pressure gradient [kg/m^3/s^2]

$$\frac{\partial \rho}{\partial t}+\frac{\partial V}{\partial y}+\rho U=-\frac{\rho}{T}\frac{\partial T}{\partial t}-\sum_{k=1}^{N}\frac{\rho\bar{W}}{W_k}\frac{\partial Y_k}{\partial t}+\frac{\partial V}{\partial y}+\rho U=0$$

: Continuity **Eq. 2-1**

$$\rho\frac{\partial U}{\partial t}+V\frac{\partial U}{\partial y}+\rho U^2+\Lambda_x-\frac{\partial}{\partial y}\left(\mu\frac{\partial U}{\partial y}\right)=0$$

: x-momentum **Eq. 2-2**

$$\rho\frac{\partial Y_k}{\partial t}+V\frac{\partial Y_k}{\partial y}+\frac{\partial j_k}{\partial y}-\dot{\omega}_k\,W_k=0$$

: Species **Eq. 2-3**

where, $j_k=-\rho D_{km}\left(\frac{\partial Y_k}{\partial y}+\frac{Y_k}{\bar{W}}\frac{\partial \bar{W}}{\partial y}\right)-\frac{D_k^T}{T}\frac{\partial T}{\partial y}$

$$\rho\frac{\partial T}{\partial t}+V\frac{\partial T}{\partial y}+\frac{1}{c_p}\left[\sum_{k=1}^{N}\hat{h}_k\,\dot{\omega}_k+\sum_{k=1}^{N}j_k c_{p,k}\frac{\partial T}{\partial y}-\frac{\partial}{\partial y}\left(\lambda\frac{\partial T}{\partial y}\right)\right]=0$$

: Energy **Eq. 2-4**

$$\frac{\partial \Lambda_x}{\partial y}=0$$

: Pressure curvatures **Eq. 2-5**

where ρ is the density; υ is the normal velocity; u is the transverse velocity; μ is the dynamic viscosity; D_{km} is the mixture-averaged diffusion coefficient; D_k^T is the thermal diffusion (Soret effect) coefficient; $\bar{W}$ is the mixture molecular weight; W_k is the molecular weight of species k; $\dot{\omega}_k$ is the molar production rate of species k; c_p is the mixture specific heat; $c_{p,k}$ is the specific heat of species k; $\hat{h}_k$ is the molar enthalpy of species k; λ is the mixture thermal conductivity; N is the number of gas-phase species. To model the finite domain configuration where the inlet velocity is imposed as a boundary condition, the pressure curvature equation is added to the system of governing equations. This is in contrast to the semi-infinite stagnation flow configuration conventionally considered in opposed-flow flame studies. Therefore, the pressure gradient is determined as a part of the solution in order to satisfy the remaining boundary conditions [71]. Along with the system of governing equations, the equation of state is used to compute the density as a function of species mass fractions:

$$\rho = \frac{p\bar{W}}{RT} \qquad \textbf{Eq. 2-6}$$

where R is the universal gas constant.

2.3. Boundary conditions

The boundary conditions describe inflow conditions at the inlets and flux-matching conditions at the membrane surface. Flux-matching conditions are applied to the continuity, species and energy conservation equations at the membrane surface, $y = 0$. The convective and diffusive mass fluxes of the gas-phase species at the membrane surface are based on the oxygen permeation. In an ITM unit, only oxygen is separated from the air. It permeates to the sweep side of the membrane. Thus, boundary conditions for the continuity and species conservation equations include the oxygen permeation rate, J_{O_2}, which is negative on the air side (sink term) and positive on the sweep gas side (source term) as follows:

$$V_{mem} = \begin{cases} -J_{O_2} & (air) \\ +J_{O_2} & (sweep) \end{cases}$$ **Eq. 2-7**

$$j_k + Y_k V_{mem} = \begin{cases} \pm J_{O_2} & (k = O_2) \\ 0 & (k \neq O_2) \end{cases}$$ **Eq. 2-8**

where V_{mem} is the mass flux at the membrane surface. In addition, heat released from chemical reactions on the sweep gas side is transferred to the membrane, which transfers heat to the air domain and to the surrounding walls via radiation. Radiation heat transfer is considered between the membrane and the reactor walls (Inconel 601 [65]). In the ITM unit configuration [65], the membrane sees a large area of the wall, and the shape factor is taken to be unity. Therefore, the energy conservation across the membrane relates the heat fluxes, $Q^{"}_{sweep}$ and $Q^{"}_{air}$, to and from the membrane, respectively, and its temperature, as shown below.

$$Q^{"}_{sweep} - Q^{"}_{air} - 2\sigma\varepsilon_{mem}\left(T^4_{mem} - T^4_{\infty}\right) = 0$$ **Eq. 2-9**

where, $Q^{"}_{air} = -\lambda\nabla T + \sum_{k=1}^{N}\left(j_k + Y_k V_{mem}\right)\hat{h}_k$

$$Q^{"}_{sweep} = \lambda\nabla T - \sum_{k=1}^{N}\left(j_k + Y_k V_{mem}\right)\hat{h}_k$$

where σ is the Stefan-Boltzmann constant, T_{∞} is the surrounding wall temperature, and ε_{mem}

is the emissivity of the membrane. The emissivity of the membrane, $\varepsilon_{mem} = 0.8$, has been measured [73]. It is assumed that T_∞ is the same as the gas inlet temperature at steady state. On the other hand, the no-slip condition at the solid surface makes the transverse velocity at the membrane surface (U_{mem}) set to zero.

$$U_{mem} = 0 \qquad \textbf{Eq. 2-10}$$

Input operating conditions are imposed at the inlets, $y = H$. The mass influx, V_{air} and V_{sweep}, and the gas inlet temperature, T_{air} and T_{sweep}, are known. The mass ratio of oxygen to nitrogen in the air dictates the gas composition, $Y_{k,air}$, at the air inlet, whereas the fuel dilution ratio between methane and the diluent such as carbon dioxide determines the composition of the gas inflow, $Y_{k,sweep}$, in the sweep gas side. The normal flow condition implies a zero transverse velocity, i.e., $u_{in} = U_{in} = 0$.

$$V_{in} = \begin{cases} V_{air} & (air) \\ V_{sweep} & (sweep) \end{cases} \qquad \textbf{Eq. 2-11}$$

$$Y_{k,in} = \begin{cases} Y_{k,air} & (air) \\ Y_{k,sweep} & (sweep) \end{cases} \qquad \textbf{Eq. 2-12}$$

$$T_{in} = \begin{cases} T_{air} & (air) \\ T_{sweep} & (sweep) \end{cases} \qquad \textbf{Eq. 2-13}$$

$$U_{in} = 0 \qquad \textbf{Eq. 2-14}$$

Note that the mass influx boundary condition is satisfied through the pressure curvature equation. Because the continuity equation is first-order, it needs only one boundary condition at the membrane surface, which is the oxygen permeation rate. However, the finite-gap stagnation flow configuration requires another mass flux boundary condition at the inlets to take into account the given mass influx. The pressure curvature equation does not have an explicit boundary condition and is solved to satisfy the specified mass flux at the inlets.

2.4. Detailed chemistry and transport and numerical methodology

To examine the fuel conversion processes, the detailed chemical kinetic mechanism for methane, GRI-Mech 3.0 [74], is implemented for the homogeneous gas phase chemical reactions. Since it has not been elucidated what reactions are important in governing the overall fuel conversion processes, detailed chemistry is necessary for capturing important phenomena and chemical species appearing in the vicinity of the membrane. To integrate the multi-step chemical reactions and evaluate the thermodynamic and the transport properties shown in the governing equations and reaction kinetics, Cantera [75] is used along with NASA polynomials. Surface reactions are ignored to focus on the gas-phase fuel conversion and their relationship with oxygen permeation. Surface chemistry will be considered in future studies.

A finite difference method, which has been used for stiff numerical problems such as combustion, is used to discretize the governing equations and boundary conditions. The convective terms are discretized using a first-order upwind differencing to avoid numerical instabilities [71]. The diffusion terms in the momentum equation and the species conservation equations are approximated to second-order accuracy. A first-order fully implicit finite difference is implemented to discretize the continuity equation. The discretized equations are integrated using the Sundials IDA solver [76], which integrates the differential algebraic equations using a variable-order (from 1 to 5) backward differentiation formula. At each time step, this produces a system of nonlinear algebraic equations, which are solved using a preconditioned Newton-Krylov method.

Due to the presence of the membrane, the computational domain is divided into two parts, the air domain and the sweep gas domain. The air and sweep gas domains are coupled to obtain the steady state solution by matching the two flux-matching boundary conditions, the oxygen permeation rate and the heat flux, as shown in **Figure 2-2**.

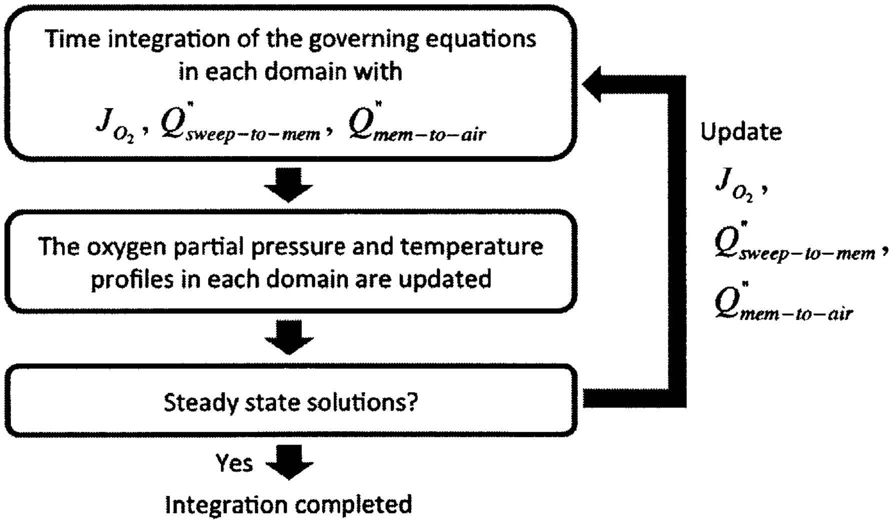

Figure 2-2 The methodology to couple the two computational domains, air and sweep gas domains, by using the two flux-matching conditions, the oxygen permeation flux and the heat flux

Each domain considers the oxygen permeation rate and the heat flux as boundary conditions at the membrane surface during time integration, which are solved for during and intermediate calculation step. After the system of governing equations for each domain is integrated using the inlet boundary conditions and the two flux-matching boundary conditions determined during the previous time step, the oxygen partial pressure profile and the temperature profile in each domain are updated. Note that the oxygen permeation rate and the heat flux depend on the partial pressures of oxygen in the immediate vicinity of the membrane and the temperature profile in both domains, respectively. Therefore, the new oxygen partial pressures and the new temperature profile must be used to update the oxygen permeation rate and heat flux for the following time step. This simulation procedure is repeated until a steady state solution is acquired.

2.5. Conclusions

A numerical model for oxygen transport and fuel conversion processes in an ITM reactor was presented. The physical model is consistent with a finite-gap stagnation flow configuration, and incorporates detailed gas-phase chemistry and transport enabling us to obtain the spatially resolved profiles of species concentration, temperature and reaction rates. The membrane separates the domain into two sides, the feed side and the permeate side, coupled by the oxygen permeation flux and the heat flux across the membrane. An efficient numerical approach has been implemented to obtain solutions over a wide range of operating conditions.

Chapter 3 Oxygen Permeation and Transport

3.1. Overview

Oxygen permeation rate and hydrocarbon conversion/product selectivity are strongly coupled through the local oxygen chemical potential in the vicinity of membrane surfaces, as well as the membrane temperature [20]. In case a homogeneous reaction takes place on the permeate side, the local oxygen concentration in the vicinity of the membrane is influenced by oxidation reactions and hence cannot be approximated by the bulk stream oxygen concentrations measured at the permeate stream outlet side. With respect to fuel conversion, since oxygen is introduced at a finite rate, its local concentration plays an important role in determining the overall reaction rate and reaction products. Therefore, it is important to perform experimental studies and to develop modeling approaches that can spatially resolve the thermochemical field in the immediate neighborhood of the membrane. So far only a limited number of studies have been conducted [40, 50, 52, 53].

I parameterized an oxygen permeation flux model in terms of the local oxygen partial pressures in the vicinity of the membrane and used it to examine the dependence of oxygen permeation on key operating conditions. I show that it is important to use permeation flux models based on the values of the oxygen concentration close to the membrane surface, and show how experimental measurements of the flux and the oxygen concentration at the bulk can be used to calculate the oxygen concentration at the surface. The spatially resolved flow field is used to estimate the kinetic parameters of the membrane. Next I use the permeation flux model to study the dependence of oxygen transport on the operating conditions including the presence of a fuel in the sweep gas.

3.2. Oxygen transport mechanism

The oxygen permeation mechanism is incorporated into the coupled thermochemical-fluid dynamic model described in Chapter 2 as a boundary condition at the membrane surface, using a single step expression. In this expression, the oxygen permeation flux is described in terms of the gas phase parameters, that is, the oxygen partial pressure in the immediate neighborhood of the membrane on both air and sweep gas sides. This expression is derived in this section starting with a multi-step mechanism. **Figure 3-1** shows the important steps of oxygen transport across the membrane: the gas phase mass transfer, surface exchange and bulk diffusion, following the chemical potential gradient. The gas phase mass transfer is described using a fluid dynamic model, while surface exchange and bulk diffusion are based on surface species and bulk phase ions inside the membrane [12, 77]. Instead of keeping track of the surface species and bulk phase ions, a single step expression that accounts for surface exchange on both sides of the membrane and bulk ion diffusion across the ITM is developed. Implementing a single-step oxygen transport expression across the membrane improves the computational efficiency of the overall model and enables studying important oxygen transport steps and their dependence on other gas-phase flow parameters.

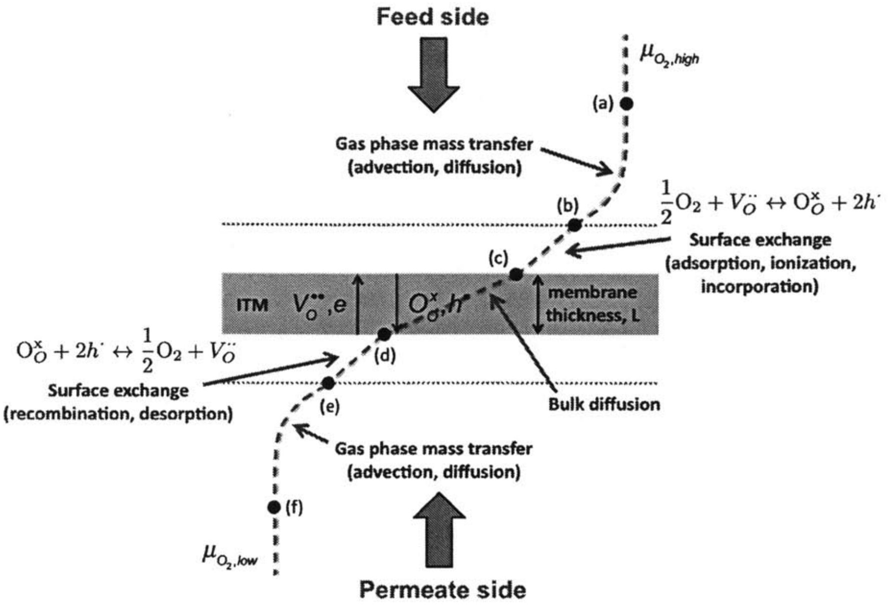

Figure 3-1 Oxygen transport processes within the ITM unit following the oxygen chemical potential gradient (revised from [37])

3.2.1. Overview of oxygen transport processes

Based on the difference in the oxygen chemical potentials between the feed side and the permeate side, the membrane temperature and its ambipolar conductivity, oxygen migrates from the high pressure feed side to the low pressure permeate side, according to the overall transport processes summarized as follows [21-24] (refer to **Figure 3-1** for stream points, (a) through (f)):

i. **(a) to (b):** gaseous oxygen mass transfer (advection and diffusion) from the feed stream to the membrane surface

ii. **(b) to (c):** adsorption onto the membrane surface, dissociation and ionization of oxygen molecules and subsequent incorporation of the ions into the lattice vacancies (feed side surface exchange)

iii. **(c) to (d):** transport of lattice oxygen ions through the membrane (bulk diffusion)

iv. **(d) to (e):** association of lattice oxygen ions to oxygen molecules and desorption from the membrane surface into the gas phase (permeate side surface exchange)

v. **(e) to (f):** gaseous oxygen mass transfer (advection and diffusion) from the membrane surface to the permeate stream

The gaseous mass transfer processes (i and v) are modeled using homogeneous gas species conservation equations (continuity, momentum and energy). Global reaction kinetics is used to approximate the surface exchange (ii and iv), while the bulk diffusion (iii) is governed by internal defect reactions or oxygen vacancy transport.

3.2.1.1. Gas phase mass transfer

The gas phase mass transfer plays an important role in oxygen transport especially when the flow rate is low enough to result in a relatively thick boundary layer. A high flow rate of the sweep gas or feed gas reduces the corresponding boundary layer next to the membrane surface. In this case, the oxygen concentration profile in the gas is nearly uniform and its effect on the gas phase mass transfer is insignificant. This is the typical assumption in some ITM research. However, the flow rate in typical ITM reactors is small such that the required stoichiometry of the chemical reactions (i.e., fuel to oxygen ratio) is satisfied, and accordingly the boundary layer thicknesses can be large depending on the length scale of the reactor. In this case, the gas phase mass transfer has a significant impact on the oxygen concentration profile, especially in the permeate side where oxidation reactions occur. Recent research has highlighted the importance of the gas phase mass transfer and the non-uniform oxygen chemical potentials next to the membrane surface [78].

In typical ITM permeation measurements, the oxygen permeation rates are characterized in terms of the feed stream inlet partial pressure or oxygen concentration and the same parameters at the sweep gas outlet. Oxygen concentrations measured at these two points may not be the same as those at the two sides of the membrane surface. By ignoring the effects of the gas phase mass transfer, it is assumed that the measurements at the points away from the vicinity of the membrane surface are the same as the local values near the membrane ((b) and (e) in **Figure 3-1**). Thus, while the resulting expressions may be sufficient for describing similar set ups, they are not general [78] and the local oxygen concentration profiles should be determined in order to recast these expressions in terms of the local values at the vicinity of the membrane surface.

3.2.1.2. Surface exchange

The surface exchange processes connect the gas phase oxygen molecules in the immediate neighborhood of the membrane with the membrane surface species. As mentioned above, gaseous oxygen molecules adsorb onto the membrane surface, dissociated and ionized by reacting with available free electrons from the lattice, hence occupying an oxygen vacancy and forming two electron holes [37]. The reverse processes take place on the permeate side of the membrane after the oxygen ions transport across the membrane by bulk diffusion as discussed in Section 3.2.1.3. The global surface exchange reaction describing these processes is,

$$\frac{1}{2}O_2 + V_O^{\bullet\bullet} \xleftrightarrow{k_f/k_r} O_O^x + 2h^{\bullet} \qquad \textbf{Eq. 3-1}$$

The conventional Kroger-Vink notation is used here for the lattice species and defects where

$V_O^{\bullet\bullet}$ is the oxygen vacancy; O_O^x is the lattice oxygen ion; $h^{\bullet}$ is the electron hole, and k_f and k_r are the reaction rates of forward and backward reactions of Eq. 3-1, respectively. The Eq. 3-1 is sufficient to model the overall surface exchange process on both sides of the membrane [29, 33].

The law of mass action, with reaction rates based on the activation energy and membrane temperature, is used to approximate the oxygen surface exchange kinetics [25-29]. Based on the transition state theory, the reaction rates are typically expressed in an Arrhenius form,

$$k_i = \xi \frac{\kappa_B T_{mem}}{h_p} \exp\left(\frac{-E_A}{RT_{mem}} \right) \qquad \textbf{Eq. 3-2}$$

where k_i represents either forward (k_f) or backward (k_r) reaction rate of the surface exchange reactions, as described in Eq. 3-1; ξ is a transmission coefficient; κ_B is the Boltzmann constant; h_p is the Planck constant; E_A is the activation energy; T_{mem} is the membrane temperature and R is the universal gas constant. Surface exchange processes are strongly dependent on the membrane temperature and the activation energy that is a function of surface properties.

Typical mixed-conducting membranes have a substantially high electronic conductivity, and hence the electron hole concentrations are constant throughout the ITM at steady state. It can be assumed that the surface exchange reactions are no longer dependent on the concentration of electron holes. As a result, the backward reaction of surface exchange, expressed in Eq. 3-1, becomes pseudo-zero order at steady state under isothermal operations [61]. Then, based on the global reaction Eq. 3-1 and the reaction rate expression Eq. 3-2, the oxygen permeation rate by the surface exchange reaction on each side of the membrane can be expressed as,

$$J_{O_2} = k_f P_{O_2,feed,(s)}^{0.5} C_{V_O^{\bullet\bullet},feed} - k_r \qquad \text{: Feed side} \qquad \textbf{Eq. 3-3}$$

$$J_{O_2} = k_r - k_f P_{O_2,sweep,(s)}^{0.5} C_{V_O^{\bullet\bullet},sweep} \qquad \text{: Permeate side} \qquad \textbf{Eq. 3-4}$$

where $P_{O_2,feed,(s)}$ and $P_{O_2,sweep,(s)}$ stand for the oxygen partial pressures evaluated at the membrane surfaces in both the feed and sweep gas sides, respectively; $C_{V_O^{\bullet\bullet},feed}$ and $C_{V_O^{\bullet\bullet},sweep}$ are the molar concentrations of oxygen vacancies on the membrane surfaces in both feed and sweep gas sides, respectively. Note that Eq. 3-3 and Eq. 3-4 are equal at steady state. Depending on how the expressions in Eq. 3-3 and Eq. 3-4 are simplified or the reaction rate Eq. 3-2 is approximated, different empirical correlations for the surface exchange processes have been proposed [27-29, 36].

3.2.1.3. Bulk diffusion

When both ionic and electronic conductivities of the membrane are sufficiently high, oxygen ion transport through the membrane does not need an external electrical circuit. The permeation of oxygen ions is charge compensated by a flux of electrons in the reverse direction. Because these membranes are dense/gas-tight, direct permeation of gaseous oxygen molecules is prohibited, and only ionized oxygen can move across them. A number of different mechanisms have been discussed to explain bulk ion diffusion across an ITM, among which the vacancy transport mechanism is widely used [61]. Only mobile ionic defects can move from one lattice position to another, and the oxygen vacancy and electron hole are the two charged defects in ITM. When an oxygen vacancy moves to the site occupied by an oxygen ion, the oxygen ion is relocated to the site released by the oxygen vacancy. The transport of charged defects at steady state under an electrochemical potential gradient is described by the Nernst-Planck equation,

$$J_i = -\frac{\sigma_i}{(z_i F)^2} \nabla \eta_i \qquad \textbf{Eq. 3-5}$$

where σ_i is the ionic conductivity of charged defects *i*; z_i is the charge number of charged defects *i*; F is the Faraday constant; $\nabla \eta_i$ is the electrochemical potential gradient of charged defects *i*, which can be expressed as,

$$\nabla \eta_i = \nabla \mu_i + z_i F \nabla \phi \qquad \textbf{Eq. 3-6}$$

where $\nabla \mu_i$ is the chemical potential gradient of charged defects *i*, and $\nabla \phi$ is the electric potential gradient across the membrane. In general, transverse variations of charged defect concentrations are negligible in a thin mixed ionic-electronic conductor, and a one-dimensional approximation ((c) to (d) in **Figure 3-1**) can be implemented. Expression Eq. 3-5 and Eq. 3-6 are thus written as,

$$J_i = -\frac{\sigma_i}{(z_i F)^2} \left[RT \frac{\partial \ln C_i}{\partial y} + z_i F \frac{\partial \phi}{\partial y} \right] \qquad \textbf{Eq. 3-7}$$

where C_i is the molar concentration of charged defects *i*. The Nernst-Einstein relation explains σ_i, as shown below.

$$\sigma_i = \frac{(z_i F)^2 D_i C_i}{RT} \qquad \textbf{Eq. 3-8}$$

where D_i is the diffusivity of charged defects *i*. Depending on the simplification applied to the Nernst-Einstein relation for the ionic conductivity, different empirical correlations for bulk diffusion have been proposed [32-36]. Due to the high electronic conductivity of mixed-conducting ceramic membranes, the concentration of electrons is maintained constant across the ITM at steady state. As a result, the oxygen permeation is limited by the transport of oxygen vacancy (i.e., ionic conductivity). In addition, the membrane is electrically neutralized, and the electric potential gradient is generally neglected at steady state. Then, assuming a linear variation of oxygen vacancy concentration across the ITM, the oxygen vacancy transport can be expressed using expression Eq. 3-7 and Eq. 3-8 as,

$$J_{V_O^{\bullet\bullet}} = -D_{V_O^{\bullet\bullet}} \frac{\partial C_{V_O^{\bullet\bullet}}}{\partial y} = -\frac{D_{V_O^{\bullet\bullet}}}{L}\left(C_{V_O^{\bullet\bullet},sweep} - C_{V_O^{\bullet\bullet},feed}\right) \qquad \textbf{Eq. 3-9}$$

where L is the membrane thickness. Note that the oxygen vacancy diffusion coefficient, $D_{V_O^{\bullet\bullet}}$, is dependent on the temperature and the crystalline structure of the membrane. At steady state, under isothermal operations and for small differences in the oxygen partial pressures, the diffusion coefficient is assumed to be constant across the membrane. Based on the stoichiometry (refer to expression Eq. 3-1), the oxygen permeation rate by bulk diffusion becomes,

$$J_{O_2} = -\frac{1}{2} J_{V_O^{\bullet\bullet}} = \frac{D_{V_O^{\bullet\bullet}}}{2L} \left(C_{V_O^{\bullet\bullet},sweep} - C_{V_O^{\bullet\bullet},feed} \right) \qquad \textbf{Eq. 3-10}$$

Expression Eq. 3-10 shows that the oxygen permeation rate by bulk diffusion is governed by the ionic conductivity, temperature and the chemical potential gradient of oxygen vacancies across the membrane.

3.2.2. Reduction in terms of the partial pressures

As proposed by Xu and Thomson [31], at steady state, an expression that combines surface exchange on the feed and permeate sides and bulk diffusion in terms of the oxygen partial pressures can be derived. At steady state, expression Eq. 3-3, Eq. 3-4 and Eq. 3-10 are equal. Combining these expressions, the desired form is obtained [31]:

$$J_{O_2} = \frac{D_{V_O^{\bullet\bullet}} k_r \left(P^{0.5}_{O_2,feed,(s)} - P^{0.5}_{O_2,sweep,(s)} \right)}{2Lk_f \left(P_{O_2,feed,(s)} P_{O_2,sweep,(s)} \right)^{0.5} + D_{V_O^{\bullet\bullet}} \left(P^{0.5}_{O_2,feed,(s)} + P^{0.5}_{O_2,sweep,(s)} \right)} \qquad \textbf{Eq. 3-11}$$

Note that expression Eq. 3-11 describes the important dependence of the oxygen permeation rate on the surface exchange (i.e., the membrane temperature and the activation energy) and the bulk diffusion (i.e., the ionic conductivity, chemical potential gradient and membrane temperature) as discussed in Section 3.2.1.2 and Section 3.2.1.3 and can be used under surface exchange limited and bulk diffusion limited conditions.

To use the single step expression in the fluid dynamic model, the diffusion coefficient of oxygen vacancies, $D_{V_O^{\bullet\bullet}}$, and the surface exchange reaction rates, k_f and k_r, must be known. These can be expressed in an Arrhenius form as shown below,

$$\Theta_i = \psi_i \exp\left(\frac{-E_{A,i}}{RT_{mem}}\right) \qquad \text{where } \Theta_i = D_{V_O^{\bullet\bullet}}, k_f, k_r \qquad \textbf{Eq. 3-12}$$

The pre-exponential factor, ψ_i, and the activation energy, $E_{A,i}$, are derived from experimental data (i.e., oxygen permeation rates). Furthermore, the oxygen partial pressures used in expression Eq. 3-11 should be evaluated in the immediate vicinity of the membrane surface (i.e., $P_{O_2,feed,(s)}$ and $P_{O_2,sweep,(s)}$ ((b) and (e) in **Figure 3-1**), and not the bulk values. This is particularly important in cases when the local variations of oxygen partial pressure in the direction normal to the membrane surface are strong, as discussed in Section 3.2.1. Xu and Thomson [31] assumed that bulk stream parameters (i.e., $P_{O_2,feed,(b)}$ and $P_{O_2,sweep,(b)}$) can approximate the local oxygen partial pressures when they used a similar expression in their numerical and experimental work. Given that measurements of these variations are not often available, I propose to evaluate them using a numerical model, as explained in Chapter 2. The methodology to compute the oxygen partial pressure profiles is discussed in Section 3.3. The numerical model makes it possible to evaluate the partial pressures at the membrane surface, starting with these values in the bulk and the oxygen permeation flux. Using this approach, I recast the oxygen permeation flux in terms of the oxygen partial pressures at the membrane surface, endowing it with wider applicability.

3.3. Parameterization of spatially resolved oxygen transport expression

Numerical modeling of reacting flow supported membrane processes requires an oxygen transport flux expression that can be coupled with the gas-phase transport and reaction chemistry in the vicinity of the membrane. This is especially true in the case of oxy-fuel combustion and hydrocarbon reforming. Because of the presence of oxidation reactions near the membrane surface, flow parameters vary significantly throughout the boundary layer on the permeate side. In this case, the bulk stream parameters or mean values (i.e., $P_{O_2,sweep,(b)}$) are substantially different from the local values next to the membrane (i.e., $P_{O_2,sweep,(s)}$) because of the combined transport and chemical reactions. Therefore, the oxygen flux model must be formulated in terms of the local oxygen concentration at the membrane surfaces. These are not available in the literature, and it is difficult to measure these local properties experimentally. Instead, to proceed with my modeling effort, I first use the numerical model of the coupled flow-membrane process described above to derive the parameters in expression Eq. 3-11 and Eq. 3-12 from the measured global values. I use the permeation rates measured by Xu and Thomson. The flux expression in terms of the local oxygen partial pressures is then used to estimate the diffusion coefficient of oxygen vacancies and the reaction rates of surface exchange.

3.3.1. Estimation of local oxygen partial pressure

The numerical simulation is used to evaluate the local oxygen partial pressures using the experimentally measured oxygen permeation rates and bulk conditions. To produce the oxygen partial pressure profile, I used the experimentally measured oxygen permeation rates by Xu and

Thomson [31]. Using the $La_{0.6}Sr_{0.4}Co_{0.2}Fe_{0.8}O_{3-\delta}$ membrane, they generated 126 data points in a typical disc-type stagnation-flow permeation facility that were used to evaluate the six parameters (pre-exponential factors and activation energies) required in expression Eq. 3-12. Note that they used the bulk stream oxygen partial pressures, $P_{O_2,feed,(b)}$ and $P_{O_2,sweep,(b)}$, measured at the feed air inlet and a sweep gas outlet, respectively. Thus, the diffusion coefficient of oxygen vacancies and the reaction rates of surface exchange they derived are evaluated in terms of the bulk stream parameters or mean values. To utilize their permeation rate measurements for a reactive flow supported membrane process, where the parameters in expression Eq. 3-12 should account for the local flow variations, I used my model to numerically reproduce their experiments to determine the local oxygen partial pressures near the membrane surface. As discussed in Section 2.3, the continuity and the species conservation equations need an oxygen permeation rate to be used as a flux matching boundary condition at the membrane surface. The experimentally measured permeation rates are set as constant boundary conditions (for the continuity and species equations) at the membrane surface such as,

$$V_{mem} = \begin{cases} -J_{O_2,\exp} & (feed) \\ +J_{O_2,\exp} & (sweep) \end{cases} \qquad \textbf{Eq. 3-13}$$

$$j_k + Y_k V_{mem} = \begin{cases} \pm J_{O_2,\exp} & (k = O_2) \\ 0 & (k \neq O_2) \end{cases} \qquad \textbf{Eq. 3-14}$$

where the subscript $\exp$ represents the experimentally measured values.

The corresponding experimental conditions including feed and sweep gas flow rates, molar compositions and membrane temperature are used as boundary conditions at the inlets.

Table 3-1 shows the bulk stream oxygen partial pressures and the membrane temperature at which Xu and Thomson measured oxygen permeation rates. At the feed air inlet, $P_{O_2,feed,(b),\exp}$ is applied as a species boundary condition when the rest of the feed gas is nitrogen.

$$Y_{k,feed} = \begin{cases} \dfrac{P_{O_2,feed,(b),\exp}}{P^\circ}\dfrac{W_{O_2}}{\bar{W}} & (k = O_2) \\ \dfrac{\left(1 - P_{O_2,feed,(b),\exp}\right)}{P^\circ}\dfrac{W_{N_2}}{\bar{W}} & (k = N_2) \\ 0 & (k \neq O_2, N_2) \end{cases} \qquad \textbf{Eq. 3-15}$$

where P° is the operating pressure that is 1 atm. Note that the feed air flow rate is maintained at the maximum value of 150 ml/min (STP) to reduce the gas phase mass transfer effect in the feed domain [31], and thus the mass flux of feed air is,

$$V_{feed} = \frac{150\rho_{feed}}{A_{feed}} \qquad \textbf{Eq. 3-16}$$

where ρ_{feed} is the density of feed air (STP), and A_{feed} is the feed inlet area of $5.333\times10^{-3}m^2$. At the sweep gas inlet, the mass flux of the sweep gas can be found from the measured permeation rates and $P_{O_2,sweep,(b),\exp}$ measured by Xu and Thomson. Since $P_{O_2,sweep,(b),\exp}$ is measured at the sweep gas outlet assuming perfect mixing between the permeated oxygen and the sweep gas, $P_{O_2,sweep,(b),\exp}$ is estimated as,

$$P_{O_2,sweep,(b),\exp} = \frac{J_{O_2,\exp}}{V_{sweep} + J_{O_2,\exp}} \times P^{\circ}$$ **Eq. 3-17**

Then, the sweep gas mass flux to be used in the numerical simulations as a sweep gas inlet boundary condition is found by using $P_{O_2,sweep,(b),\exp}$ and the corresponding oxygen permeation rate, $J_{O_2,\exp}$, by rearranging expression Eq. 3-17,

$$V_{sweep} = J_{O_2,\exp}\left(\frac{1}{P_{O_2,sweep,(b),\exp}\big/P^{\circ}} - 1\right)$$ **Eq. 3-18**

Nitrogen is used as a sweep gas, and the species boundary condition at the sweep gas inlet is,

$$Y_{k,sweep} = \begin{cases} 1 & (k = N_2) \\ 0 & (k \neq N_2) \end{cases}$$ **Eq. 3-19**

Both feed air and sweep gases are introduced at the membrane temperature assuming isothermal conditions in the experiments.

$$T_{feed} = T_{sweep} = T_{mem,\exp}$$ **Eq. 3-20**

By imposing the permeation rate measurements and the corresponding experimental conditions in my numerical model, I computed the local oxygen partial pressures, $P_{O_2,feed,(s)}$ and

$P_{O_2,sweep,(s)}$, at each operating condition in **Table 3-1**.

Table 3-1 Experimental conditions for oxygen permeation rate measurements by [31]

Parameter		Unit	Value
Membrane thickness	L	[cm]	0.399
Oxygen partial pressure at the feed air inlet	$P_{O_2,feed,(b),\exp}$	[atm]	0.21 ~ 1.0
Oxygen partial pressure at the sweep gas outlet	$P_{O_2,sweep,(b),\exp}$	[atm]	$4.6\times10^{-4} \sim 2.3\times10^{-3}$
Membrane temperature	T_{mem}	[K]	1023 ~ 1223

3.3.2. Evaluation of $D_{V_O^{\bullet\bullet}}$, k_f and k_r for oxygen transport expression

The local oxygen partial pressures computed by my numerical model and the membrane temperature are used to evaluate the diffusion coefficient of oxygen vacancies and the surface exchange reaction rates, that is, the six parameters in expression Eq. 3-12 to account for the local flow variations, using a nonlinear regression analysis. The multivariable nonlinear regression solver in Matlab is used for parameterization. Since the diffusivity of oxygen vacancy has been well characterized, its value is controlled to maintain within the range of experimental values. $D_{V_O^{\bullet\bullet}}$, k_f and k_r derived from the analysis are shown in **Table 3-2** and **Figure 3-2**, where they are compared with the values estimated on the basis of using the bulk stream parameters reported in [31]. Note that the values reported in this table are fitted against the permeation rate measurement and may need to be compared with the parameters measured experimentally, which is not available in the literature.

Table 3-2 Pre-exponential factors and activation energies of $D_{V_O^{\bullet\bullet}}$, k_f and k_r: (a) accounting for the local flow variations (based on $P_{O_2,feed,(s)}$ and $P_{O_2,sweep,(s)}$) computed by the numerical simulation and (b) evaluated by bulk stream parameters ($P_{O_2,feed,(b),\exp}$ and $P_{O_2,sweep,(b),\exp}$) by [31]

Parameter	Pre-exponential factor, ψ			Activation energy, E_A [J/mol]	
	Unit	Value			
		(a)	(b)	(a)	(b)
$D_{V_O^{\bullet\bullet}}$	[cm^2/s]	$1.01 \pm 0.05 \times 10^{-2}$	1.58×10^{-2}	$7.56 \pm 0.05 \times 10^{4}$	7.36×10^{4}
k_f	[cm/atm$^{0.5}$/s]	$9.21 \pm 0.44 \times 10^{8}$	5.90×10^{6}	$2.68 \pm 0.005 \times 10^{5}$	2.27×10^{5}
k_r	[mol/cm^2/s]	$1.75 \pm 0.087 \times 10^{11}$	2.07×10^{4}	$3.77 \pm 0.004 \times 10^{5}$	2.41×10^{5}

The results confirm that the local variations of the oxygen partial pressure should be considered when constructing an oxygen transport model for use in reactive flow studies. The pre-exponential factor, ψ, of the surface exchange reaction rates (k_f and k_r) is substantially larger than that obtained on the basis of using the bulk oxygen partial pressures in the permeation flux. As shown in **Figure 3-1**, when the local oxygen concentrations at the surface ((b) and (e) in **Figure 3-1**) are considered, the chemical potential gradient is smaller than that determined by the bulk oxygen partial pressures. With respect to activation energy of the surface exchange reaction rates, they remain nearly the same. Because the activation energy accounts primarily for the dependency of the reaction rates on temperature, its magnitude does not vary significantly when the same temperature is used in its evaluation. The pre-exponential factor and the activation energy of the diffusion coefficient also remain essentially the same.

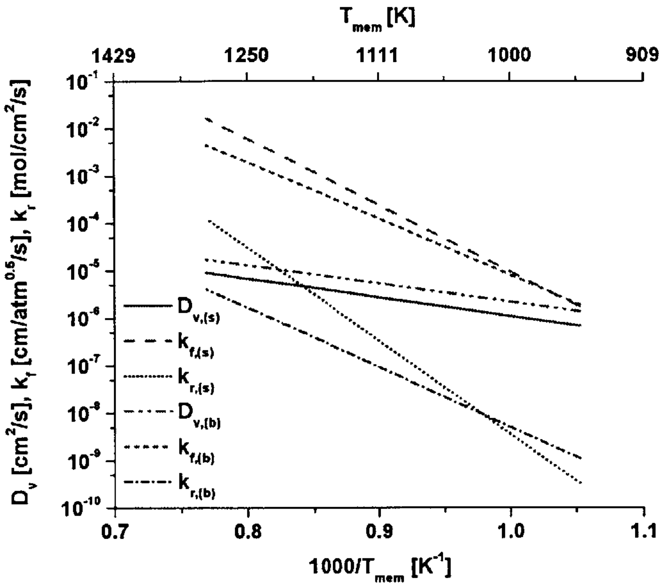

Figure 3-2 The variations of the diffusion coefficient of oxygen vacancies and the reaction rates of surface exchange with changes in the membrane temperature ($D_{V_O^{\bullet\bullet},(s)}$, $k_{f,(s)}$ and $k_{r,(s)}$ computed by $P_{O_2,(s)}$ using the numerical model and $D_{V_O^{\bullet\bullet},(b)}$, $k_{f,(b)}$ and $k_{r,(b)}$ estimated by $P_{O_2,(b),\mathrm{exp}}$ reported in [31])

The fact that the coefficients in the oxygen transport expression pertaining to $D_{V_O^{\bullet\bullet}}$, k_f and k_r depend on whether the bulk or the local oxygen partial pressures are used to estimate them highlights the importance of a spatially resolved oxygen partial pressure field and the local oxygen partial pressure in the vicinity of membrane surfaces. The oxygen transport expression should be evaluated by the local oxygen partial pressure. If the oxygen transport expression is based on the oxygen partial pressure at bulk streams as used in previous research, the model cannot predict the oxygen concentration profile in ITM reactors where significant local flow variations exist.

3.4. Factors influencing oxygen transport

The numerical model supplemented with the oxygen permeation flux properly parameterized can be used to examine oxygen transport and other processes in membrane supported flows. In typical experimental investigations, the measurement tools are limited and results are shown as function of the bulk stream data which may not be reflective of the local conditions at the membrane surface, especially in the reactive cases. Here I use my spatially resolved model to examine the dependency of the process on different operating parameters including the membrane temperature, feed and sweep gas flow rates, geometry and oxygen concentration in the feed stream. The base-case parameters and the range of their variations in the parametric study are summarized in **Table 3-3**. Moreover, the effects of chemical reactions on oxygen transport are discussed. To highlight the importance of local flow variations, the oxygen permeation flux, $J_{O_2,(s)}$, evaluated by the local oxygen partial pressure, $P_{O_2,(s)}$, is compared to that of bulk parameters, $J_{O_2,(b)}$ and $P_{O_2,(b)}$. The spatially resolved numerical model calculates the local oxygen partial pressure, $P_{O_2,(s)}$, and the corresponding permeation rate, $J_{O_2,(s)}$. Next, the bulk oxygen partial pressure, $P_{O_2,(b)}$, is post-processed assuming perfect mixing between the permeated oxygen and the sweep gas, which is the method used in experiments to estimate the permeation rate. By using this bulk oxygen partial pressure, I calculate $J_{O_2,(b)}$.

Table 3-3 Flow parameters used in the parametric study ($\mathrm{Re}_{feed} = \frac{V_{feed}H_{feed}}{\mu_{feed}}$ and $\mathrm{Re}_{sweep} = \frac{V_{sweep}H_{sweep}}{\mu_{sweep}}$)

Parameter		Unit	Base-case value	Range of variations	
				Min	Max
Membrane temperature	T_{mem}	[K]	1100	950	1300
Sweep gas flow rate	V_{sweep}	[kg/m^2/s]	0.1 (Re_{sweep} = 42.92)	0.005 (Re_{sweep} = 2.146)	3.0 (Re_{sweep} = 1287.6)
Feed gas flow rate	V_{feed}	[kg/m^2/s]	0.1 (Re_{feed} = 111.38)	0.001 (Re_{feed} = 1.114)	1.0 (Re_{feed} = 1113.8)
Channel height from membrane to sweep gas inlet	H_{sweep}	[mm]	25.4 (Re_{sweep} = 42.92)	5.0 (Re_{sweep} = 8.449)	70 (Re_{sweep} = 118.29)
Oxygen concentration in feed air	$Y_{O_2,feed}$	[atm]	0.21	0.21	1.0
Membrane thickness	L	[mm]	1.0	--	--
Channel height from membrane to feed gas inlet	H_{feed}	[mm]	50.8	--	--

3.4.1. Membrane temperature

The high sensitivity of $D_{V_O^{\bullet\bullet}}$, k_f and k_r to temperature is shown in **Figure 3-2**. The resistances of surface exchange kinetics and bulk diffusion to oxygen permeation are reduced significantly with increasing the membrane temperature. According to the lower resistances, the permeation rate increases by nearly four orders of magnitude for a temperature rise from 950K to 1300K, as shown in **Figure 3-3**(a). However, beyond a certain point, the sensitivity of oxygen permeation to temperature starts to decrease. This can be explained by the different activation energies of the surface exchange reaction rates and the diffusion coefficient of oxygen vacancies.

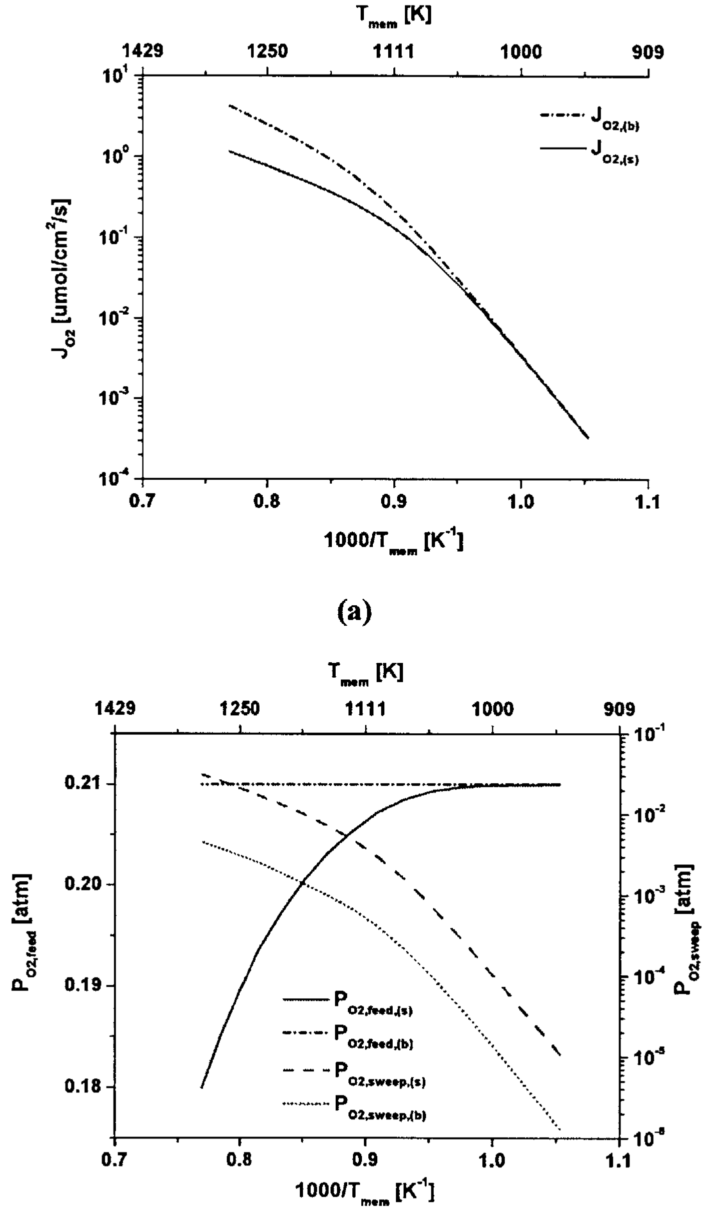

(a)

(b)

Figure 3-3 Influences of membrane temperature on: (a) the oxygen permeation rate and (b) the oxygen partial pressure

As shown in **Figure 3-2**, the slope of $D_{V_O^{\bullet\bullet}}$ is substantially lower than that of k_f and k_r. As the temperature is raised, the diffusion coefficient of oxygen vacancies becomes limiting factor in oxygen transport [31].

Figure 3-3(a) shows two different oxygen permeation rates evaluated using the oxygen transport expression based on the oxygen partial pressures at the bulk stream, $J_{O_2,(b)}$, or the local partial pressures at the membrane surface, $J_{O_2,(s)}$, respectively. The figure shows that the dependence on the membrane temperature is weaker when the oxygen permeation rate is described in terms of the local partial pressure. An increasing membrane temperature leads to a larger permeation rate that accounts for a sink and a source term for the feed domain and the permeate domain, respectively. However, the permeation flux and partial pressures are coupled (see **Figure 3-3**(b)). The local oxygen partial pressure in the feed side decreases and that of the permeate side increases due to the higher permeation rate, and reduces the chemical potential gradient across the membrane, as shown in **Figure 3-4**, We note here that, experimentally, the bulk stream pressure is a mean value measured in the exiting stream. As shown in **Figure 3-4**, the oxygen partial pressures change significantly from the membrane surface to the inlet in the permeate domain. Assuming complete mixing in the sweep gas at the exit section, the measured pressure is lower than that at the membrane surface, increasing the apparent partial pressure difference between the two sides and hence not accurately accounting for the dependency of the permeation flux on that parameter.

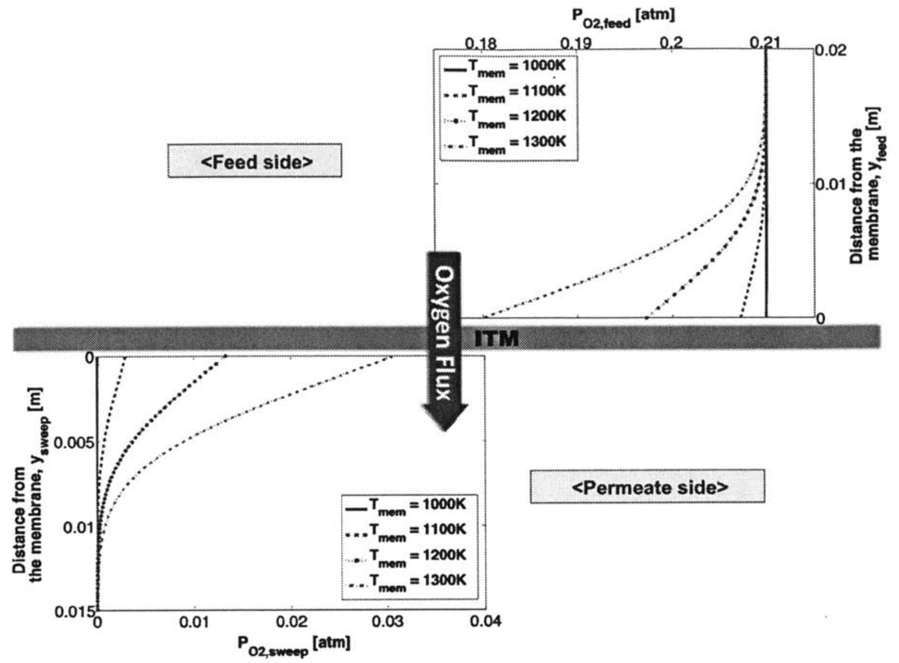

Figure 3-4 Spatially resolved oxygen partial pressure profiles as a function of the membrane temperature

3.4.2. Feed and sweep gas flow rates

Given the significant impact of the gas phase mass transfer on oxygen transport, it is of interest to consider the impacts of the feed and sweep gas flow rates. **Figure 3-5** shows that the permeation rate increases significantly as the sweep gas flow rate is raised. As shown in **Figure 3-5**, the spatially averaged parallel velocity on the permeate side increases linearly as the sweep gas flow rate is raised, lowering the oxygen partial pressure. However, the rate of change in the permeation rate and the oxygen partial pressure become smaller as the sweep gas flow rate increases. It can be explained by the spatially resolved partial pressure profiles shown in **Figure 3-6**. As the sweep gas flow rate increases, the boundary layer is restricted to a narrow region in the vicinity of the membrane surface. As a result, the oxygen transport becomes less dependent on the sweep gas flow rates.

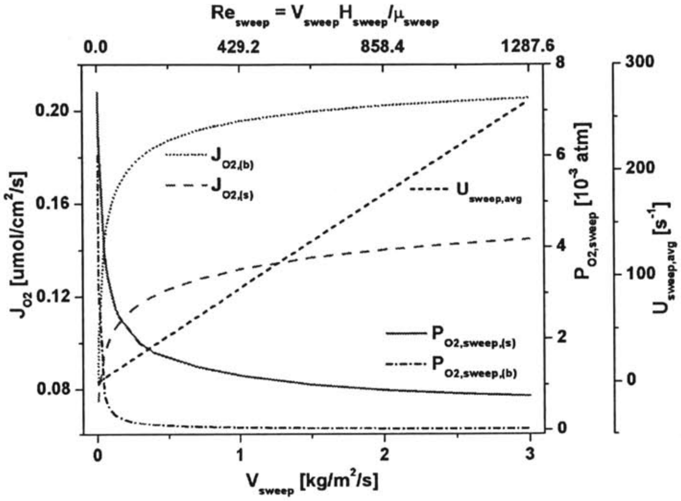

Figure 3-5 The effects of sweep gas flow rate on the oxygen permeation rate, the oxygen partial pressure on the sweep gas side and the spatially averaged parallel velocity on the sweep gas side, $U_{sweep,avg} = \dfrac{1}{H_{sweep}} \int_0^{H_{sweep}} U_{sweep}(t,y)\,dy$

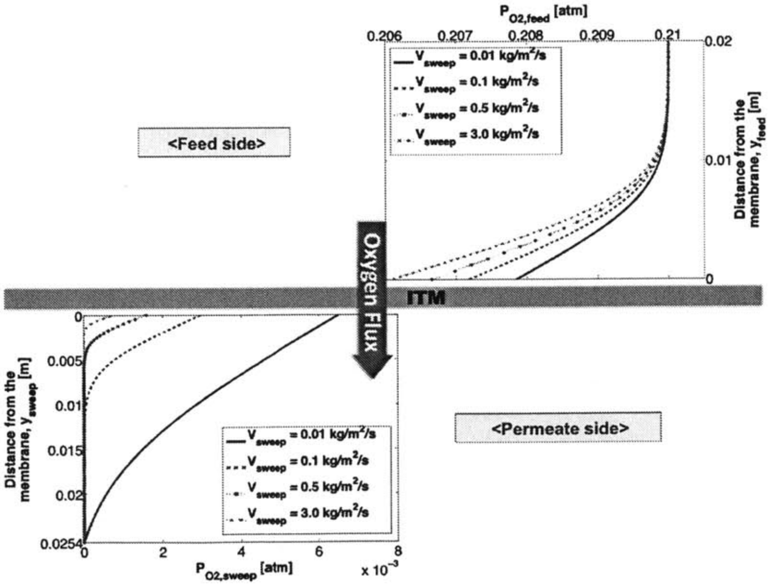

Figure 3-6 Spatially resolved oxygen partial pressure profiles as a function of the sweep gas flow rate

On the other hand, the permeation rate is much less dependent on the feed gas flow, as shown in **Figure 3-7**. At 1100 K (base-case temperature), the forward surface exchange rate, k_f, is higher than both $D_{V_O^{\bullet\bullet}}$ and k_r, as shown in **Figure 3-2**, and hence the permeation is limited by the bulk diffusion or the surface exchange kinetics on the permeate side. Thus, although the effects of the gas phase mass transfer in the feed side is reduced by the higher momentum (see **Figure 3-7**), the oxygen permeation rate is hardly affected by an increase in the local oxygen partial pressure. This can also be seen in the spatially resolved partial pressure profiles shown in **Figure 3-8**. Whereas the feed side oxygen concentration profiles vary substantially as the feed gas flow rate increases, the oxygen partial pressure in the permeate side does not change, which represents negligible changes in the permeation rate.

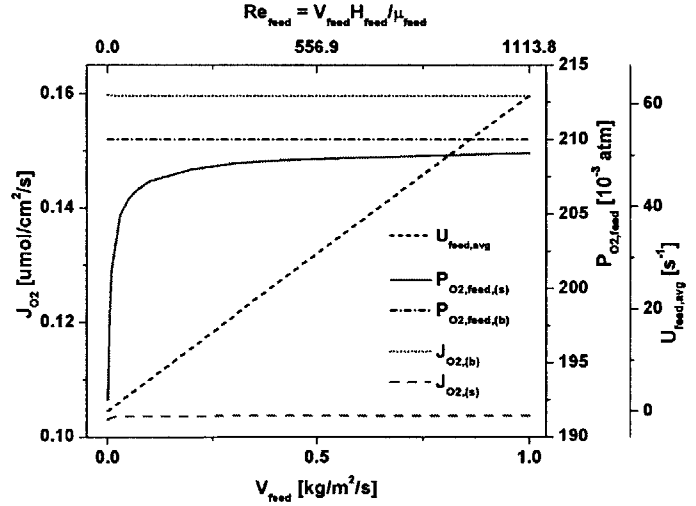

Figure 3-7 The effects of feed air flow rate on the oxygen permeation rate, the oxygen partial pressure on the feed side and the spatially averaged parallel velocity on the feed side,

$$U_{feed,avg} = \frac{1}{H_{feed}} \int_0^{H_{feed}} U_{feed}(t,y)\,dy$$

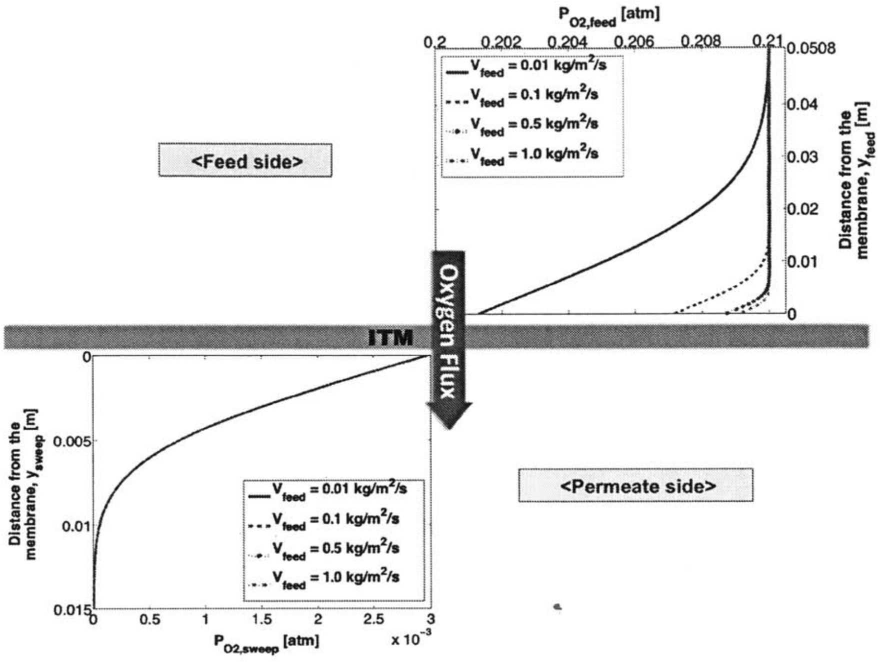

Figure 3-8 Spatially resolved oxygen partial pressure profiles as a function of the feed air flow rate

Ignoring gas phase mass transfer is valid only at high gas flow rates. As shown in **Figure 3-6**, the boundary layer on the permeate side is reduced to a narrow region near the membrane surface when the sweep gas flow rate is raised. In this case, gas phase mass transfer is negligible, and the bulk stream oxygen partial pressure can be used to asymptotically approximate the local oxygen partial pressure (see **Figure 3-5**). However, as discussed in Section 3.2.1.1, the flow rate in ITM reactors is limited by the required stoichiometry of the chemical reactions.

Comparing **Figure 3-3**(a) and **Figure 3-5**, it can be shown that gains in the permeation rate by increasing the gas flow rates are much smaller than those induced by heating the membrane. The fact that the oxygen permeation rate is weakly dependent on the gas phase flow makes it less efficient to increase the flow rate for enhancing the oxygen permeation rate given that high gas flow rates introduce more pressure drop.

3.4.3. Geometry – channel height from membrane to sweep gas inlet

To further investigate the dependence of the oxygen permeation rate on the permeate side gas phase mass transfer, a sensitivity analysis with respect to the channel height on the sweep gas side was conducted. A smaller channel height increases the parallel velocity (momentum) on the permeate side reducing the mass transfer effect. In the parametric investigation of the geometry, the sweep gas flow rate is maintained constant. As shown in **Figure 3-9**, the local oxygen partial pressure, $P_{O_2,sweep,(s)}$, is lowered with the channel height, enhancing the flux and highlighting the effect of momentum. Note also that the bulk stream parameters ($J_{O_2,(b)}$ and $P_{O_2,sweep,(b)}$) vary in the opposite direction to that of the local flow parameters ($J_{O_2,(s)}$ and $P_{O_2,sweep,(s)}$) with respect to the geometry. Since bulk oxygen partial pressure measured at the exit stream is determined assuming perfect mixing of the permeated oxygen with the sweep gas (refer to expression Eq. 3-17), its value increases when oxygen permeation is enhanced by reducing the gap height, lowering the apparent bulk stream oxygen partial pressure as opposed to the results based on the local oxygen partial pressures.

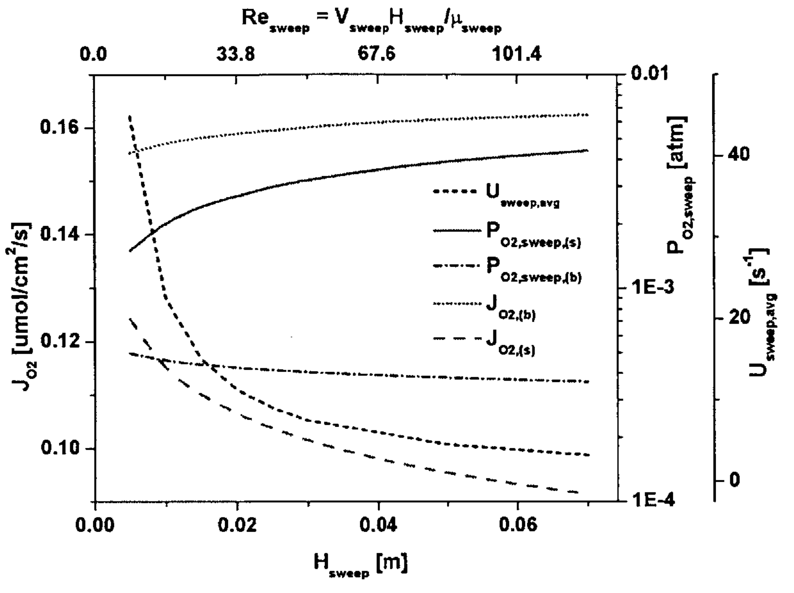

Figure 3-9 The effects of geometry (channel height from the membrane to the sweep gas inlet) on the oxygen permeation rate, the oxygen partial pressure on the sweep gas side and the spatially averaged parallel velocity, $U_{sweep,avg} = \frac{1}{H_{sweep}} \int_0^{H_{sweep}} U_{sweep}(t,y)dy$

3.4.4. Oxygen concentration in feed air

An increase in the oxygen permeation flux with the oxygen concentration in the feed air is obvious, as discussed in Section 3.2. In this study, I assume that both feed and permeate domains are at the same operating pressure, which results in no total pressure difference across the ITM, for mechanical stability. The permeation rate increases when the oxygen partial pressure in the feed air is higher. Note that the effects of gas phase mass transfer in the feed domain are negligible (for the configurations considered in this investigation), as discussed in Section 3.4.2. Therefore, a larger oxygen partial pressure in the feed air directly increases the local oxygen partial pressure near the membrane surface. Gains in the permeation rate are larger than those induced by the feed gas flow rates, but not as large as those earned by increasing the membrane temperature.

3.4.5. Chemical reactions

To capture the effect of chemical reactions on oxygen transport across the membrane, a reactive gas (CH_4) is introduced into the permeate side with diluents (CO_2). Other flow parameters are maintained at the base-case values as listed in **Table 3-3**. We note here that to support combustion on the permeate side in the form of a diffusion flame, a substantial amount of oxygen is required. A diffusion flame is established in the region of unity stoichiometry. To achieve a significant oxygen permeation flux for the oxidation reactions, in this study, it is assumed that the feed and sweep gases are introduced at 1300K. Low oxygen concentration due to low permeation would make it necessary to use a higher dilution ratio (for instance CH_4:CO_2 = 1:40 on a molar basis) in order to sustain a diffusion flame. To highlight the impacts of oxidation reactions, the results are compared with those of inert gas.

Oxidation reactions in the permeate side change the oxygen concentration profile as well as the membrane temperature. The oxygen permeation flux increases in reactive environment because oxygen concentration in the permeate side is reduced by consumption in the reaction zone. If the diffusion flame is established in the vicinity of the membrane, the effect of lowering the oxygen concentration is enhanced and the permeation rate increases further. **Figure 3-10** shows that this is indeed the case, and the reaction zone is located a few millimeters away from the membrane. Oxidation reactions in this region reduce the oxygen concentrations compared to the inert gas case, as shown in **Figure 3-11**. Furthermore, compared to the inert gas case in which no temperature variations is seen, the membrane in the reactive environment conducts heat from the permeate to the feed sides. The heat released at the reaction zone is transferred to the membrane, as well as to the feed side, raising its temperature, and further enhancing the oxygen permeation flux. Thus, in a reactive flow, lower oxygen concentration (resulting in $\Delta J_{O_2} = 1.49 \times 10^{-1} \mu mol / cm^2 / s$) and higher membrane temperature (leading to $\Delta J_{O_2} = 1.00 \mu mol / cm^2 / s$) enhance the oxygen permeation flux. In comparison with the inert gas case ($J_{O_2} = 1.15 \mu mol / cm^2 / s$), in the reactive case, the permeation rate is $J_{O_2} = 2.30 \mu mol / cm^2 / s$.

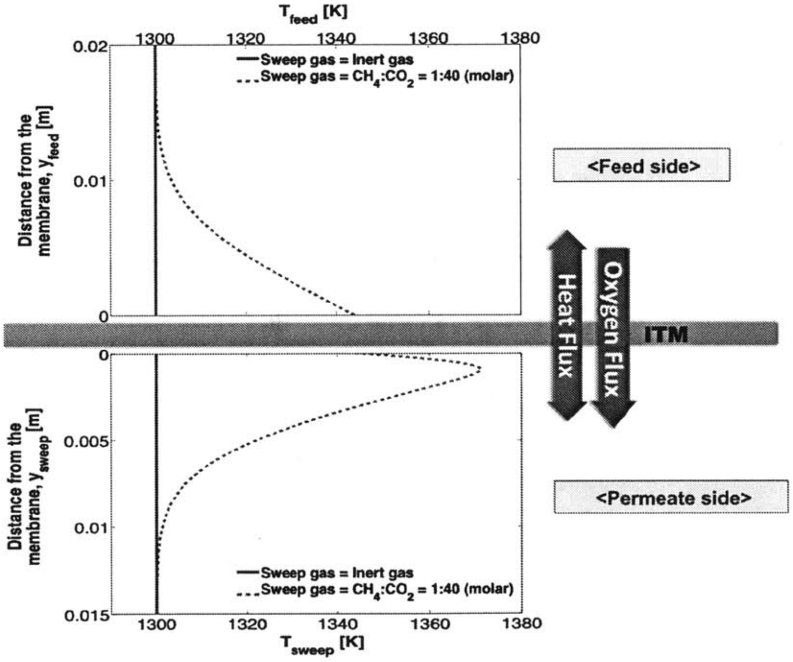

Figure 3-10 Temperature variations when sweep gas is inert gas or reactive gas

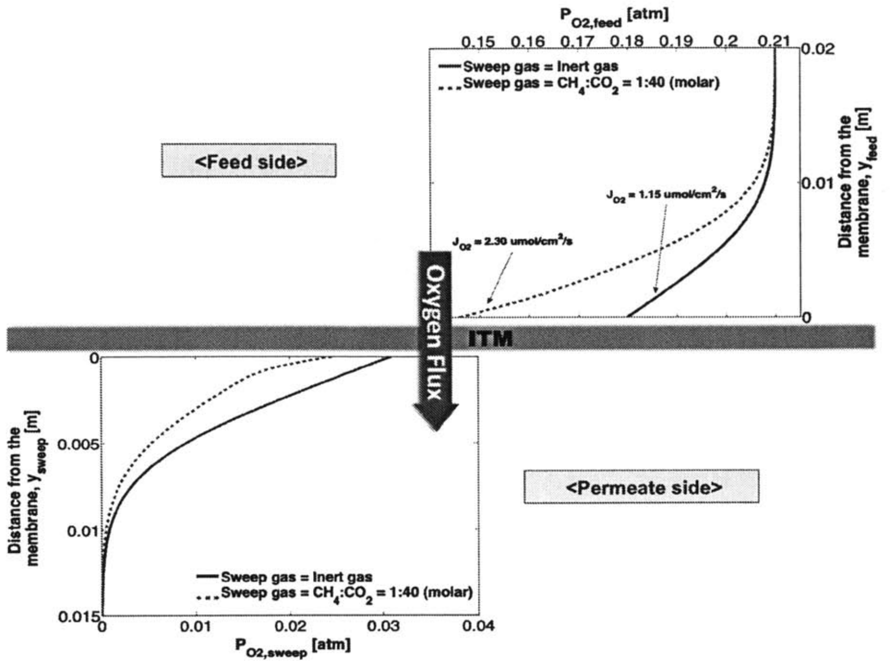

Figure 3-11 Spatially resolved oxygen partial pressure profiles when sweep gas is inert gas or reactive gas

Partial oxidation and fuel pyrolysis are also seen on the permeate side, as reported in [45, 51, 79-81]. When fuel is introduced into a high temperature reactor without oxygen, the decomposition and pyrolysis of fuel proceed rather than combustion. The oxygen permeation rate and hence the oxygen concentration on the permeate side are rather low, resulting in a fuel-rich environment in the reaction zone. In this case, instead of being fully converted to carbon dioxide (complete combustion), methane is partially oxidized to form synthesis gas composed of carbon monoxide and hydrogen, as follows.

$$CH_4 + \frac{1}{2}O_2 \rightarrow CO + 2H_2 \qquad \textbf{Eq. 3-21}$$

Figure 3-12(a) shows the spatially resolved species concentrations. Within the reaction zone, fuel-rich conditions are established, and the partial oxidation of fuel produces carbon monoxide and hydrogen. Note that the fuel stream is highly diluted by carbon dioxide. Methane is reformed to produce carbon monoxide and hydrogen by carbon dioxide reforming reaction as shown below.

$$CH_4 + CO_2 \rightarrow 2CO + 2H_2 \qquad \textbf{Eq. 3-22}$$

Moreover, methane is decomposed and pyrolyzed before reaching the reaction front at 1300K, as shown in **Figure 3-12**(b). Fuel pyrolysis may result in soot formation and carbon deposition on the membrane surface [82]. Deposited carbon degrades the membrane activity including oxygen permeation. Rigorous investigation on these phenomena will be conducted using the current model. The location of the reaction zone along with fuel pyrolysis shows the importance of possible heterogeneous reactions on the membrane surface [83]. It has been reported that typical mixed-conducing ion transport membranes exhibit catalytic activities [20]. This is another phenomenon that will be investigated in a subsequent work.

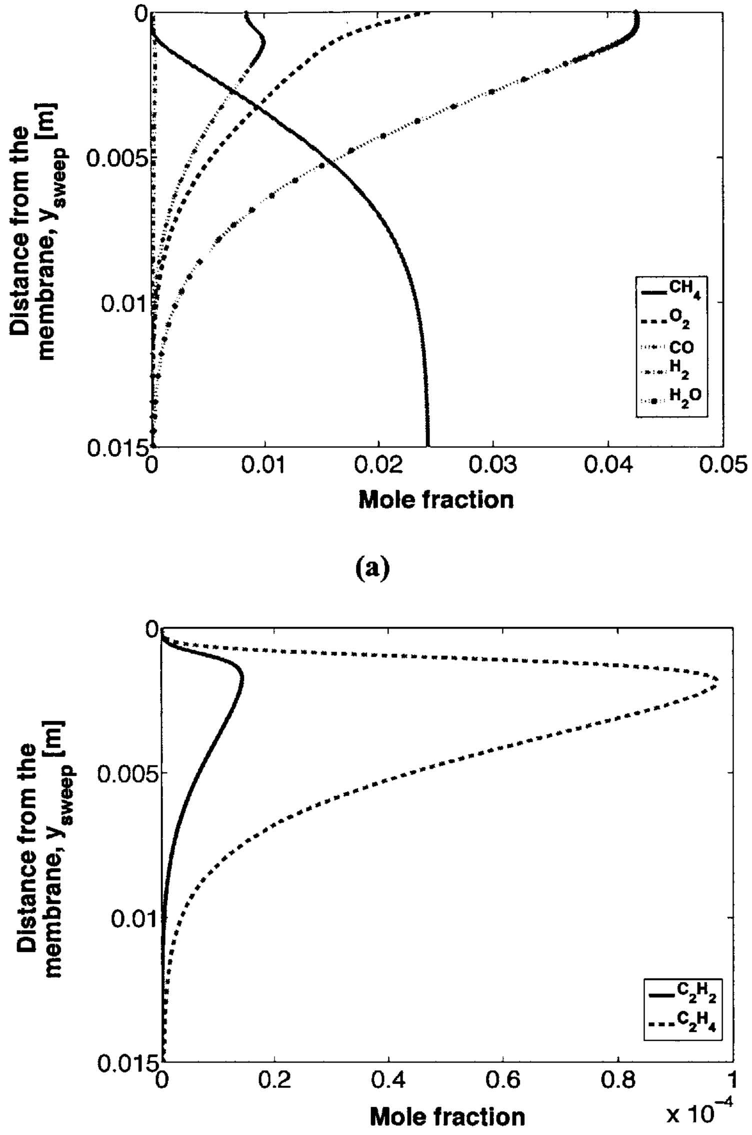

(a)

(b)

Figure 3-12 Influences of chemical reactions on the species concentration variations when a reactive gas is used as a sweep gas: (a) major species including CH_4, O_2, CO, H_2, and H_2O, and (b) soot precursors including C_2H_2 and C_2H_4

3.5. Conclusions

I used available experimental data and the numerical model to obtain an expression for the oxygen permeation flux in terms of the oxygen partial pressure at the membrane surface on both sides. I demonstrated that this is a more accurate and general representation that allows the application of the resulting expression over a wider range of conditions. I showed that neglecting the impact of mass transfer in parameterizing the dependency of the permeation flux on the operating conditions may lead to errors. The flux expression accounts for the adsorption/desorption kinetics and the diffusion across the membrane. The values of the parameters $D_{V_O^{\bullet\bullet}}$, k_f and k_r evaluated using the local oxygen partial pressures confirm that the local variations should be considered when constructing an oxygen transport model.

The resulting model was then used to examine the impact of the operating conditions, such as the membrane temperature, feed and sweep gas flow rates, geometry, oxygen concentration in the feed air and chemical reactions on oxygen transport. The oxygen permeation rate depends most strongly on the membrane temperature, but also on the gas flow rates and the channel height on the permeate side. Moreover, a lower oxygen concentration in the permeate side and a higher membrane temperature resulting from fuel oxidation reactions on the permeate side enhance the oxygen permeation rate. A reaction zone located in the vicinity of the membrane consumes the permeated oxygen and reduces its partial pressure. A high temperature and low oxygen concentration environment may also result in the partial oxidation and/or the pyrolysis of fuel. The latter is a subject of current studies.

Chapter 4 Flame Analysis

4.1. Overview

Fuel conversion processes on the sweep side of the ITM have important features that should be investigated for reaction selectivity. The nature of oxygen permeation across the membrane does not enable pre-mixing fuel and oxygen, which results in the establishment of a non-premixed (diffusion) flame in the absence of nitrogen. In a diffusion flame, the state of the reactants is critical for defining the response of the flame to strain rates and controlling the reaction products. On the sweep side of the ITM, the sweep gas stream, i.e., the fuel stream, tends to be preheated and to require diluents such as CO_2 and H_2O along with the fuel in order to control the flow rate and the flame temperature [52, 84]. In addition, the oxygen permeation flux, i.e., the oxidizer stream, is influenced by oxygen consumption and heat released from the oxidation reactions, which affect the oxygen concentration in the immediate vicinity of the membrane and the membrane temperature. Thus, the oxidation reactions and flow conditions near the membrane are highly important for determining the flow rate of the oxidizer, i.e., oxygen permeation rate. The reaction environment on the sweep side of the ITM is different from that in conventional diffusion controlled combustion. Modeling studies are needed to investigate fuel conversion processes and to control reaction selectivity.

In this chapter, fuel conversion and some important features (e.g., the flame location, temperature, thickness and structure) of a non-premixed flame established on the sweep side of an ITM are investigated. It is assumed that no additional catalyst is mounted on the membrane, and the membrane surface is not catalytically active for hydrocarbon or syngas conversion so that the impact of the homogeneous phase reactions can be independently considered. Dry CO_2 is assumed as the diluent in the sweep gas stream with CH_4 as a fuel, and results are compared with those in which the fuel is diluted with N_2. I examine the chemical reactions occurring on the sweep side of the ITM and their effects on the reaction products, flame structure and oxygen permeation rate. In addition, important phenomena such as hydrocarbon pyrolysis and the formation of possible soot precursors are discussed.

4.2. Reaction environment supported by an ITM

The presence of a dense ceramic membrane between the air and sweep gas inlets leads to several particular characteristics concerning the fuel conversion processes on the sweep side of an ITM, as compared to the classical opposed-flow diffusion flames. First, oxygen selectively permeates from the air side to the sweep side. In the absence of diluents (other than nitrogen) in the sweep side, this forms a nitrogen-free environment for the chemical reactions. Nitrogen is completely removed prior to combustion, and oxy-fuel combustion takes place without NO_x formation. However, the flame temperature in the absence of nitrogen, i.e., oxy-fuel flame, is significantly higher compared to that of CH_4/air combustion. Matching the combustion temperature requires the introduction of a substantial amount of another diluent such as CO_2 or H_2O in the sweep gas stream [7]. In typical oxy-fuel combustion reactors, a fraction of the flue gas stream is recirculated back to the reactor in the form of wet or dry CO_2 to control the flame structure and its temperature. In this study, dry CO_2 recycle is assumed, and it is mixed with CH_4 as a sweep gas stream, which is also considered in experiments [65]. Note that CO_2 is mixed and fed into the reactor along with CH_4, rather than being mixed with oxygen, i.e., the process relies on fuel dilution rather than oxidizer dilution. Since oxygen is introduced into the sweep side of the ITM via permeation, pre-mixing of the recirculated CO_2 stream with oxygen is not possible. This will affect fuel pyrolysis, which will be discussed in Section 4.3.4. In an environment with a mixture diluted by CO_2, the thermodynamic and transport properties of gases change greatly from those of a mixture diluted by N_2, i.e., air. CO_2 is a tri-atomic molecule with the higher specific heat capacity and molecular weight than the diatomic N_2 molecule. A higher molecular weight raises the gas density and hence the density-weighted diffusion coefficients, i.e., ρD_k, of the fuel and oxidizer, i.e., permeated oxygen in the gas-phase. In addition, the chemical effects of CO_2 driven by its reduction reaction with the H radical become important [85, 86]. These effects also become apparent in an ITM reactor as will become evident in Section 4.3.

The oxygen permeation flux across the membrane is relatively low compared to the convective oxidizer feed stream in conventional counter-flow diffusion flames. The stream velocity in typical opposed-flow diffusion flames is on the order of 10^{-1}~1 m/s [68, 87], whereas that in the ITM reactor is limited by low oxygen permeation rates, which is on the order of 10^{-1}~1 μmol/cm^2/s [61] or 10^{-4}~10^{-3} m/s. Accordingly, the fuel stream must be fed to the sweep side at a low flow rate to satisfy the requisite stoichiometry and stabilize the reaction zone between the membrane and the sweep gas inlet. The corresponding Reynolds number for the sweep side, which is defined as below, is on the order of 10.

$$\mathrm{Re}_{sweep} = \frac{\rho_{sweep} v_{sweep} H_{sweep}}{\mu_{sweep}} = \frac{V_{sweep} H_{sweep}}{\mu_{sweep}} \qquad \textbf{Eq. 4-1}$$

where H_{sweep} is the sweep gas channel height of the reactor. Therefore, the species transport by diffusion is important in this low Reynolds number regime, which further highlights the implications of a CO_2-diluted (rather than N_2-diluted) sweep gas stream. The species diffusion is also critical with respect to the oxygen permeation rate, as will be discussed in Section 4.3.1. In addition, the air and sweep gas streams are preheated to a high temperature to enhance the oxygen permeation flux and promote the gas-phase kinetics, as the former is predominantly dependent on the membrane temperature and the oxygen partial pressure on the sweep side of the ITM.

Lastly, the flow rate of the oxidizer, i.e., the oxygen permeation rate, is not a predetermined or controlled parameter, but it is a dependent variable. Unlike conventional counterflow diffusion flames where the oxidizer flow rate can be controlled explicitly, the oxygen permeation rate is not known a priori and depends on the local oxygen partial pressure in the immediate vicinity of the membrane and membrane temperature [12]. These two parameters are strongly influenced by the oxidation reactions and cannot be independently manipulated. Furthermore, the overall reaction rate and reaction products/selectivity are dependent on the oxygen permeation rate, which is also affected by the chemical reactions. Non-premixed, diffusion-limited reactions occurring on the sweep side are governed by the oxidizer flow rate, i.e., the oxygen permeation rate, as well as the sweep gas initial conditions (e.g., flow rate, initial temperature and fuel concentration). Thus, it is difficult to control the oxygen permeation flux, the mass ratio of oxygen to fuel, i.e., equivalence ratio, and reaction products independently. The operating regime of ITM reactors and associated fuel conversion processes need to be examined using detailed models capable of resolving each of these processes to gain understanding of the complex coupling.

4.3. Fuel conversion and flame analysis

To gain insight into the fuel conversion process, a reference operating condition was defined and the flame, oxygen permeation, chemical kinetics, and thermodynamic characteristics were evaluated. The following results were obtained for a sweep gas fuel concentration of 6% on a molar basis, with the remainder being CO_2, and a sweep gas mass flux of 3.00×10^{-2} kg/m^2/s, corresponding to $Re_{sweep} = 15.6$ and sweep gas inlet velocity = 7.56×10^{-2} m/s. In addition, it is assumed that the sweep gas stream is preheated to 1300 K in order to obtain a high oxygen permeation rate. These conditions were selected because they are within the realistic operating regime of an ITM unit and allow a sustainable reaction zone to be established. To characterize the impacts of fuel dilution using CO_2 sweep gas stream, the results are compared to those of a N_2-diluted sweep fuel stream in which the Damköhler number (defined as a ratio of the extinction strain rate to the flow strain rate), the fuel concentration on a mass basis in the sweep gas stream and the initial temperature are the same as those of the CO_2-dilution case. Since a diffusion flame structure appears in a complicated coupled manner between thermal input, species transport and chemical kinetics, and is strongly sensitive to the flame regime in Linan's S-curve, the Damköhler number is maintained constant for comparison. Note that, since the temperature on the sweep side of the ITM is sufficiently low, N_2 chemistry does not have significant effects on the flame. The mass flux of air is maintained at 1.00×10^{-1} kg/m^2/s, corresponding to $Re_{air} = 100$ and air inlet velocity = 3.70×10^{-1} m/s, for both cases. It is assumed that the air is preheated to 1300 K, and the surrounding wall temperature is the same as the gas (i.e., both air and sweep gas) inlet temperature. Results obtained from the CO_2-diluted sweep gas stream are categorized as a base case (CO_2-dilution), while those from the sweep gas stream diluted with N_2 are called a reference case (N_2-dilution).

4.3.1. Flame location and oxygen permeation

Low oxygen permeation rates result in a stagnation point and a flame front established in the vicinity of the membrane with weak flame stretch. The flame location is defined as the point of maximum heat release. As discussed in Section 4.2, the oxygen permeation rate from a typical ITM is substantially lower compared to the oxidizer flow rate in conventional opposed-flow diffusion flames. Given the inlet conditions, the oxygen permeation rates obtained from the simulations are 1.13×10^{-3} and 1.24×10^{-3} kg/m^2/s for CO_2-dilution and N_2-dilution cases, respectively, which are one order of magnitude lower than the sweep gas mass flux. In this case, the stagnation point and the flame front are established in the vicinity of the membrane, as shown in **Figure 4-1**.

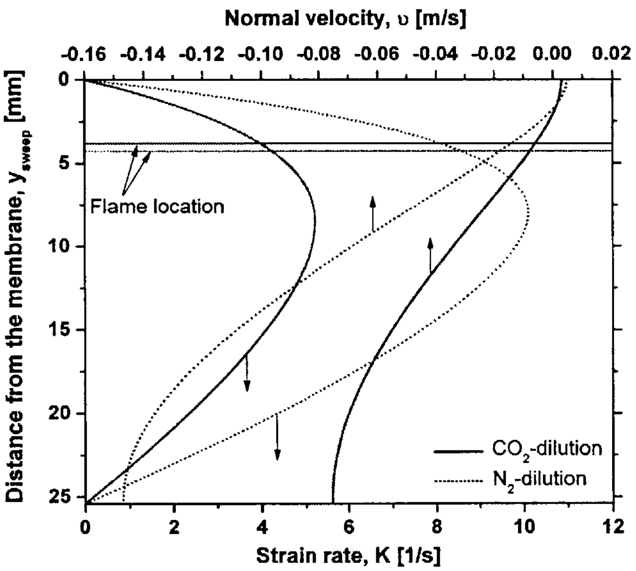

Figure 4-1 Normal velocity and strain rate along with the flame location (where, solid lines represent CO_2-dilution, and dotted lines stand for N_2-dilution). $y_{sweep} = 0$ is located on the membrane surface of the sweep side.

In addition, low strain rate flames result from the low oxygen permeation flux, as compared to the strain rate of conventional opposed-flow diffusion flames which is on the order of $10^2\sim10^3$ s^{-1} [68, 87]. The strain rate, *K*, is defined as [87],

$$K = -\frac{1}{\rho}\frac{\partial(\rho v)}{\partial y} = -\frac{1}{\rho}\frac{\partial V}{\partial y} \qquad \textbf{Eq. 4-2}$$

Figure 4-1 shows that the strain rates of both CO_2-dilution and N_2-dilution cases are close to or less than 10 s^{-1}. Furthermore, to obtain the same Damköhler number for the CO_2-dilution and the N_2-diluted fuel stream, the latter needs a higher inlet velocity resulting in a larger strain rate. The differences in the flame location, inlet velocity and strain rate between the two cases are attributed to the chemical effects and transport properties of CO_2, which will be discussed in Section 4.3.2.

The flame location and the high CO_2 concentration on the sweep side of the ITM play important roles in determining the oxygen permeation rate and the flame temperature. **Table 4-1** summarizes the results regarding the flame location and several critical parameters in this problem. Since the reaction zone is established close to the membrane, the heat transfer from the flame towards the membrane is substantial, which decreases the flame temperature while increasing the membrane temperature. It can be seen that maximum flame temperature for both CO_2-dilution and N_2-dilution cases are lower than the corresponding adiabatic flame temperatures, while the membrane is heated and is maintained at a high temperature due to the heat transfer from the reaction zone. If this heat loss is extensive such that the reaction rates are significantly lowered, the flame can be even extinguished [88, 89]. Moreover, oxygen consumption and the diffusion of the reaction products towards the membrane surface and the permeated oxygen away from the surface reduce the oxygen concentration in the immediate vicinity of the ITM and increase the permeation rate. In the CO_2-dilution case, the flame front established closer to the membrane along with the enhancement of the species diffusion because of the larger density-weighted diffusion coefficients in CO_2 with respect to that in N_2 (e.g., ρD_{H_2O} = 1.10×10^{-4} and 8.94×10^{-5} kg/m/s for CO_2-dilution and N_2 dilution cases, respectively) result in a lower oxygen mass fraction at the membrane surface, in comparison with that of the N_2-dilution case.

Table 4-1 The effects of the flame location on the flame temperature and the oxygen permeation rate

Parameter	**Unit**	**Base case (CO_2 diluted sweep gas)**	**Reference case (N_2 diluted sweep gas)**
Flame location (from the membrane)	[mm]	3.82	4.28
Stagnation point (from the membrane)	[mm]	2.10	1.80
Heat transfer towards the membrane	[W/m^2]	7436	7496
Adiabatic flame temperature	[K]	1980	2056
Maximum flame temperature	[K]	1537	1589
Membrane temperature	[K]	1311	1311
Oxygen mass fraction at the membrane surface	[--]	5.01×10^{-2}	6.41×10^{-2}
Oxygen partial pressure at the membrane surface	[atm]	6.37×10^{-2}	5.65×10^{-2}
Oxygen permeation rate	[µmol/cm^2/s]	3.53	3.87

Note that oxygen permeation is enhanced as the oxygen chemical potential gradient across the membrane and the membrane temperature increase (refer to Eq. 3-11 and Eq. 3-12). A lower oxygen concentration induced by a closer flame location increases the oxygen permeation flux. However, the high molecular weight of CO_2 reduces the impact of these effects, as the oxygen permeation rate is a function of oxygen partial pressure, i.e., the O_2 mole fraction (and not mass fraction), as described in Eq. 3-11. Thus, the higher mixture molecular weight in the CO_2-dilution case translates the oxygen mass fraction to a higher oxygen partial pressure in the vicinity of the membrane than when N_2 dilution is used. As a result, the permeation rate in the N_2-dilution case is slightly larger than that of the CO_2-dilution case, despite the CO_2-dilution case having a lower oxygen mass fraction in the vicinity of the membrane.

4.3.2. Flame temperature and thickness

Fuel conversion processes on the sweep side of the ITM show a number of important features regarding the temperature and thickness of the flame. **Figure 4-2**(a) shows the temperature for both CO_2-dilution and N_2-dilution cases, in the direction normal to the membrane. It can be seen that the flame temperature and its gradient in the CO_2-dilution case are lower than those of the N_2-dilution case. This can be attributed to the chemical, thermal and transport effects of CO_2 and the oxygen leakage through the flame. To examine the chemical effects of CO_2, **Table 4-2** shows dominant reactions governing the overall fuel conversion processes and the strength of each reaction, as described by the spatially averaged reaction rate, $\overline{\eta}_i$ (defined as below), for both CO_2-dilution and N_2-dilution cases.

$$\overline{\eta}_i = \frac{1}{H_{sweep}} \int_0^{H_{sweep}} \dot{\eta}_i \, dy \qquad \text{Eq. 4-3}$$

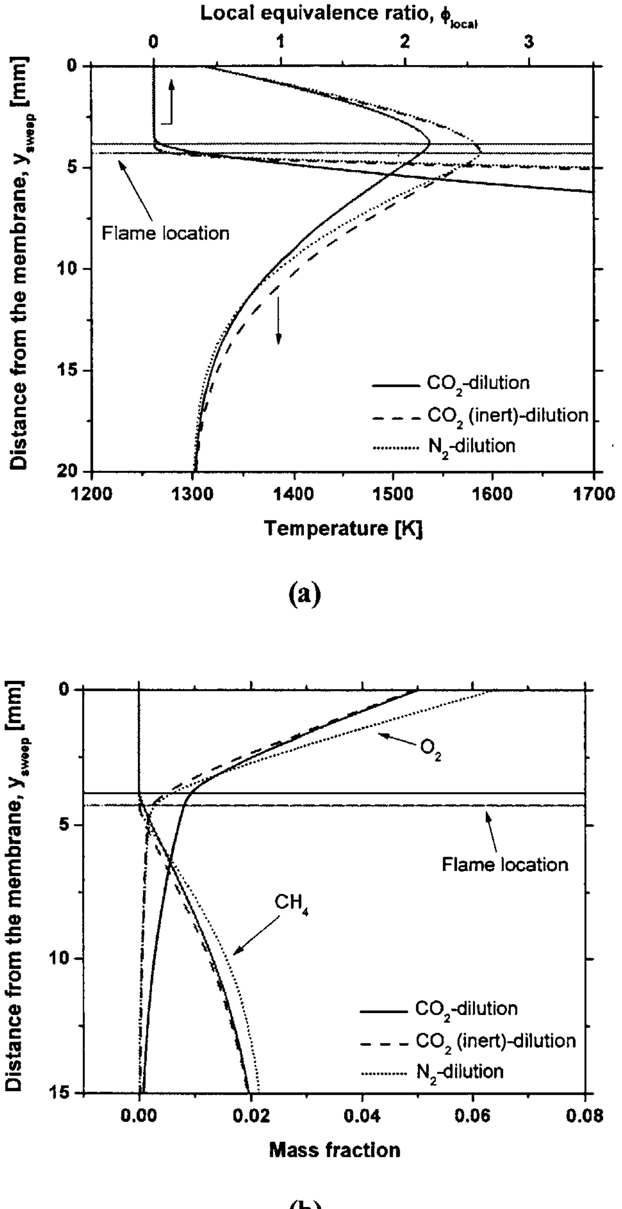

(a)

(b)

Figure 4-2 The variations of (a) temperature and the local equivalence ratio and (b) CH_4 and O_2 concentrations, along with the flame location (where, solid lines represent CO_2-dilution, dashed lines are for CO_2 (inert, eliminating the chemical effects of CO_2)-dilution, and dotted lines stand for N_2-dilution). A lower slope of the local equivalence ratio represents a wider overlap of CH_4 and O_2, and hence a thicker flame. $y_{sweep} = 0$ is located on the membrane surface of the sweep side.

Table 4-2 Important reactions considered in this investigation (obtained from the reaction pathway analysis), which determine the reaction products and govern predominantly the overall fuel conversion processes, and their enthalpy of reaction at standard temperature and pressure, ΔH_{STP}. The spatially averaged reaction rate, $\bar{\eta}_i$, represents the strength of each reaction for both CO_2-dilution and N_2-dilution cases. The CH_2 exists in two electric states, singlet and triplet, and (s) in R.2 and R.10 represents its singlet state.

Reaction Number	Reaction	ΔH_{STP} [kJ/mol]	$\bar{\eta}_i$ [mol/m³/s]		
			CO_2-dilution	N_2-dilution	CO_2-dilution/ N_2-dilution
(R.1)	$H + CO_2 \leftrightarrow OH + CO$	104.3	$0 \sim y_{flame}$: -5.76	$0 \sim y_{flame}$: -3.68	1.57
			$y_{flame} \sim H_{sweep}$: 2.31×10^{-1}	$y_{flame} \sim H_{sweep}$: -5.43×10^{-2}	4.25
(R.2)	$CH_2(s) + CO_2 \leftrightarrow CH_2O + CO$	−255.5	2.26×10^{-1}	6.08×10^{-2}	3.72
(R.3)	$H + O_2 \leftrightarrow O + OH$	70.5	1.02	1.14	0.895
(R.4)	$O + H_2 \leftrightarrow H + OH$	8.2	5.39×10^{-2}	2.13×10^{-1}	0.253
(R.5)	$H + O_2 + M \leftrightarrow HO_2 + M$	−205.5	2.85×10^{-1}	2.31×10^{-2}	1.23
(R.6)	$H + CH_4 \leftrightarrow CH_3 + H_2$	3.5	1.02×10^{-1}	3.74×10^{-1}	0.273
(R.7)	$H + H_2O \leftrightarrow OH + H_2$	63.2	$0 \sim y_{flame}$: -1.62	$0 \sim y_{flame}$: -4.74	0.342
			$y_{flame} \sim H_{sweep}$: 1.36×10^{-2}	$y_{flame} \sim H_{sweep}$: 1.71×10^{-1}	0.0795
(R.8)	$H + CH_2O \leftrightarrow HCO + H_2$	−67.4	7.57×10^{-2}	1.79×10^{-1}	0.423
(R.9)	$OH + CH_4 \leftrightarrow CH_3 + H_2O$	−59.7	5.58×10^{-1}	4.40×10^{-1}	1.27
(R.10)	$OH + CH_3 \leftrightarrow CH_2(s) + H_2O$	1.8	2.67×10^{-1}	2.06×10^{-1}	1.30
(R.11)	$OH + CH_2O \leftrightarrow HCO + H_2O$	−130.6	3.12×10^{-1}	1.63×10^{-1}	1.91
(R.12)	$2CH_3 + M \leftrightarrow C_2H_6 + M$	−377.7	5.87×10^{-2}	8.56×10^{-2}	0.686
(R.13)	$2CH_3 \leftrightarrow H + C_2H_5$	−175.1	1.85×10^{-2}	2.77×10^{-2}	0.668
(R.14)	$C_2H_6 + OH \leftrightarrow C_2H_5 + H_2O$	−78.7	3.90×10^{-2}	3.73×10^{-2}	1.05

(R.15)	$C_2H_5 + M \leftrightarrow H + C_2H_4 + M$	151.8	7.36×10^{-2}	1.11×10^{-1}	0.663
(R.16)	$C_2H_4 + M \leftrightarrow H_2 + C_2H_2 + M$	175.7	4.05×10^{-3}	4.57×10^{-3}	0.886
(R.17)	$HCO + M \leftrightarrow H + CO + M$	65.5	2.74×10^{-1}	2.51×10^{-1}	1.09
(R.18)	$OH + HO_2 \leftrightarrow O_2 + H_2O$	−293.7	4.02×10^{-1}	2.92×10^{-1}	1.38
(R.19)	$H + O_2 + H_2O \leftrightarrow HO_2 + H_2O$	−205.5	1.83×10^{-1}	2.15×10^{-1}	0.851
(R.20)	$CH_3 + O_2 \leftrightarrow OH + CH_2O$	−216.1	1.63×10^{-2}	3.56×10^{-3}	4.58

where $\dot{\eta}_i$ is the rate of reaction *i*. Note that $\overline{\dot{\eta}}_i$ of R.1 and R.7 are shown for each side, i.e., the oxidizer and fuel sides, of the flame in **Table 4-2**, because their directions change from the forward reaction on the fuel side of the flame, i.e., $\frac{1}{\left(H_{sweep} - y_{flame}\right)}\int_{y_{flame}}^{H_{sweep}} \dot{\eta}_i \, dy > 0$, to the backward reaction on the oxidizer side of the flame, i.e., $\frac{1}{y_{flame}}\int_{0}^{y_{flame}} \dot{\eta}_i \, dy < 0$, where y_{flame} is the flame location. Other reactions vary monotonically such that the forward reaction is dominant throughout the sweep gas channel. When high concentration CO_2 is introduced with a hydrocarbon fuel into a high temperature environment such as the sweep side of the ITM, the endothermic reaction of CO_2 with the H radical, R.1, forming CO is favored [85] while approaching the flame, i.e., on the fuel side of the flame. The radical H is formed through thermolysis of CH_4 prior to the flame. Compared to the N_2-dilution case, the reaction rate of R.1 and consumption of the H radical in the CO_2-dilution case is faster on the fuel side of the flame because of the high concentration CO_2, which leads to a reduction in the flame temperature. On the oxidizer side of the flame, high concentration CO_2 acts as a third body in R.5, which is a chain terminating reaction, to promote the H radical consumption and to inhibit the most important chain branching reaction, R.3. The lower flame temperature and consumption of the H radical due to R.1 and R.5 slow down R.3, which is weakly endothermic and depends strongly on temperature. R.3 is the primary reaction for consuming oxygen and producing more radicals hence enhancing the overall reaction rates. As a result, in the CO_2-dilution case, oxygen is not fully consumed in the reaction zone due to the lack of the H radical and instead leaks through the flame, as shown in **Figure 4-2**(b). The unconverted oxygen further lowers the flame temperature. The leakage of oxygen through the flame results in a lower peak flame temperature, flame instability and possible extinction in conventional diffusion flames under the impact of high strain rates [90, 91]. Moreover, since CO_2 has a higher specific heat capacity than N_2, the temperature rise due to the exothermic reactions of fuel combustion is lower. Consequently, the flame temperature is reduced in comparison with that of N_2-dilution. To differentiate the chemical effects of CO_2 from its thermal effects on the flame temperature, **Figure 4-2**(a) also shows the temperature in a case in which CO_2 was assumed to be chemically inert. Inert-CO_2 has the same thermodynamic and transport properties as CO_2, but it is chemically inactive and hence does not contribute to the chemical reactions. The flame temperature in the inert-CO_2 dilution case is similar to that of the N_2-dilution case, indicating that the chemical effects of CO_2 on a lower flame temperature are more dominant. In addition, the enhanced species diffusion in the CO_2-dilution case promotes the transport of the reaction products away from the reaction zone, leading to a smaller temperature gradient, in particular, on the fuel side of the flame. This reduces the conductive heat transfer towards the fuel stream, and hence preheating of the reactants.

The presence of high concentration CO_2 in the sweep gas stream also affects CH_4 oxidation, the flame thickness and location. **Figure 4-2**(b) shows that CH_4 conversion is delayed, and it diffuses closer to the membrane in the CO_2-dilution case. The suppression of the chain branching reactions, R.3 and R.4, and the enhancement of the chain terminating reaction, R.5, reduce the radical concentrations, as will be discussed in Section 4.3.4, and lower the overall reaction rates. The initiation of CH_4 kinetics through reaction with the H radical via R.6 is delayed by the consumption of the H radical in R.1 on the fuel side of the flame. These two effects suppress CH_4 oxidation and delay the onset of fuel conversion. Moreover, the flame stretch is smaller in the CO_2-dilution case than that with N_2 (see **Figure 4-1**). The leakage of oxygen in the CO_2-dilution case makes the reaction environment unstable and brings it closer to the extinction limit. In this case, to obtain the same Damköhler number as that of the CO_2-dilution case, the N_2-diluted fuel stream requires a higher strain rate, which needs a higher inlet velocity. Consequently, given the same Damköhler number, fuel concentration and inlet temperature, the lower reaction rates and smaller flame stretch in the CO_2-dilution case form a thicker diffusion flame, as evidenced by the smaller slope of the local equivalence ratio in **Figure 4-2**(a) (see comments on the figure). The local equivalence ratio, ϕ_{local}, is defined as,

$$\phi_{local} = \frac{\left(m_{O_2}/m_{CH_4}\right)_{stoich}}{\left(m_{O_2}/m_{CH_4}\right)} = \frac{\left(2W_{O_2}/W_{CH_4}\right)}{\left(Y_{O_2}/Y_{CH_4}\right)} \qquad \textbf{Eq. 4-4}$$

A lower slope of the local equivalence ratio represents a wider overlap of fuel and oxidizer, and hence a thicker diffusion flame. In addition, the suppression of CH_4 oxidation shifts the flame towards the membrane. **Figure 4-2** highlights the chemical effects of CO_2, showing that they result in a thicker diffusion flame and shifts the flame further towards the membrane, as seen in comparison with the inert-CO_2 dilution case.

4.3.3. Reaction products governed by suppressed H and enhanced OH radical chemistry

The dominant reactions governing the overall reaction rates are different from those of CH_4/air flames and consequently impact the products on the sweep side of the ITM. **Figure 4-3** shows the profiles of CO_2, CO, H_2 and H_2O concentrations. It can be seen that the CO concentration in the CO_2-dilution case is larger than that of the N_2-dilution case throughout the sweep gas channel. The higher CO concentration is attributed to the enhanced CO_2 reduction reactions, R.1 and R.2 in **Table 4-2**. Note that a small fraction of CO reaches the membrane surface in the CO_2-dilution case, as compared to the N_2-dilution case in which the CO concentration at the membrane surface is nearly zero. Due to its higher concentration of CO and the relative proximity of the flame location to the membrane, CO oxidation cannot be completed. On the other hand, the H_2 concentration in the CO_2-dilution case is lower, in comparison with that of the N_2-dilution case. This can be explained by the suppressed H radical reactions, R.6 to R.8 in **Table 4-2**, because of the lower H radical concentration as a result of R.1 on the fuel side of the flame. R.6, R.7 and R.8 are the primary reactions for the production of H_2, which takes place on the fuel side of the flame (see **Figure 4-4**(b)).

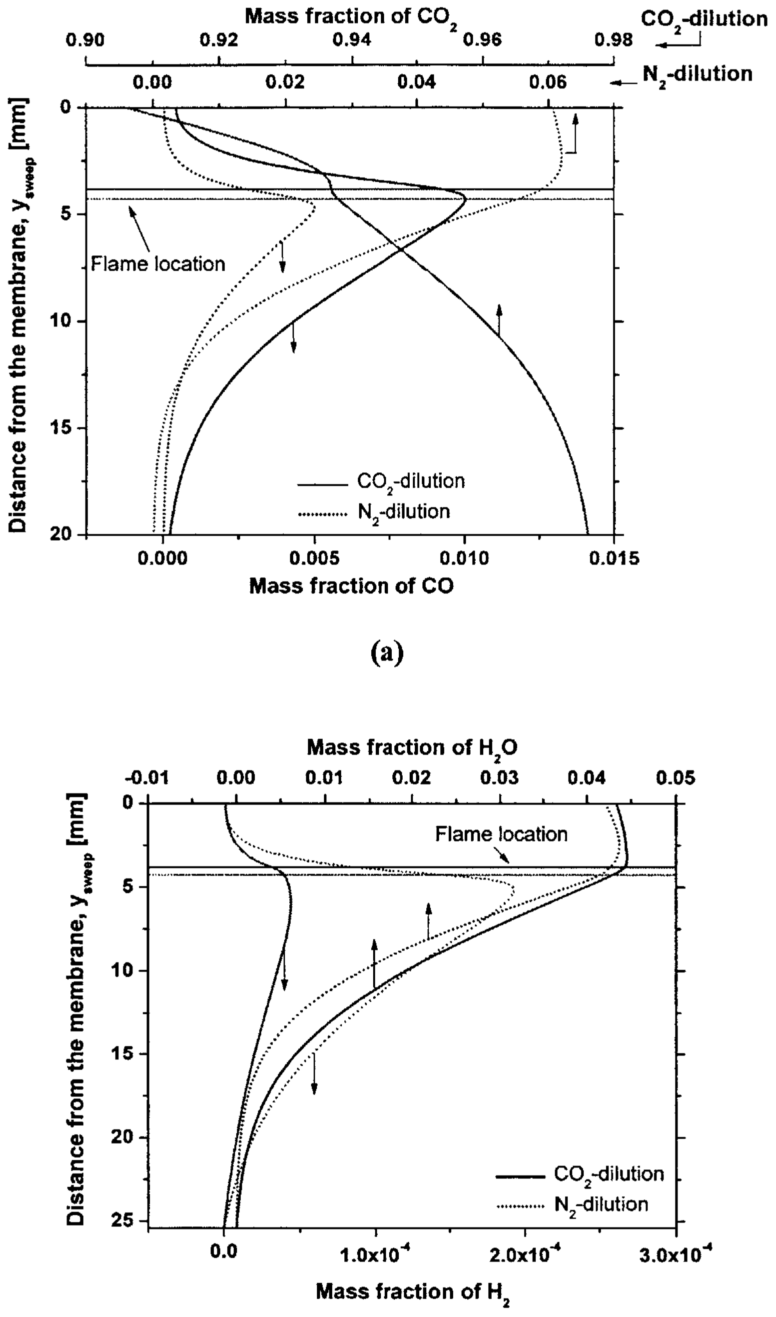

(a)

(b)

Figure 4-3 The concentrations of the reaction products (a) CO_2 and CO and (b) H_2 and H_2O, throughout the sweep gas channel, along with the flame location (where, solid lines represent CO_2-dilution, and dotted lines stand for N_2-dilution). $y_{sweep} = 0$ is located on the membrane surface of the sweep side.

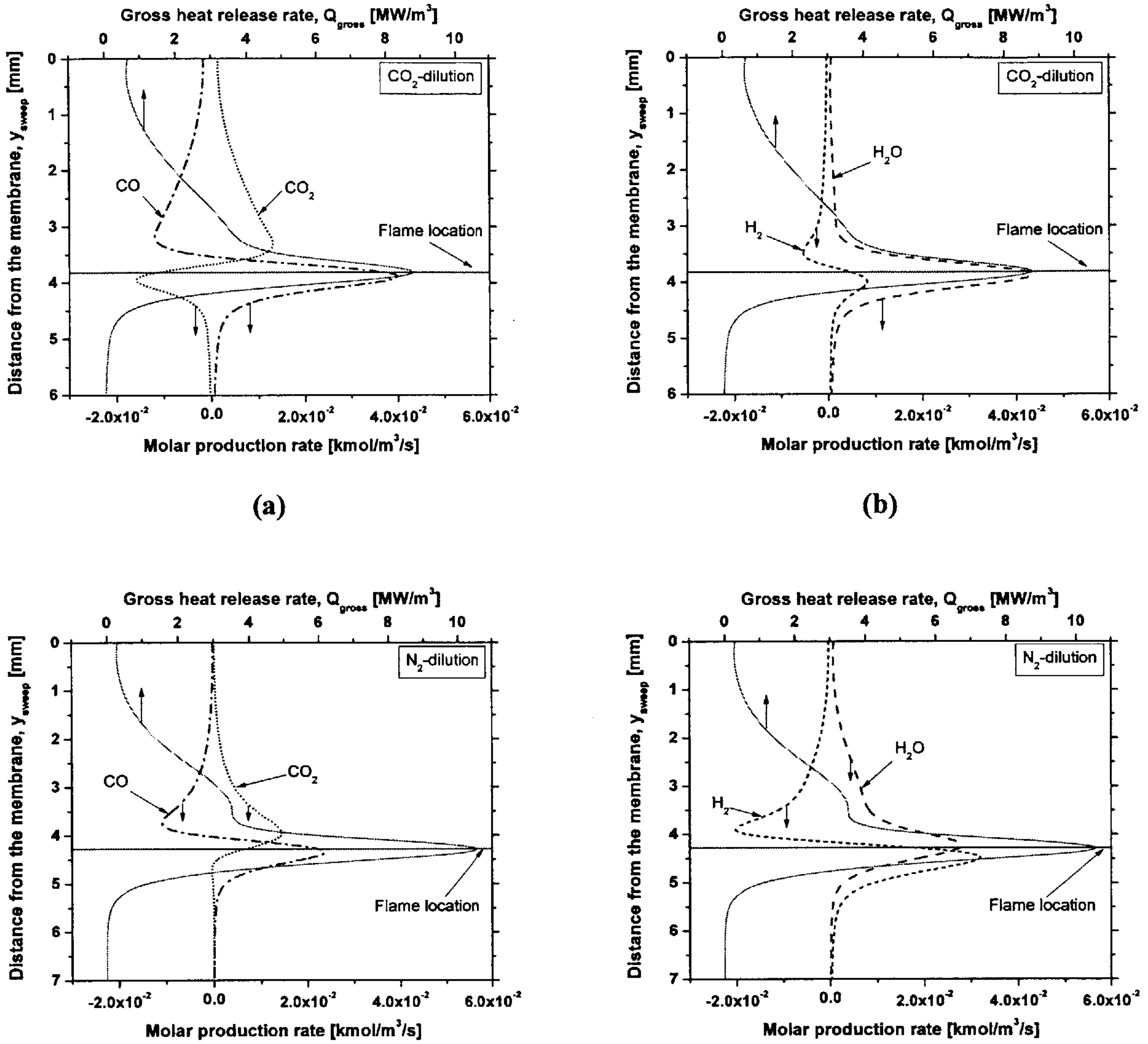

(a) (b)

(c) (d)

Figure 4-4 The molar production rates of the reaction products, CO_2, CO, H_2 and H_2O, along with the gross heat release rate and the flame location for CO_2-dilution ((a) and (b)) and N_2-dilution ((c) and (d)). $y_{sweep} = 0$ is located on the membrane surface of the sweep side.

Because the H radical is consumed by R.1, the forward rates of these three reactions are reduced, hence lowering the H_2 concentration. With respect to H_2O production, R.9, R.10 and R.11 (see

Table 3-1) are more dominant in the CO_2-dilution case. The OH radical is produced in the CO_2 reduction reaction, R.1, before reaching the flame, while the H radical is consumed. This promotes the forward reactions of R.9, R.10 and R.11, and a slightly larger H_2O concentration in CO_2-dilution. Therefore, suppressed H radical chemistry and enhanced OH-driven reactions change the products on the sweep side of the ITM and lead to higher CO and lower H_2 concentrations.

Changing the H and OH radical chemistry impacts the location of CO_2, CO, H_2 and H_2O production. **Figure 4-4** shows the molar production rate profiles of the four species along with the gross heat release rate for CO_2-dilution ((a) and (b)) and N_2-dilution ((c) and (d)) cases. In the CO_2-dilution case, CO is produced via R.1 while approaching the primary reaction zone (defined by the major peak in the heat release rate). It can be seen that CO production and CO_2 destruction proceed together, and they are accelerated in comparison with the N_2-dilution case (compare **Figure 4-4**(a) and (c)). Their production and destruction rates are maximized in the high temperature primary reaction zone driven by both R.1 and R.2. As these two reactions become dominant when the sweep gas approaches the primary reaction zone, the H_2O production rate increases significantly via R.9 to R.11, whereas H_2 production is suppressed (compare **Figure 4-4**(b) and (d)). On the other hand, in the CO_2-dilution case, CO oxidation (the backward reaction of R.1) in the secondary reaction zone (defined by the secondary peak in the heat release rate) is substantially enhanced (refer to **Figure 4-4**(a) and **Table 4-2**) due to the high CO concentration, which inhibits the H_2O production and H_2 destruction in this region (see **Figure 4-4**(b)) by competing for the OH radical with the backward reaction of R.7. As a result, suppressed H radical chemistry (R.6 to R.8) and OH-driven reactions (R.9 to R.11) on the fuel side of the flame, and enhanced CO oxidation on the oxidizer side of the flame confine species production to a small region in the high temperature primary reaction zone, relative to the N_2-dilution case. This effect will be discussed further in Section 4.3.5.

4.3.4. Low radical concentrations

Suppressed chain branching reactions due to CO_2 decomposition affect the radical concentrations. **Figure 4-5** shows the profiles of the radicals, H, O, OH and CH_3. In general, the radical concentrations in the CO_2-dilution case are significantly reduced in comparison with those of the N_2-dilution case. The small amount of hydrogen-oxygen radicals, i.e., H, O and OH, are attributed to the suppression of the chain branching reactions, R.3 and R.4, and the enhancement of the chain terminating reaction, R.5 (refer to **Table 4-2** for their reaction rates). The consumption of the H radical by the CO_2 reduction reaction, R.1, on the fuel side of the flame and the chain terminating reaction, R.5, on the oxidizer side of the flame lower the reaction rate of R.3, while the low H_2 concentration in the CO_2-dilution case slows down R.4. In addition, high concentration CO_2 promotes the chain termination via R.5. The suppression of R.3 and R.4 and the enhancement of R.5 lower the radical concentrations and reduce the overall reaction rates in the CO_2-dilution case as compared to the N_2-dilution case. In addition, the concentration of CH_3, which is a precursor for the initiation of CH_4 oxidation, is substantially lowered before reaching the primary reaction zone due to R.6. As discussed in Section 4.3.2, the reaction rate of R.6 is reduced by competing with R.1 for the H radical.

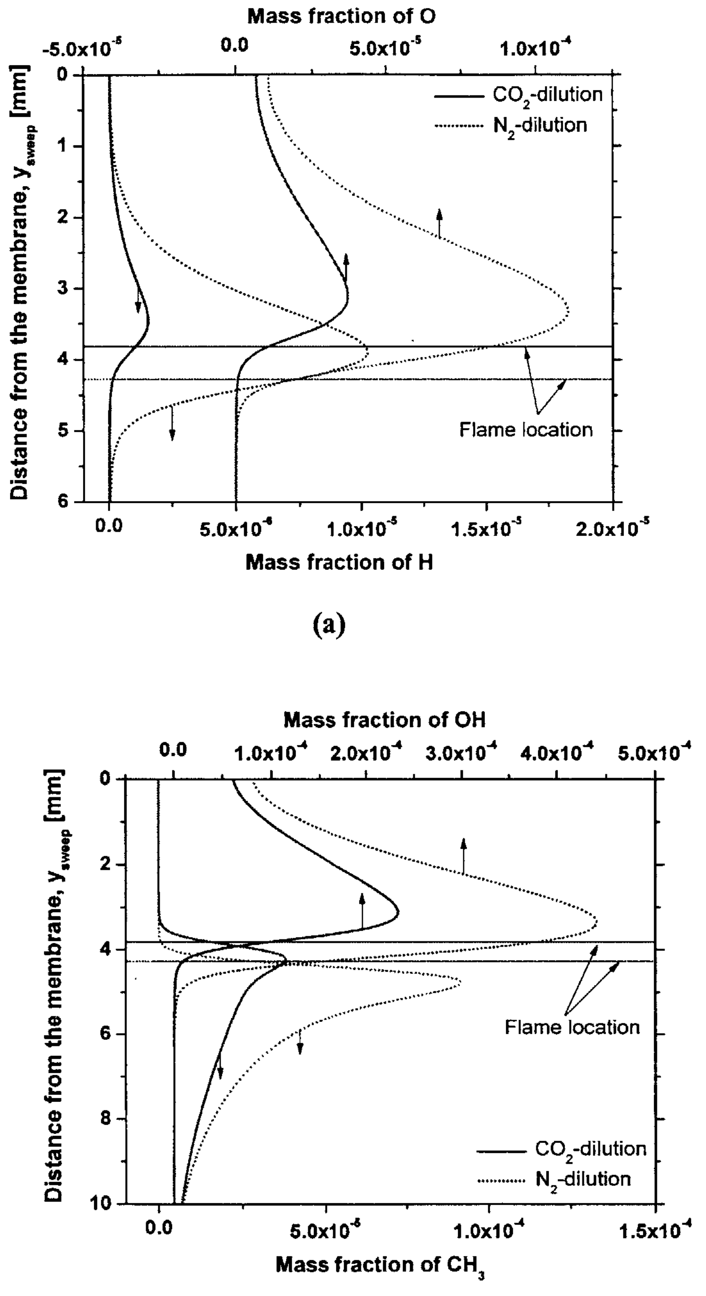

(a)

(b)

Figure 4-5 The concentrations of the important radicals (a) H and O and (b) OH and CH_3, along with the flame location (where, solid lines represent CO_2-dilution, and dotted lines stand for N_2-dilution). $y_{sweep} = 0$ is located on the membrane surface of the sweep side.

As a consequence, the CH_4 kinetics is delayed, and the CH_3 mass fraction is lowered. Therefore, the higher concentration of CO_2 on the sweep side of the ITM reduces the radical concentrations and slows the overall fuel conversion processes.

Lowering the CH_3 radical concentration also has an impact on the fuel pyrolysis. In a diffusion flame with temperature of approximately 1500 K, such as that established on the sweep side of the ITM, the CH_4 kinetics have additional pathways that lead to the formation of C_2 hydrocarbons [92]. Before reaching the flame, i.e., on the fuel side of the flame, CH_3 molecules are combined to form C_2H_6 and C_2H_5 via R.12 and R.13 (see **Table 4-2**). C_2H_6 and C_2H_5 react further via R.14, R.15 and R.16 to form C_2H_2 and C_2H_4, which are known soot precursors [93]. However, high CO_2 concentration in the sweep gas stream lowers CH_3 formation and concentration before reaching the primary reaction zone via R.1 and R.6 by reducing the H radical concentration, as shown in **Figure 4-5**. Accordingly, the reaction rates of R.12 and R.13 are reduced, and the formation of soot precursors, C_2H_2 and C_2H_4, are suppressed, as shown in **Figure 4-6**. Note that, because CO_2 is mixed and fed into a reaction zone with the fuel stream, i.e., fuel dilution, the formation of soot precursors is reduced, as discussed in [94, 95]. In conventional diffusion flames in which oxidizer dilution via N_2 is typically used, such a reduction in the formation of soot precursors does not take place. Thus, the presence of high concentration CO_2 in the sweep gas (fuel) stream may suppress hydrocarbon pyrolysis and the formation of soot precursors. This conclusion needs further investigations by implementing a more comprehensive soot chemistry.

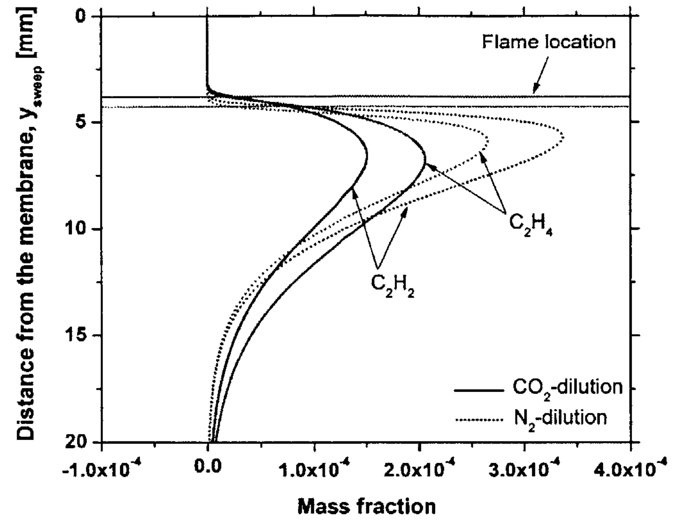

Figure 4-6 Soot precursors, C_2H_2 and C_2H_4, concentrations, along with the flame location (where, solid lines represent CO_2-dilution, and dotted lines stand for N_2-dilution). $y_{sweep} = 0$ is located on the membrane surface of the sweep side.

4.3.5. Reaction pathway and flame structure

A reaction pathway analysis shows that the dominant reactions governing the overall fuel conversion processes and the flame structure on the sweep side of the ITM are also impacted by CO_2 dilution. **Figure 4-7** shows the reaction rate of the important reactions, which determine the reaction products and govern predominantly the overall fuel conversion, and the gross heat release rate for CO_2-dilution ((a) and (b)) and N_2-dilution ((c) and (d)) cases. **Figure 4-7**(a) and (c) show the primary reaction zone where CH_4 conversion forming CO takes place, while the secondary reaction zone in which CO oxidation and H_2/O_2 reactions occur is shown in **Figure 4-7**(b) and (d). In the CO_2-dilution case, the major peak in the heat release rate is attributed to R.2, R.9, R.10, R.11 and R.17, while the secondary peak in the heat release rate is contributed by R.1, R.5, R.7, R.18 and R.19, most of which are not prominent in the N_2-dilution case (see **Table 4-2** for reactions and their relative reaction rates).

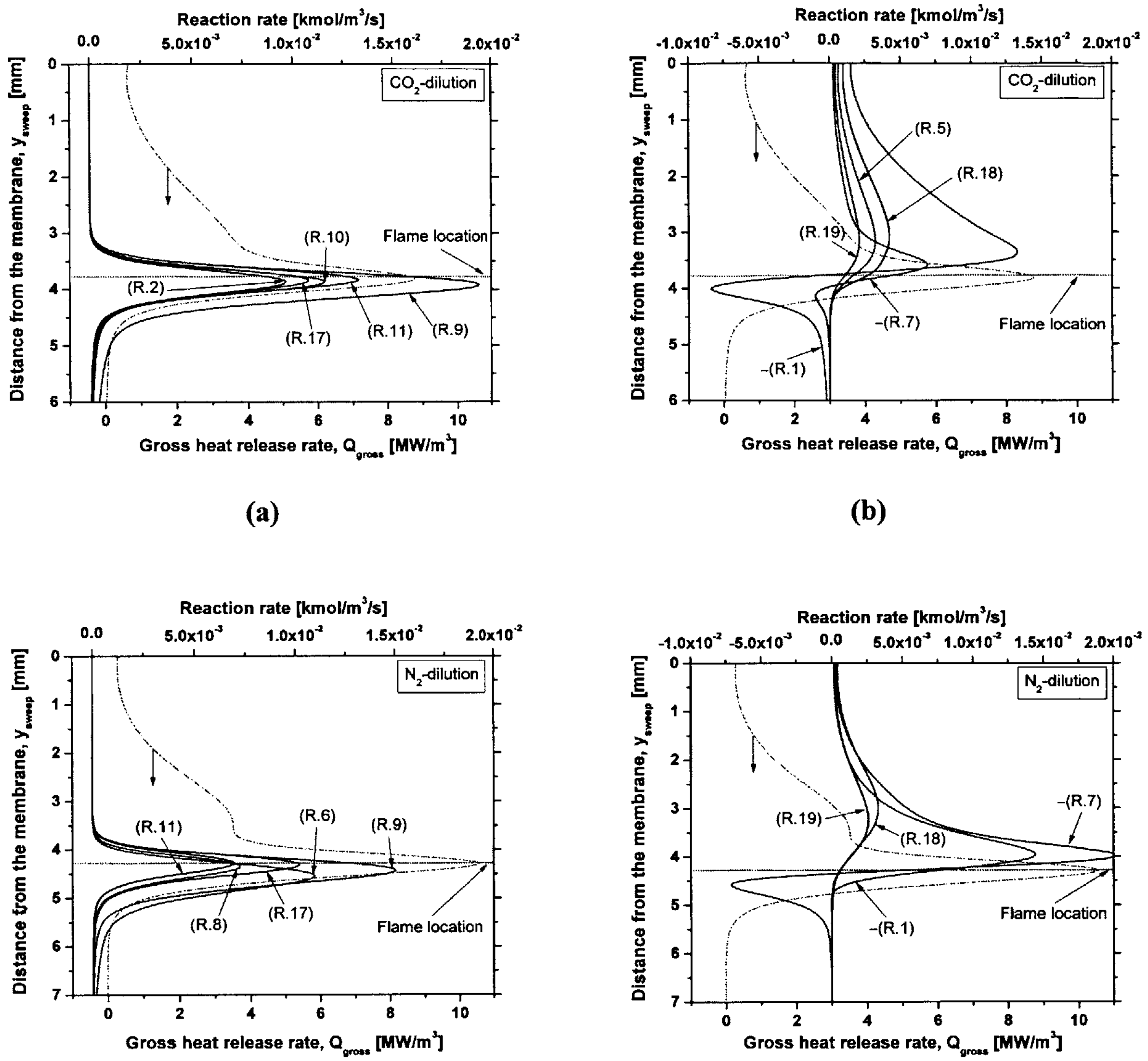

(a) (b)

(c) (d)

Figure 4-7 Gross heat release rate, the flame location and the reaction rate of dominant reactions for the primary reaction zone where CH_4 is converted to CO ((a) and (c)) and the secondary reaction zone in which CO oxidation and H_2/O_2 reactions take place ((b) and (d)). The minus sign in front of a reaction number means by its reverse direction. (a) and (b) belongs to CO_2-dilution, while (c) and (d) are for N_2-dilution. $y_{sweep} = 0$ is located on the membrane surface of the sweep side.

Note that CO and CO_2 in the secondary reaction zone are important third bodies, *M*, in R.5 and R.17 promoting their forward reaction rates. We also note that CO oxidation, which is the reverse of R.1, is dominant in the secondary reaction zone and is not completed by the time it reaches the membrane, while the reverse of R.7 is suppressed. As a result, the concentration of CO can be non-zero at the membrane surface, and the H_2O production is limited to the primary reaction zone. It can be observed that the dominant reactions in the CO_2-dilution case coincide with the major peak in the heat release rate, as discussed in Section 4.3.3, in comparison with the N_2-dilution case where its dominant reactions, R.6, R.8, R.9, R.11 and R.17 (see **Table 4-2** for reaction numbers), are spatially more distributed across the primary reaction zone. Thus, the flame structure in the CO_2-dilution case is governed by CO_2 reactions and OH-driven chemistry. The results from the reaction pathway analysis are depicted in **Figure 4-8**, showing the importance of the reaction pathways for CO_2 dilution relative to N_2 dilution. This shows the important carbon-containing species and dominant reactions that govern the overall fuel conversion processes in ITM reactors (CO_2-dilution). The thickness of the arrows represents the ratio of the reaction rates between the CO_2-dilution case and the reference case (N_2-dilution), i.e., thick-solid arrows mean that the corresponding reactions are enhanced, whereas thin-dashed arrows show suppressed reactions in CO_2-dilution in comparison with N_2-dilution. In the N_2-dilution case where both H and OH radical reactions are relevant, the dominant reactions follow the characteristics of typical counter-flow diffusion flames as discussed in [81].

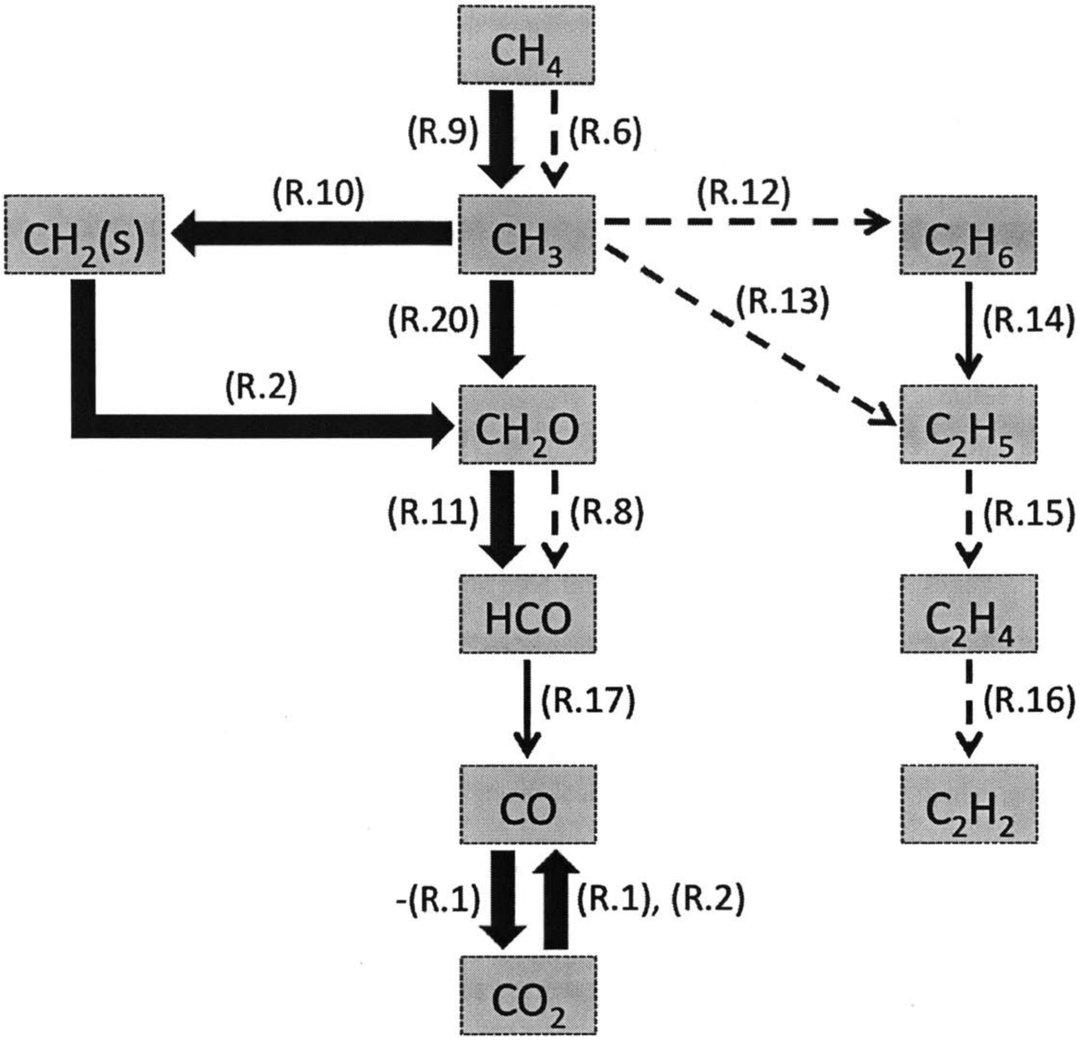

Figure 4-8 Reaction pathway analysis showing the important carbon-containing species and dominant reactions in ITM supported fuel conversion processes (CO_2-dilution). The thickness of arrows represents the ratio of the reaction rates between the CO_2-dilution case and the reference case (N_2-dilution), which is summarized in Table 3 (i.e., thick solid arrows = enhanced reactions in CO_2-dilution, thin solid arrows = moderate reactions in CO_2-dilution, thin dashed arrows = suppressed reactions in CO_2-dilution).

4.4. Conclusions

The numerical model is used to examine fuel conversion processes and associated important phenomena, which includes the location, temperature, thickness and structure of a flame, the relationship between the oxygen permeation rate and the oxidation reactions, hydrocarbon pyrolysis and the formation of possible soot precursors, occurring on the sweep side of the ITM. The presence of an ITM that permeates oxygen into the sweep side supports oxy-fuel combustion with high fuel dilution with CO_2. Since the oxygen permeation rate is typically low compared to the convective oxidizer flow in conventional counter-flow diffusion flames, the flow rate and fuel concentration of the sweep gas stream are limited to meet the requisite stoichiometry. In addition, to achieve a sufficient oxygen permeation flux and enhance the chemical kinetics, the sweep gas, i.e., the fuel feed stream, is preheated, leading to a relatively high temperature pre-flame environment. The oxygen permeation rate is not known a priori and is dependent on the local flow conditions, i.e., the species concentration and temperature near the membrane, which are affected by the chemical reactions in the vicinity of the membrane. As a result, under the conditions modeled in this study, the sweep side of the ITM features a preheated laminar oxy-fuel diffusion flame composed of a CO_2-diluted fuel stream and an oxidizer, the flow rate of which is coupled with the fuel conversion characteristics such as reaction zone position, flame temperature and diluent composition.

Fuel conversion processes on the sweep side of the ITM show the interesting features of a laminar oxy-fuel diffusion flame. The chemical effects of a high CO_2 concentration in the sweep gas stream result in a lower flame temperature and the suppression of the CH_4 kinetics, relative to the case with the N_2-diluted sweep gas. The endothermic reduction reaction of CO_2 and the chain terminating reaction promoted by CO_2 compete with the chain branching reaction for the H radical and leads to a reduction in the flame temperature, low radical concentrations and oxygen leakage through the flame. The leakage of unconverted oxygen through the flame further lowers the flame temperature. Moreover, the initiation of CH_4 oxidation is delayed due to the reduction of the H radical chemistry, and hence a thicker flame is established near the membrane surface. The location of the flame determines the flame temperature and the oxygen permeation rate via species diffusion and heat transfer from the flame towards the membrane. CO_2 decomposition consumes the H radical while producing the OH radical. As a result, H radical chemistry is suppressed, whereas OH-driven reactions are enhanced. This produces more CO and H_2O and less H_2. Fuel dilution with CO_2 also reduces CH_3 formation, which slows down fuel pyrolysis and may reduce soot formation. In addition, CO_2 and OH driven reactions govern the flame structure to confine species production to a small region in the high temperature primary reaction zone. The flame location close to the membrane implies that surface reactions may play important roles in fuel conversion processes. This along with gas radiation effects will be investigated in a subsequent study.

Page left intentionally blank

Chapter 5 Sensitivity Analysis of Operating Conditions

5.1. Overview

When a reactive gas is added to the sweep stream of an ITM reactor, the oxygen permeation rate and the hydrocarbon conversion are influenced by the local thermodynamic state (predominantly the oxygen concentration and the gas temperature near the membrane surface). Because oxygen is introduced through permeation, the fuel and oxidizer in the sweep side of an ITM are not pre-mixed, leading to the establishment of a non-premixed or diffusion-controlled reaction zone. In such diffusion-supported reactions, the local thermodynamic state including species concentration and temperature play significant roles in establishing stable reactions and determining the reaction products. Unlike typical diffusion-controlled combustion in which the temperature is so high that the overall hydrocarbon conversion rate is governed almost solely by diffusion, the temperature in an ITM reactor is kept low to protect the membrane, and hence chemical kinetics play an important role in determining the fuel conversion rate. Furthermore, the initial conditions of the oxidizer and the fuel streams (i.e., permeated oxygen and sweep gas in the case of ITM reactors, respectively) govern the hydrocarbon conversion. However, unlike other conventional reactors, the flow rate and temperature of the oxidizer stream (i.e., oxygen permeation) in an ITM reactor are not known a priori and rather depend on the oxygen partial pressure in the immediate vicinity of the membrane and its temperature. Therefore, it is difficult to independently control the mass ratio of the fuel to the oxidizer in the sweep side and hence hydrocarbon conversion processes. The detailed analysis using a spatially resolved physical model is needed to examine the key features that can be observed in the vicinity of the membrane, which has been neglected in the literature.

In this chapter, the interactions between oxygen permeation and fuel conversion on the sweep side of an ITM are investigated. It is assumed that no additional catalyst is mounted on the membrane, and the membrane surface is not catalytically active for hydrocarbon or syngas conversion. To elucidate the relationship between fuel conversion and oxygen permeation, a parametric study is performed with respect to several control parameters including the fuel concentration in the sweep gas stream (i.e., fuel plus a diluent), its inlet temperature, flow rate and the channel height (i.e., the distance from the membrane to the sweep gas inlet or the opposite walls).

5.2. Parametric study

To examine the interactions between fuel conversion and oxygen permeation, a parametric study is conducted with respect to several control parameters including the fuel concentration in the sweep gas stream on a molar basis, $x_{CH_4,sweep}$, the sweep gas inlet temperature, T_{sweep}, volumetric flow rate, F_{sweep}, and the channel height, H_{sweep}. The parameters and their variations considered in the parametric study are summarized in **Table 5-1**. The interaction between the permeated oxygen and the fuel forms a laminar, non-premixed (diffusion), oxy-fuel reaction zone. The oxygen permeation rate is substantially lower than the flow rate of a convective oxidizer feed stream in conventional counter-flow diffusion flames [68, 87], and hence the fuel stream (i.e., sweep gas) has to be fed into the sweep side at a low velocity in order to maintain an overall stoichiometric mixture.

Table 5-1 The control parameters or independent variables and their variations considered in the parametric study

Control parameter (independent variable)		Unit	Base-case value	Range of variations	
				Min	Max
Fuel concentration in the sweep gas (with the remainder being CO_2)	$x_{CH_4,sweep}$	[%]	6	3	30
Sweep gas inlet temperature	T_{sweep}	[K]	1300	1050	1400
Sweep gas flow rate	F_{sweep}	[m^3/s]	4.39×10^{-4}	3.00×10^{-4}	4.50×10^{-3}
Sweep gas channel height	H_{sweep}	[mm]	25.4	3.00	30.0

Moreover, the fuel stream is heavily diluted with CO_2 to keep the reaction zone temperature low [7] in order to protect the membrane material, and hence the fuel oxidation kinetic rates are not as fast as in the case of conventional diffusion flames. To meet this requirement, the base-case considers a sweep gas volumetric flow rate of 4.39×10^{-4} m^3/s (sweep gas velocity at the inlet = 7.56×10^{-2} m/s, $Re_{sweep} = 15.6$) and a fuel concentration of 6%, with the remainder being CO_2 at a temperature of $T_{sweep} = 1300K$. Note that, integrated at the front end of a power plant, an ITM reactor may use a hot recycled carbon dioxide stream as a diluent in the sweep gas stream. The base-case considers a membrane thickness, L, of 100 μm and the sweep gas channel height of 25.4 mm. Throughout the parametric study, the air inlet flow rate of 1.97×10^{-3} m^3/s (air velocity at the inlet = 3.70×10^{-1} m/s, $Re_{air} = 100$) and temperature of 1300 K, are maintained constant. It is assumed that the surrounding wall temperature is the same as the gas (i.e., both air and sweep gas) inlet temperature. The total pressure is kept constant at 1 atm. These control parameters for the base-case are selected as they are representative of realistic operating conditions for ITM reactors.

5.2.1. Base-case results and important features

The base-case results highlight the characteristics of the diffusion-controlled reaction zone and the important features regarding fuel conversion and oxygen permeation. **Figure 5-1**(a) shows the variations of the CH_4 and O_2 molar concentrations, the temperature and the heat release rate between the membrane and the sweep gas inlet. The concentrations of CH_4 and O_2 decrease from the sweep gas inlet and the membrane surface, respectively, approaching the reaction zone in which the maximum temperature and the peak heat release rate are found. The chemical reactions, i.e., CH_4 conversion and O_2 consumption, around the reaction zone lower their concentrations while raising the heat release rate and the temperature. A rise in temperature exists even in regions without a significant heat release due to the heat transfer and the transport of the hot products towards both the membrane surface and the sweep gas inlet. A sharp temperature gradient near the membrane indicates a high heat transfer rate towards the membrane of 8.58 kW/m^2, being a significant fraction of the gross heat release of 12.1 kW/m^2. This raises the membrane temperature while lowering the reaction zone temperature. The membrane conducts part of this heat (4.33 kW/m^2) to the air side and transfers the rest of it (4.25 kW/m^2) to the sweep side surrounding walls via radiation. On the air side, the conducted heat is transferred to the air (0.08 kW/m^2) and towards the air side surrounding walls via radiation (4.25 kW/m^2). Note that the radiative heat transfer plays an important role in controlling the membrane temperature and maintaining a high reactor temperature. In addition, the thermal energy carried by the permeated oxygen (1.15 kW/m^2) is transferred from the air to the sweep gas through the membrane. The gross heat release, Q_{gen}, is defined as follows,

$$Q_{gen} = \int_0^{H_{sweep}} q\,dy_{sweep} = \int_0^{H_{sweep}} \left(\sum_1^N \dot{\omega}_k \hat{h}_k \right) dy_{sweep} \quad \textbf{Eq. 5-1}$$

where q is the heat release rate; N is the number of gas-phase species; $\dot{\omega}_k$ is the molar production rate of species *k*; $\hat{h}_k$ is the molar enthalpy of species *k*. The gross heat release shows the extent of the chemical reactions and their effect on the temperature rise, whereas the heat transfer to the membrane indicates a thermal effect on the temperature drop.

The transport of the products away from the reaction zone is also important for determining the temperature as well as the local species concentration. The major products from fuel conversion processes include CO_2, CO, H_2 and H_2O, and their concentrations indeed show large increase around the reaction zone (i.e., production) and continuous reductions away from it (i.e., transport), as shown in **Figure 5-1**(b). Note that the CO_2 concentration drops as the fuel stream reaches the reaction zone increasing that of CO, due to decomposition or reverse water gas-shift reactions, which suppresses the production of H_2 [96]. The reduction in the CO_2 concentration is also attributed to the transport of O_2 and H_2O towards the sweep gas inlet. After being produced through the chemical reactions, the primary products diffuse out from the reaction zone towards the membrane surface and the sweep gas inlet.

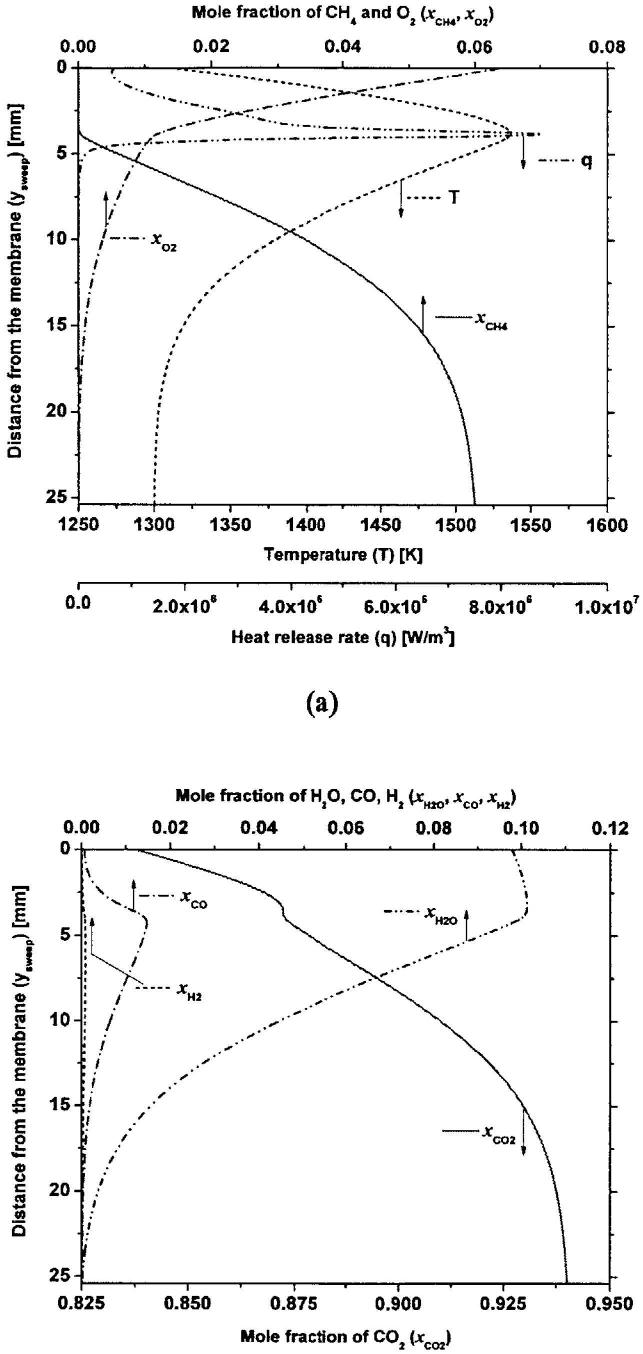

(a)

(b)

Figure 5-1 Base-case results: (a) the profiles of the temperature, the heat release rate, the CH_4 and O_2 mole fractions; (b) the concentrations of the products including CO_2, CO, H_2O and H_2, along the direction normal to the membrane

Thus, in such diffusion-controlled reactions, both species production and their transport are important for determining the local thermodynamic state including species concentration and temperature. In particular, when comparing the molar concentration of the products and oxygen at the membrane surface in **Figure 5-1**(a) and (b), it can be seen that the transport of the products towards the membrane surface reduces the oxygen concentration and raises the gas temperature near the membrane. Since the reaction zone, the location of which, relative to the membrane, is represented by the location (i.e., reaction front, y_{front}) of the maximum heat release rate, is established near the membrane surface, the effect of species transport towards the membrane is substantial, resulting in a low oxygen partial pressure in the immediate vicinity of the membrane, $P_{O_2,mem}$, and a high membrane temperature, T_{mem}. As a result, the transport of the products and heat towards the membrane along with oxygen consumption through the chemical reactions enhances the oxygen permeation rate, J_{O_2}, to 3.53 μmol/cm^2/s, in comparison with the case of an inert sweep gas which achieves the oxygen permeation rate less than or nearly 1.00 μmol/cm^2/s. The transport of the reaction products towards the membrane is also important in influencing the kinetic rates on the oxidizer side of a diffusion-controlled reaction zone. The product concentrations on the oxidizer side of a reaction zone can change substantially the O_2 consumption and radical reaction rates, i.e., chain-branching and chain-terminating reactions. Moreover, depending on the membrane, the composition of the mixture at the membrane surface can have significant implications on the membrane longevity [30, 97, 98].

Fuel conversion processes in an ITM reactor can be characterized by key variables such as the CH_4 conversion, the gross heat release, the residence time and the average scaled transverse (i.e., parallel to the membrane) velocity. The CH_4 conversion, X_{CH_4}, is defined as,

$$X_{CH_4} = \frac{V_{CH_4,converted} A_{mem}}{F_{sweep} x_{CH_4,sweep} \varsigma_{sweep}} = \frac{A_{mem} \int_0^{H_{sweep}} -\dot{\omega}_{CH_4}\, dy_{sweep}}{F_{sweep} x_{CH_4,sweep} \varsigma_{sweep}} \qquad \textbf{Eq. 5-2}$$

where $V_{CH_4,converted}$ is the conversion rate of CH_4 on the sweep side; ς_{sweep} is the molar density of the sweep gas; A_{mem} is the membrane area. The CH_4 conversion indicates how much fuel is consumed relative to the amount of fuel in the sweep gas stream, representing the effectiveness of fuel conversion processes on the sweep side. The base-case result shows a CH_4 conversion of 39.4%. The rest of the fuel cannot be converted through the chemical reactions and rather flows out from the reaction zone following the transverse velocity, whose magnitude is represented by the average scaled transverse velocity, U_{avg}:

$$U_{avg} = \frac{1}{H_{sweep}} \int_0^{H_{sweep}} U\, dy_{sweep} \qquad \textbf{Eq. 5-3}$$

where U is the scaled transverse velocity. Given the normal velocities of the oxidizer (i.e., oxygen permeation at the membrane surface) and the fuel (i.e., sweep gas at the inlet) streams and the sweep gas channel height, the flow field within the sweep side is determined and hence the transverse velocity. In addition, the normal velocities of both streams determine the available time or the residence time for the chemical reactions. The residence time, t_{res}, is defined as,

$$t_{res} = \frac{H_{sweep}}{\left(v_{O_2} + v_{sweep}\right)} \qquad \textbf{Eq. 5-4}$$

where υ_{O_2} is the velocity associated with the oxygen permeation rate; υ_{sweep} is the sweep gas velocity at the sweep gas inlet. Under diffusion-controlled conditions, the fuel oxidation kinetics governs the CH_4 conversion based on such variables as the flow field as well as the local thermodynamic state and the initial conditions of the oxidizer and the fuel streams.

Important features found in the base-case results show that it is worthwhile to investigate the relationship between fuel conversion and oxygen permeation by varying flow conditions on the sweep side. In diffusion-controlled reactions, the local thermodynamic state has a large impact on the fuel oxidation kinetics and hence the CH_4 conversion. Furthermore, oxygen consumption via the chemical reactions, the species transport and heat transfer towards the membrane play significant roles in determining the gas temperature and the oxygen concentration in the vicinity of the membrane, affecting the oxygen permeation rate. For these reasons, a parametric study is conducted with respect to the control parameters that change flow conditions on the sweep side, including the fuel concentration in the sweep gas, its inlet temperature, flow rate and the channel height.

5.2.2. Effect of fuel concentration

In an ITM reactor used for oxy-fuel combustion or fuel reforming, the fuel is diluted in CO_2. Here, we investigate the impact of the fuel concentration in the CO_2 sweep stream on fuel conversion and oxygen permeation. In the parametric study, the fuel concentration is raised from 3% to 30%, while the sweep gas inlet temperature, flow rate and channel height are maintained at their base-case values. **Figure 5-2** shows that, up to $x_{CH_4,sweep} \approx 15\%$, increasing the fuel concentration enhances the oxygen permeation rate substantially, while the CH_4 conversion is gradually lowered.

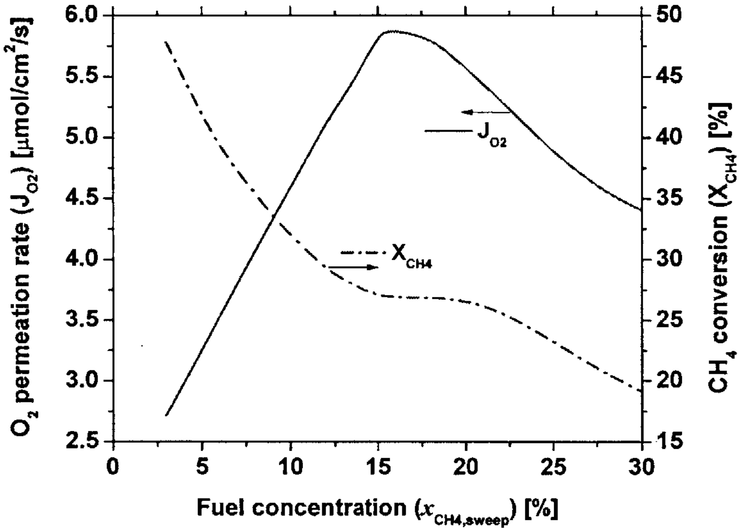

Figure 5-2 The dependency of the oxygen permeation rate and the CH_4 conversion on the fuel concentration

Beyond this point, as the fuel concentration is raised further, the oxygen permeation rate starts decreasing. As the oxygen permeation rate approaches a peak, the CH_4 conversion does not change significantly, but decreases extensively again, as the oxygen permeation rate decreases with further increases in fuel concentration. To examine why these two regimes (i.e., the enhancement and reduction of the oxygen permeation rate) exist, variables changing largely with the fuel concentration and affecting the oxygen permeation rate and the CH_4 conversion need to be investigated.

Oxygen consumption, the generation and transport of the products, in particular, the primary products such as H_2O, near the membrane and the heat transfer towards it play significant roles in determining the oxygen permeation rate through the oxygen partial pressure near the membrane and its temperature. In addition, the reaction zone is shifted towards the membrane with increasing CH_4 concentration, which further lowers the CH_4 conversion. **Figure 5-3**(a) shows the enhancement of the oxygen consumption rate, ϖ_{O_2}, and the gross heat release with the fuel concentration. In addition, as the fuel concentration is raised, the reaction zone is shifted towards the membrane, while the molar flow rate ratio of the oxygen permeation rate to the fuel influx, $J_{O_2} / J_{CH_4,in}$, gradually decreases. Higher reactant concentrations in the reaction zone promote the fuel oxidation kinetics in the gas-phase, consuming more oxygen, and result in substantial fuel conversion, although the membrane is not catalytically active. Furthermore, since the increase in oxygen permeation is not sufficient to match that of the fuel supply, raising the fuel concentration moves the reaction zone towards the oxidizer stream inlet, i.e., the membrane surface. As such, more fuel is convected out following the transverse velocity prior to the reaction zone, hence reducing the CH_4 conversion. On the other hand, when the reaction zone is shifted towards the membrane along with the higher oxidation kinetic rates, more products such as H_2O are produced and transported towards the membrane, increasing the product concentration at the membrane surface while decreasing that of O_2, as shown in **Figure 5-3**(b). In the meantime, the heat transfer increases significantly driven by a larger gross heat release and the reaction zone established closer to the membrane, which leads to a higher membrane temperature. Therefore, the enhancement of oxygen consumption, species production and transport near the membrane and the heat transfer lowers the oxygen partial pressure in the immediate vicinity of the membrane and increases its temperature, hence enhancing the oxygen permeation rate.

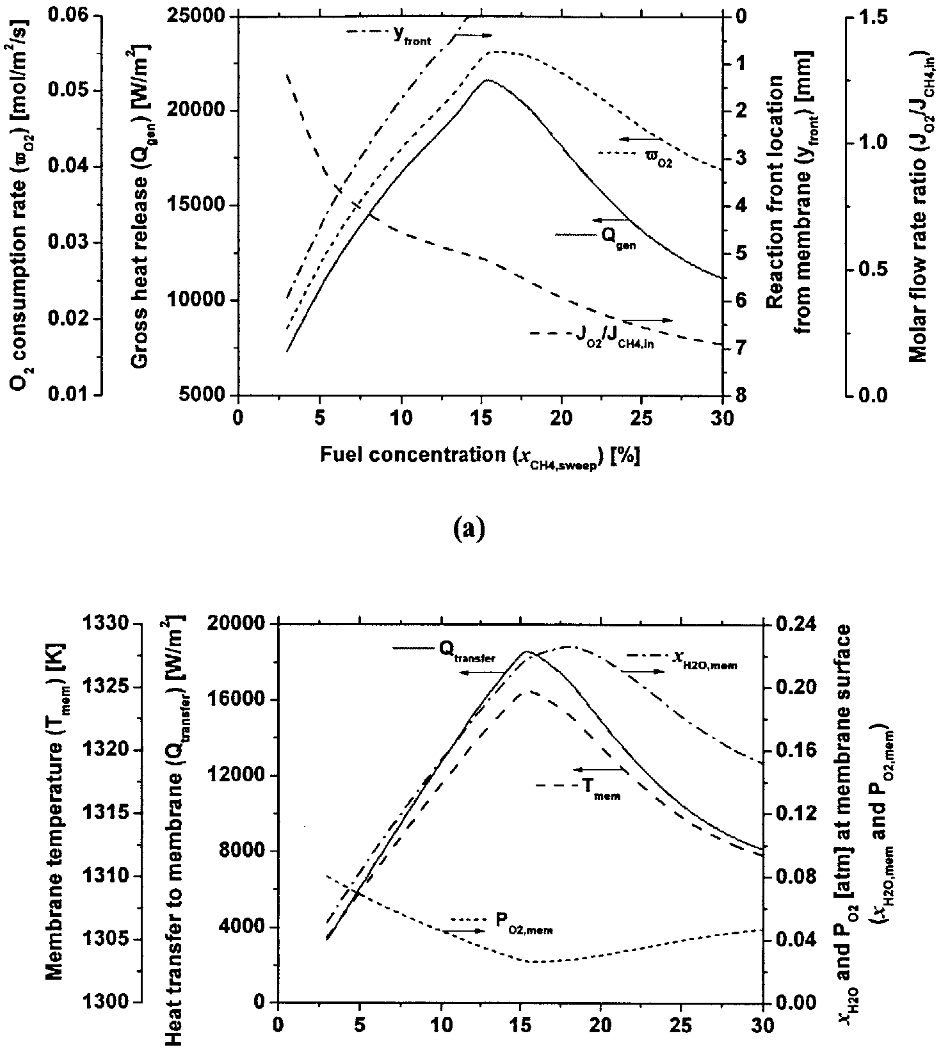

(a)

(b)

Figure 5-3 The variations of: (a) the oxygen consumption rate, the gross heat release from the chemical reactions, the reaction zone location relative to the membrane and the molar flow rate ratio of the oxygen permeation rate to the fuel influx; (b) the heat transfer towards the membrane, the membrane temperature and the concentrations of H_2O and O_2 at the membrane surface, with respect to the change in the fuel concentration

However, these variations change their trends as the reaction zone reaches the membrane. Once this occurs, subsequent increases in the fuel concentration result in decreases in the oxygen permeation rate.

The heat transfer towards the membrane impacts the reaction zone temperature and the fuel oxidation kinetics, and causes the reaction zone remaining near the membrane surface. The maximum gas temperature, $T_{\max}$, represents the reaction zone temperature. **Figure 5-4**(a) shows that the reaction zone temperature initially increases with the fuel concentration. However, as the fuel concentration is raised, the reaction zone temperature reaches a peak at the same fuel concentration at which the net heat release (gross heat release minus heat transfer) is at a maximum. It should be noted that this occurs at a lower fuel concentration than the maximum gross heat release. In addition, the concentrations of the reactants such as CH_4, CO and H_2 at the membrane surface rise slowly, when the reaction zone temperature decreases substantially with a further increase of the fuel concentration. When the gross heat release increases with the fuel concentration, the heat transfer also increases resulting in the reduction of the net thermal energy released, $Q_{gen} - Q_{transfer}$, which contributes to the variation of the reaction zone temperature. When the reaction zone is established close to the membrane, heat transfer to the air side and reactor walls increases, and extensive heat loss lowers the reaction zone temperature significantly. This slows down the fuel oxidation kinetics, and eventually leads to the reaction zone remaining near the membrane surface [88, 89]. **Figure 5-4**(b) shows the heat release rate profiles at different fuel concentrations, showing that the reaction zone reaches the membrane, and the maximum heat release rate reduces at high fuel concentration. As a result of extensive heat loss and the reaction front remaining at the membrane surface, when the fuel concentration is further increased, partial oxidation of methane, CO_2 decomposition reactions or the reverse water gas-shift reactions and hydrocarbon pyrolysis prevail, and the extent of the chemical reactions is reduced, while the reactants that are not fully oxidized reach the membrane surface.

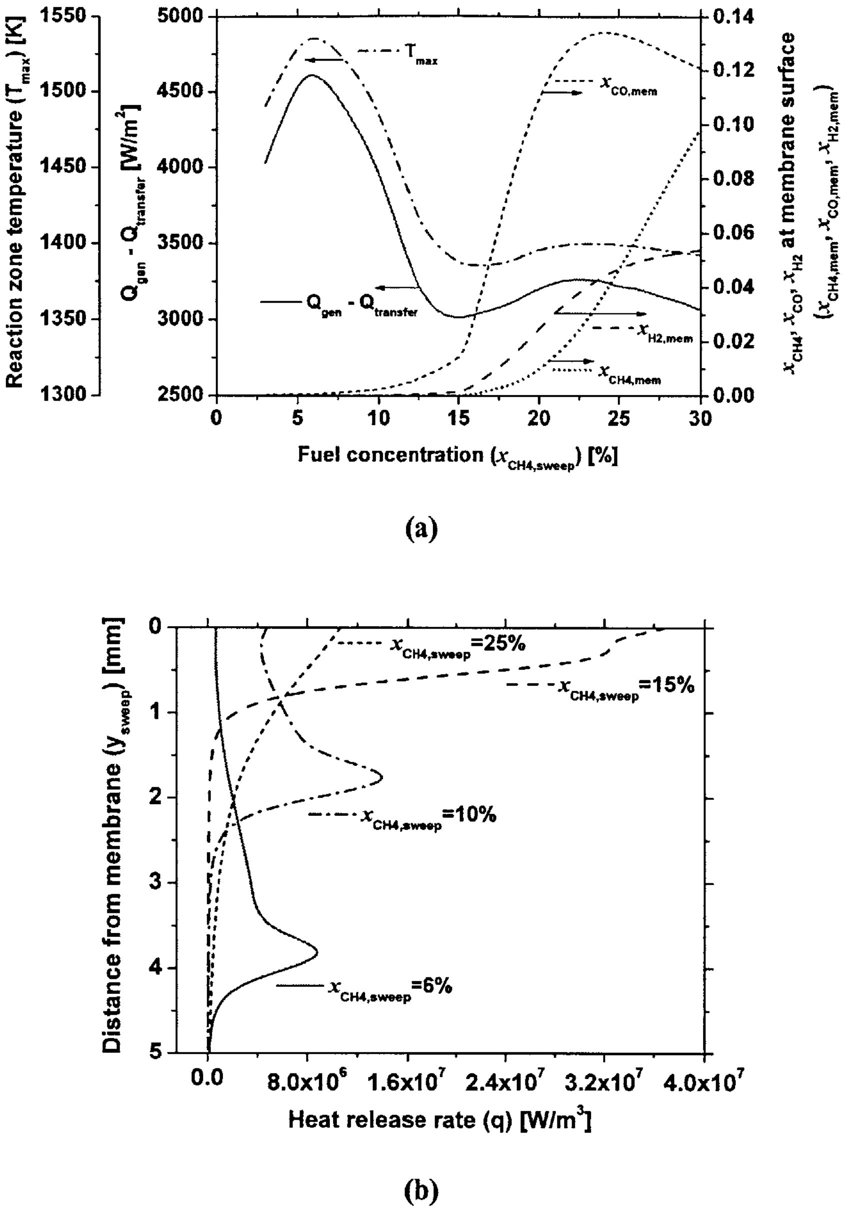

Figure 5-4 (a) The variations of the reaction zone temperature, the gross heat release subtracted by the heat transfer towards the membrane and the concentrations of CH_4, CO, H_2 at the membrane surface, with respect to the change in the fuel concentration; (b) the profiles of the heat release rate at different fuel concentrations

Therefore, at high fuel concentration, the oxygen permeation rate is reduced due to the lower kinetic rate of oxygen consumption and associated increase in local oxygen concentration and the reduced generation and transport of the products near the membrane and the heat transfer, all due to the reaction zone being located at the membrane surface. The rise in the reactant concentrations at the membrane surface implies that heterogeneous chemistry may play a role at high fuel concentration if the catalytic activity of the membrane is significant or if it has additional catalysts on its surface.

The heat loss to the air side and the surrounding walls via radiation from the membrane limits the rise of the membrane temperature and its effect on oxygen permeation. As shown in **Figure 5-3**(b), the variation of the membrane temperature is much smaller than that of the reaction zone temperature (see **Figure 5-4**(a)). Although a substantial amount of thermal energy is transferred to the membrane from the sweep side due to the chemical reactions, as the reaction zone is shifted towards the membrane, the rise of the membrane temperature is insignificant. This is attributed to the extensive heat loss to the air side and the surrounding walls via surface radiation. Note that the membrane sees large surrounding walls whose temperatures are maintained at the gas inlet temperature, as shown in **Figure 2-1**. Since the membrane temperature is nearly constant, its effect on oxygen permeation is limited, and the oxygen permeation rate is mostly dependent on the oxygen partial pressure. As seen in **Figure 5-2** and **Figure 5-3**(b), the oxygen permeation rate increases nearly three-fold, as the oxygen concentration near the membrane surface is significantly reduced for increasing fuel concentrations (given that the reaction zone is not at the membrane surface). At a high membrane temperature, oxygen permeation is largely governed by the species concentration in the vicinity of the membrane. Akin and Lin also pointed out that the oxygen permeation rate in the case of ITM reactors is highly sensitive to the variation in the oxygen partial pressure on the sweep side [56]. Thus, the species concentration near the membrane surface and the location of the reaction zone relative to the membrane play important roles in controlling oxygen permeation.

5.2.3. Effect of sweep gas inlet temperature

The sweep gas inlet temperature is another important parameter that is expected to impact oxygen permeation and fuel conversion. To examine its effect, the sweep gas inlet temperature is varied from 1050 K to 1400 K while maintaining the fuel concentration, the sweep gas flow rate and channel height at their base-case values. The air inlet and reactor wall temperature are also changed to the same value. As discussed in Chapter 3, the oxygen permeation rate varies significantly depending on the membrane temperature, and a higher sweep gas inlet temperature raises the membrane temperature, enhancing oxygen permeation. **Figure 5-5** shows that, as the sweep gas inlet temperature is increased, the oxygen permeation rate first grows slowly and then experiences a sudden and significant increase around $T_{sweep} \approx 1200K$ at which the CH_4 conversion also rises substantially. Beyond this point, as the sweep gas inlet temperature is raised further, the growth rate of the oxygen permeation rate is lowered, while the CH_4 conversion keeps increasing extensively. To investigate why these sudden and substantial increases of the oxygen permeation rate and the CH_4 conversion occur and their growth rates change, variables that depend on the sweep gas inlet temperature and impact oxygen permeation and fuel conversion are examined.

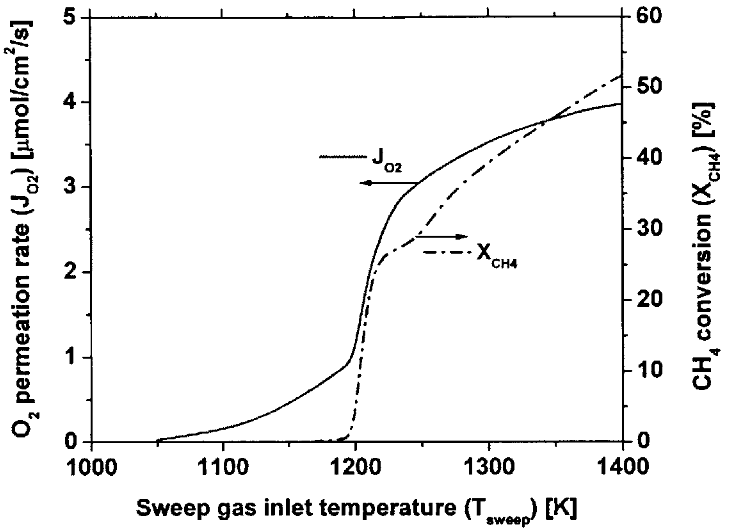

Figure 5-5 The dependency of the oxygen permeation rate and the CH$_4$ conversion on the sweep gas inlet temperature

The onset of homogeneous fuel oxidation reactions contributes to the consumption of the permeated oxygen, the generation and transport of species near the membrane and fuel conversion, while reforming reactions and partial oxidation of methane play important roles with an increase of the sweep gas inlet temperature. **Figure 5-6**(a) shows that the gross heat release and the oxygen consumption rate rise substantially around $T_{sweep} \approx 1200K$, which coincides with the increase of the oxygen permeation rate and the CH$_4$ conversion, as the sweep gas inlet temperature is raised. This phenomenon can be explained by the initiation of the CH$_4$ oxidation kinetics. When the gas temperature is not high enough to facilitate methane oxidation, only the decomposition of CH$_4$ and CO$_2$ occurs, which does not significantly affect the oxygen concentration or temperature and, as such, does not impact the oxygen permeation. To obtain the considerable gas-phase fuel conversion and oxygen permeation from the ITM reactor, the sweep gas inlet temperature has to be high enough, i.e., above an ignition temperature at the given reactant concentration, to facilitate the CH_4 oxidation reactions. Note that the typical operating temperature or membrane temperature of ITM reactors are high enough to permeate substantial oxygen to the sweep side in order to enable fuel conversion processes [61]. As a result, in the case of ITM reactors operating at high temperature, fuel oxidation reactions in the gas-phase can contribute substantially to the enhancement of oxygen permeation and fuel conversion. The sweep gas inlet temperature influences oxygen permeation not only by changing the membrane temperature, but also promoting fuel oxidation kinetics. However, as the sweep gas inlet temperature is raised further (after the initiation of homogeneous fuel oxidation reactions), the CH_4 conversion increases continuously, although the growth rate of the oxygen permeation rate decreases. This phenomenon is attributed to reforming reactions and the partial oxidation of methane. A high temperature environment facilitates the endothermic reforming reactions to increase H_2 and CO concentrations in the products. In addition, the limited oxygen concentration on the sweep side, which is lower than what is needed at higher kinetic rates (driven by high gas temperature), promotes the partial oxidation of methane. Therefore, as the sweep gas inlet temperature increases (beyond the ignition temperature), reforming reactions and the partial oxidation of methane become important to raise the CH_4 conversion.

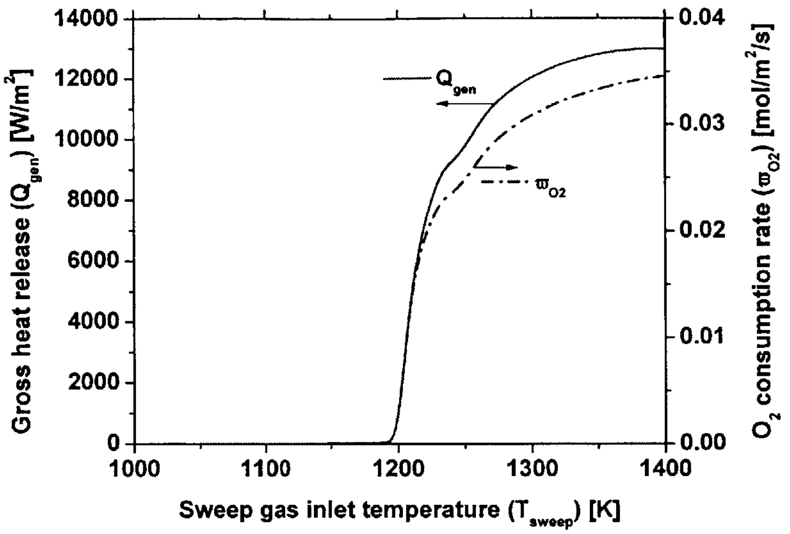

(a)

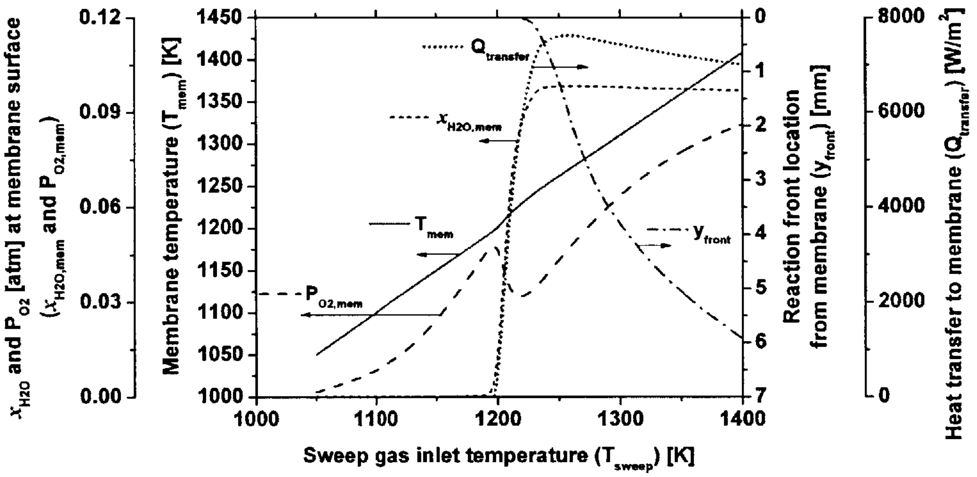

(b)

Figure 5-6 The variations of: (a) the gross heat release from the chemical reactions and the oxygen consumption rate; (b) the membrane temperature, the concentrations of H_2O and O_2 at the membrane surface, the reaction zone location relative to the membrane and the heat transfer towards the membrane, with respect to the change in the sweep gas inlet temperature

The reaction zone shifts away from the membrane with an increase of the oxygen permeation rate, reducing the effect of mass and heat transfer on oxygen permeation. When the temperature is significantly high and fuel oxidation occurs, a significant H_2O concentration at the membrane surface and the heat transfer towards it are obtained, lowering the oxygen partial pressure and raising the membrane temperature, which confirms the effect of the CH_4 oxidation and the mass and heat transfer on oxygen permeation, as shown in **Figure 5-6**(b). However, as the sweep gas inlet temperature is raised further, the H_2O concentration near the membrane and the heat transfer decrease slowly, although the oxidation reactions are further promoted, as the reaction zone is pushed away from the membrane due to a higher oxygen permeation rate. Consequently, the oxygen concentration at the membrane surface grows gradually, driven by a higher oxygen permeation rate. The heat and mass transfer towards the membrane is reduced when the reaction zone is established further from the membrane, which weakens their effect to lower the O_2 concentration in the vicinity of the membrane and to raise its temperature. Because of the reduced mass transfer, the accumulation of the permeated oxygen on the sweep side reduces the growth rate of oxygen permeation, as the sweep gas inlet temperature is raised further after the onset of homogeneous fuel oxidation reactions. Therefore, oxygen permeation is governed not only by oxygen consumption, but also by the heat and mass transfer.

5.2.4. Effect of sweep gas flow rate

I now examine the influence of another sweep gas inlet condition, the sweep gas volumetric flow rate, which determines the effect of fuel stream velocity on fuel conversion and oxygen permeation. The change in the sweep gas flow rate influences the flow field and hence the mass transfer. To highlight the mass transfer effect, the sweep gas flow rate is varied from 3.00×10^{-4} m^3/s to 4.50×10^{-3} m^3/s while maintaining the fuel concentration in the sweep gas stream, its inlet temperature and the channel height at their base-case values. **Figure 5-7** shows that, as the sweep gas flow rate is raised, the CH_4 conversion gradually decreases, whereas the oxygen permeation rate increases, before showing sudden and substantial reductions around $F_{sweep} \approx 2.30 \times 10^{-4}\, m^3/s$. Beyond this point, the oxygen permeation rate is raised again with an increase of the sweep gas flow rate, while the CH_4 conversion remains negligible. Given the fuel concentration and temperature, the homogeneous fuel oxidation reactions can proceed and contribute to fuel conversion and oxygen permeation up to a certain flow rate. Beyond this flow rate, oxygen permeation is governed by a non-reacting flow. To verify the reason for these variations and the extinction of fuel conversion processes in the gas-phase, variables that have impacts on the oxygen permeation rate and the CH_4 conversion when the sweep gas flow rate is raised are examined.

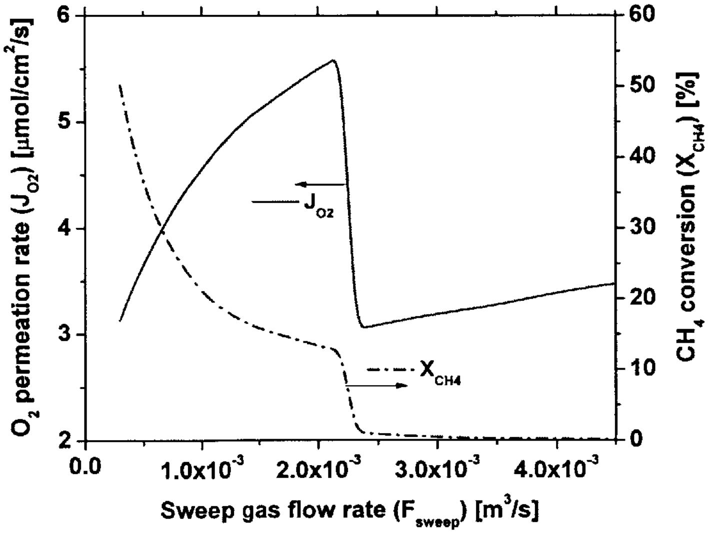

Figure 5-7 The change in the oxygen permeation rate and the CH_4 conversion, when the sweep gas flow rate is raised

The enhanced species transport establishes the reaction zone closer to the membrane and contributes to an increase of the oxygen permeation rate, whereas a higher transverse velocity and the reaction zone shifted towards the membrane make more fuel to flow out from the reaction zone before reaching it, which reduces CH_4 conversion. **Figure 5-8**(a) shows that the reaction zone is gradually shifted towards the membrane, and the CO_2 concentration in the immediate vicinity of the membrane rises, leading to the reduction of the oxygen partial pressure near it to a similar degree, with an increase of the sweep gas flow rate. The H_2O concentration at the membrane surface remains constant and then decreases to a smaller value, at the sweep gas flow rate of approximately $2.30 \times 10^{-4} \, m^3/s$, coinciding with the significant reductions of both the oxygen permeation rate and the CH_4 conversion. A higher sweep gas flow rate enhances the convective transport of the species towards the membrane and results in the reaction zone being established closer to it. In this case, more species such as CO_2 are transferred towards the membrane surface, which lowers the concentration of O_2 in the vicinity of the membrane, hence increasing the oxygen permeation rate.

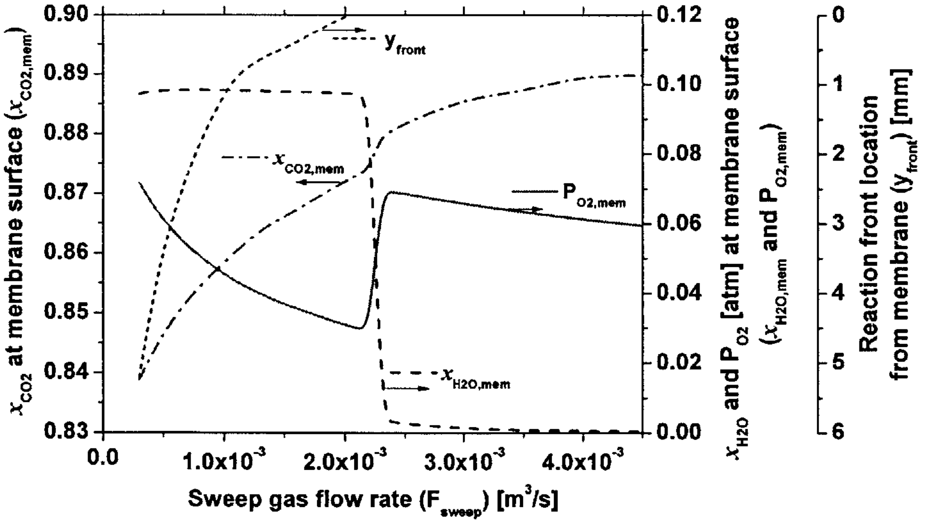

(a)

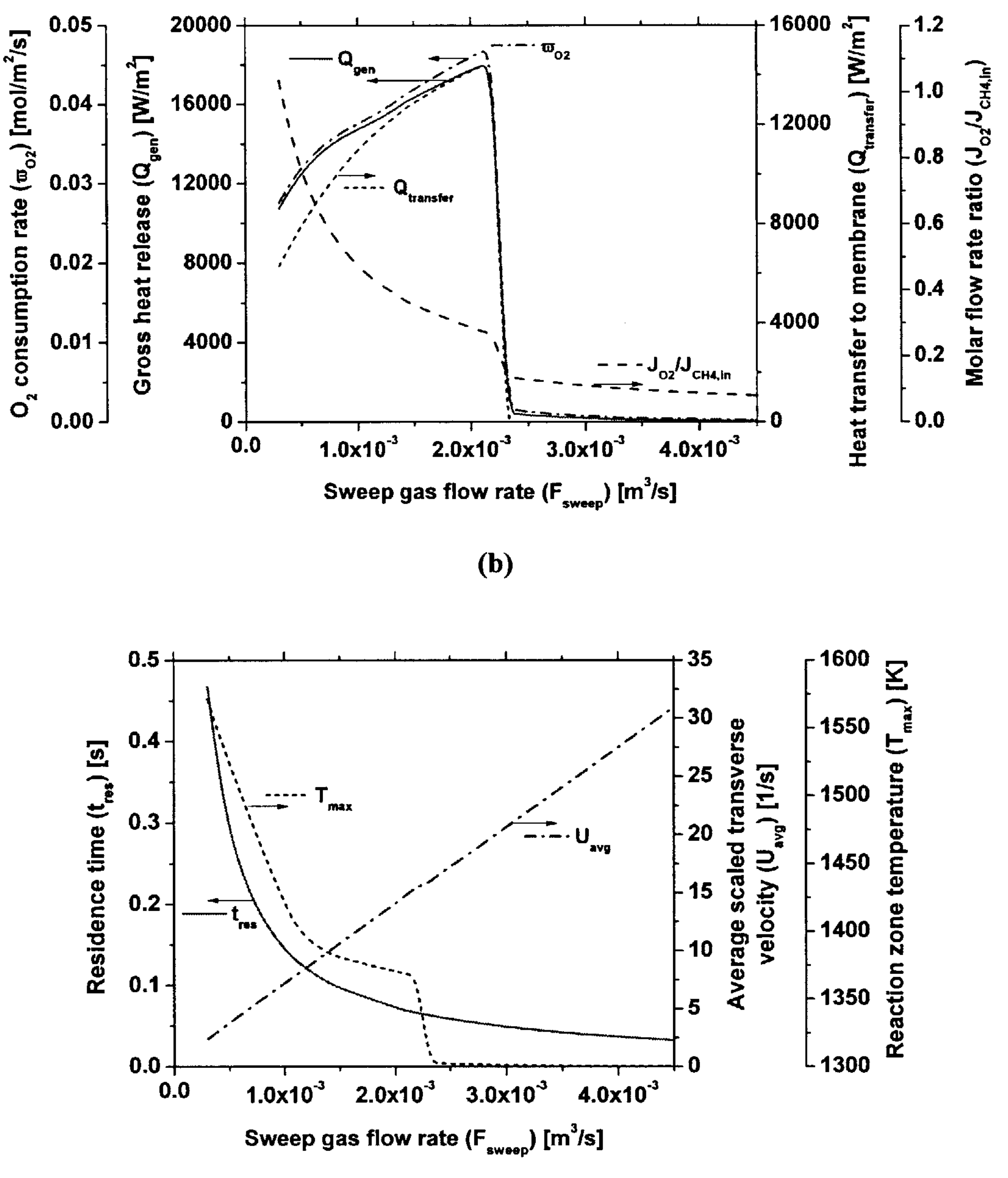

(b)

(c)

Figure 5-8 The variations of: (a) the concentrations of CO_2, H_2O and O_2 at the membrane surface and the reaction zone location relative to the membrane; (b) the gross heat release from the chemical reactions, the oxygen consumption rate, the heat transfer towards the membrane and the molar flow rate ratio of the oxygen permeation rate to the fuel influx; (c) the residence time, the reaction zone temperature and the average scaled transverse velocity, with respect to the change in the sweep gas flow rate

However, the concentration of H_2O at the membrane surface does not change even with the movement of the reaction zone towards the membrane and a larger oxygen permeation rate, which promotes the formation of the products. This is attributed to the limited enhancement of homogeneous fuel oxidation reactions, as evidenced by the small rise of the gross heat release and the O_2 consumption rate shown in **Figure 5-8**(b), and the low fuel concentration. In the meantime, the heat transfer towards the membrane increases more substantially, driven by the displacement of the reaction zone, as the sweep gas flow rate is raised. Aided by the rise of the permeated oxygen, the fuel oxidation reactions are promoted, forming more products and consuming oxygen, which also contributes to an increase of the oxygen permeation rate. However, despite the rise of the oxygen permeation rate, the growth of the gross heat release is not significant. In addition, the low CH_4 concentration leads to a small increase in the H_2O concentration, and the overall reactions are predominantly governed by the CO/CO_2 reactions due to a high CO_2 concentration on the sweep side. Thus, the limited enhancement of the fuel oxidation reactions in the gas-phase and the low fuel concentration increase the formation of the reaction products slowly, as compared to the faster transport of CO_2, the net effect of which is that the H_2O concentration at the membrane surface is approximately constant. Furthermore, a higher transverse velocity (as evidenced by **Figure 5-8**(c)) and the reaction zone shifted towards the membrane have more fuel flow away from the reaction zone in the transverse direction before reaching it. The slowly promoted oxidation reactions, a gradual reduction in the molar flow rate ratio of the permeated oxygen to the fuel influx and the movement of the reaction zone towards the membrane contribute to a continuous reduction in CH_4 conversion before the extinction of the fuel oxidation reactions.

The limited enhancement of the chemical reactions and their extinction are attributed to the higher heat capacity of the sweep gas due to the higher flow rate, as well as to the extensive heat loss towards the membrane, the smaller residence time and the flow field with a higher transverse velocity. **Figure 5-8**(c) shows that, as the sweep gas flow rate is increased, the residence time and the reaction zone temperature are gradually reduced, while the average scaled transverse velocity increases significantly. Since the velocity associated with oxygen permeation is approximately three orders of magnitude smaller than the sweep gas velocity at the inlet due to the low oxygen permeation rate, the residence time is predominantly governed by the sweep gas velocity, i.e., the sweep gas flow rate. Given the sweep gas channel height, a higher sweep gas velocity results in a smaller residence time (see Eq. 5-4) and a flow field that is more stretched in the direction parallel to the membrane gaining a higher transverse velocity. In this case, as Akin and Lin [56] and Rui et al. [57] pointed out in their study, the shorter residence time results in lower fuel conversion. Given the reaction time scale, determined by the oxidation kinetics, which depends on the species concentration and temperature, the shorter residence time results in lower fuel conversion. A substantial fraction of the fuel is not converted and instead flows out from the reaction zone. Both the chemical time scale, determined by the oxidation kinetics, and the residence time play an important role in determining the extent of fuel conversion. In addition, the convective heat transfer away from the reaction zone is enhanced, and the heat capacity of the sweep gas is raised due to a higher sweep gas flow rate, as is the convective heat transfer to the membrane, all of which reduce the temperature rise driven by the reaction exothermicity, even if the gross heat release is increased. Note that the extinction of the homogeneous oxidation reactions coincides nearly with the flow rate at which the reaction zone reaches the membrane (compare **Figure 5-8**(a) and (b)), which highlights the significant effect of the heat transfer towards the membrane on fuel conversion processes. As a result, the oxidation kinetic rates are substantially lowered. If the sweep gas velocity is too high such that the residence time is not sufficient for the reactants to be converted following the oxidation pathway, the homogeneous fuel oxidation reactions cannot proceed. As a result of this mass and heat transfer effect, the chemical reactions in the gas-phase are extinguished with an increase of the sweep gas flow rate, and their positive effect on oxygen permeation and fuel conversion vanishes.

5.2.5. Effect of sweep gas channel height

It has been shown above that the location of the reaction zone relative to the membrane and the flow field play important roles in determining the oxygen permeation rate and the CH_4 conversion. Now I investigate another way to manipulate them. The flow field and reaction zone position can be manipulated without changing the sweep flow rate or fuel concentration, both of which have significant impacts on the kinetics of fuel conversion, by varying the sweep gas channel height. In the following, the sweep gas channel height is varied from 3 mm to 30 mm while maintaining the fuel concentration in the sweep gas stream, the inlet temperature and flow rate at their base-case values. **Figure 5-9** shows that, as the sweep gas channel height is reduced, the oxygen permeation rate and the CH_4 conversion first increase and then show substantial reductions around $H_{sweep} \approx 7.5mm$.

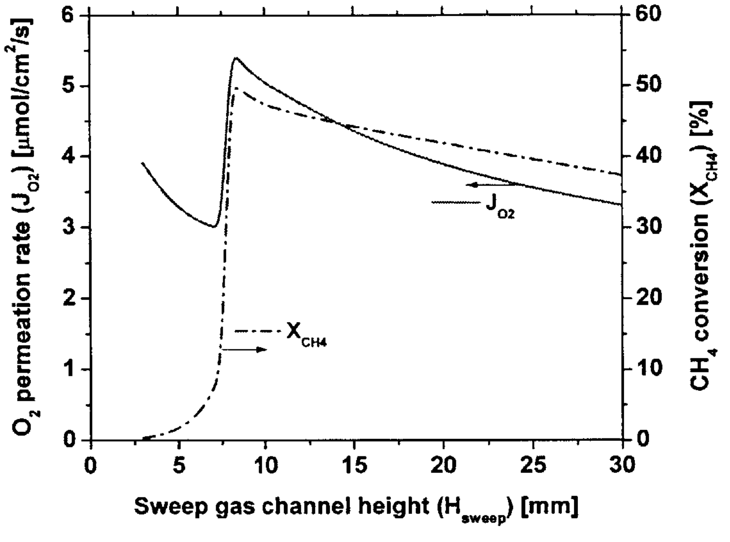

Figure 5-9 The dependency of the oxygen permeation rate and the CH_4 conversion on the sweep gas channel height

When the sweep gas channel height is reduced further beyond this point, the oxygen permeation rate rises again, whereas the CH_4 conversion is lowered continuously to zero. Note that the growth rate of the CH_4 conversion is smaller than that of the oxygen permeation rate when both of them rise before the significant decrease. Given the sweep gas initial conditions, the fuel oxidation reactions in the gas-phase can proceed and contribute to fuel conversion and oxygen permeation only above a certain channel height. Below this channel height, oxygen permeation is governed by a non-reacting flow. To examine what results in these variations and their different growth rates, variables that are mostly dependent on the sweep gas channel height and influence the oxygen permeation rate and the CH_4 conversion need to be examined.

The rise of the oxygen permeation rate is attributed to the enhanced mass transfer, driven by the reaction zone established closer to it, as well as a higher transverse velocity. **Figure 5-10**(a) shows that, as the sweep gas channel becomes narrower, the reaction zone is shifted towards the membrane, and the oxygen partial pressure in the immediate vicinity of the membrane first reduces and then grows significantly around $H_{sweep} \approx 7.5mm$ at which the oxygen permeation rate suddenly drops, while the CO2 concentration at the membrane surface changes to a similar degree.

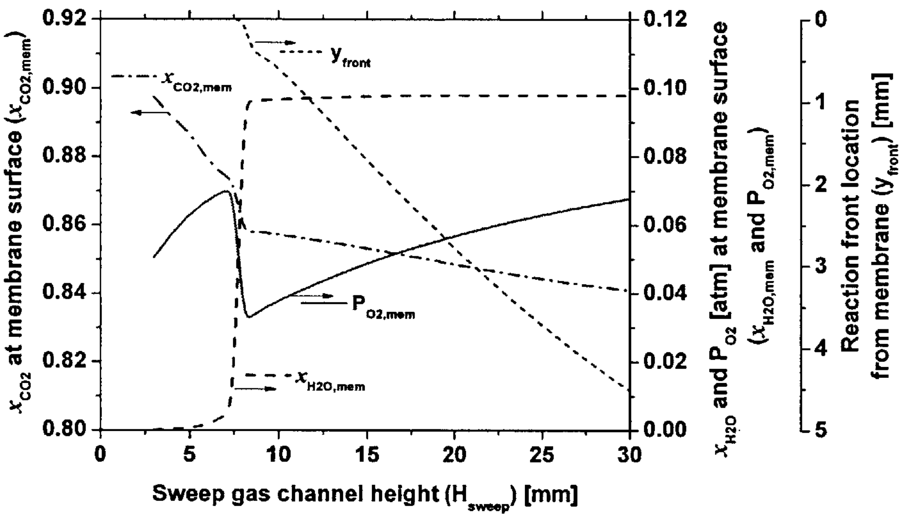

(a)

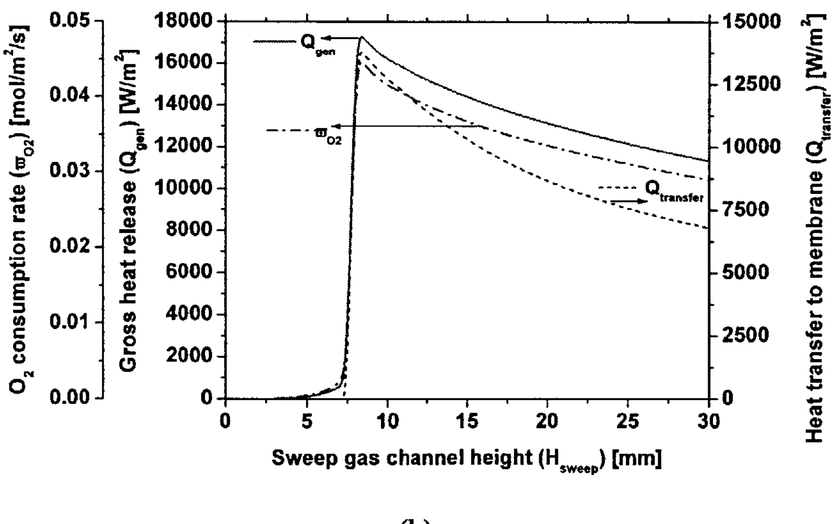

(b)

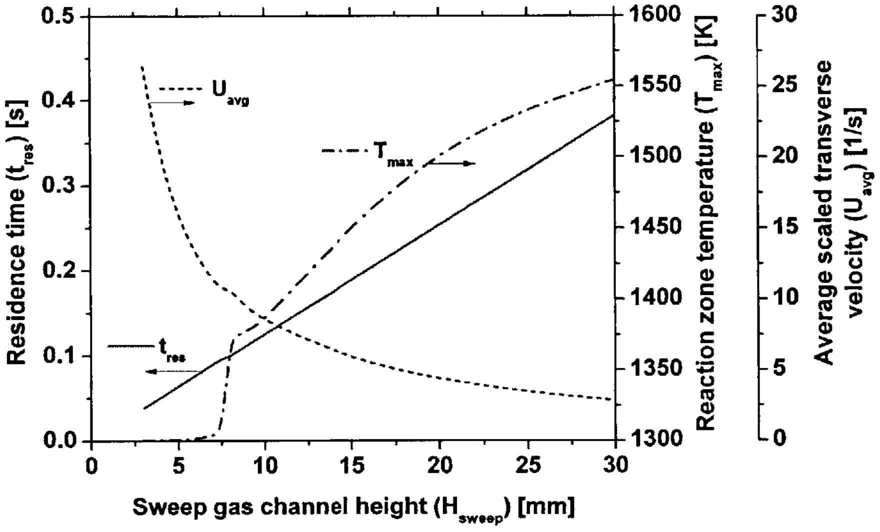

(c)

Figure 5-10 The change in: (a) the concentrations of CO_2, H_2O and O_2 at the membrane surface and the reaction zone location relative to the membrane; (b) the gross heat release from the chemical reactions, the oxygen consumption rate and the heat transfer towards the membrane; (c) the residence time, the reaction zone temperature and the average scaled transverse velocity, when the sweep gas channel height is reduced

Beyond this point, as the sweep gas channel height is reduced further, the O_2 concentration near the membrane decreases again. The H_2O concentration at the membrane surface remains constant and then decreases to a substantially small value. As the reaction zone approaches the membrane with decreasing the channel height, mass transfer is enhanced, reducing the O_2 concentration at the membrane surface and enhancing oxygen permeation. However, the concentration of the primary product, H_2O, at the membrane surface remains constant, which does not contribute to the reduction of the O_2 concentration, even if the reaction zone is established closer to the membrane. This phenomenon and the sudden increase in the magnitude of the oxygen partial pressure are explained by the low fuel concentration and the limited enhancement of the fuel oxidation reactions in the gas-phase and their extinction with a reduction of the sweep gas channel height, as shown in **Figure 5-10**(b). The gross heat release is raised with a reduction of the sweep gas channel height, enhancing the O_2 consumption rate and the heat transfer towards the membrane. Note that heat transfer to the membrane increases faster than the gross heat release because of the movement of the reaction zone. Given the sweep gas initial conditions, the fuel conversion is enhanced with an increase of the oxygen permeation rate. A larger amount of the permeated oxygen promotes the fuel conversion kinetics, which enhances further oxygen consumption and thus the oxygen permeation rate. However, the gross heat release does not rise as fast as the oxygen permeation rate. In addition, as explained in Section 5.2.4, the low CH_4 concentration results in a small rise of the H_2O concentration. Thus, although the formation of H_2O is slowly promoted (i.e., a small increase in the gross heat release), its transport towards the membrane is reduced as compared to that of CO_2, maintaining the H_2O concentration at the membrane surface constant and making the oxygen partial pressure rather dependent on the CO_2 concentration. As soon as the fuel conversion is substantially limited due to the extinction of homogeneous fuel oxidation reactions, the production of H_2O and the consumption of the permeated oxygen vanish, increasing the oxygen partial pressure significantly. Therefore, along with the oxidation reactions in the gas-phase, the location of the reaction zone with respect to the membrane plays an important role in determining the extent of the mass and heat transfer and hence the oxygen permeation rate.

Extensive heat loss, a smaller residence time and the stretched flow field in the direction parallel to the membrane cause the limited enhancement of homogeneous fuel oxidation reactions and eventually lead to their extinction. **Figure 5-10**(c) shows that the residence time is gradually lowered, while the average scaled transverse velocity increases continuously, as the sweep gas channel height is reduced. In the meantime, the reaction zone temperature is lowered and drops to a small value around $H_{sweep} \approx 7.5mm$, coinciding with a reduction of the CH_4 conversion to zero. Given a constant normal velocity of the sweep gas stream, a smaller sweep gas channel height lowers the residence time (see Eq. 5-4) and makes the flow field more stretched in the transverse direction, resulting in a higher transverse velocity, analogous to what is seen for the sweep gas flow rate variation. Furthermore, the heat loss towards the membrane increases significantly as the reaction zone is shifted towards the membrane. Note that the extinction of the gas-phase reactions coincides nearly with the channel height at which the reaction zone reaches the membrane. As a result of the reduced residence time, the flow field more stretched in the direction parallel to the membrane and slower kinetic rates due to the heat loss from the reaction zone, the growth of the gross heat release and accordingly the CH_4 conversion is not as fast as that of the oxygen permeation rate, and the diffusion-controlled reactions extinguish at small sweep gas channel height. Thus, changing the sweep gas channel height not only affects the mass and heat transfer via the reaction zone location, it also influences the residence time and the flow field for fuel conversion processes.

5.3. Feedback interactions

Results of the parametric analysis show that fuel conversion and oxygen permeation are strongly interconnected through the change in several dependent variables, e.g., reaction zone location relative to the membrane, oxygen consumption rate, residence time, etc. **Figure 5-11** shows schematically the feedback interactions between the dependent variables and the oxygen permeation rate, all of which have effects on the CH_4 conversion. As discussed Section 5.2, the sweep gas initial conditions and the reactor geometry play significant roles in influencing the local thermodynamic state and hence the fuel oxidation kinetics, affecting the gross heat release, the oxygen consumption rate and the reaction zone temperature. These in turn depend on the homogeneous fuel oxidation reactions and the flow field. In addition, the reaction zone location with respect to the membrane influences the local thermodynamic state through the mass and heat transfer towards it, changing the amount of the reaction products and thermal energy transported towards the membrane. Thus, the dependent variables encapsulating the chemical effect, the mass and heat transfer and the flow field are closely interconnected and have significant impacts on thermodynamic state at the membrane surface, i.e., the oxygen partial pressure in the immediate vicinity of the membrane and its temperature, and the oxidation kinetic rates. When the control parameters or independent variables are changed, both the chemical and heat and mass transfer effects determine the oxygen permeation rate and the CH_4 conversion.

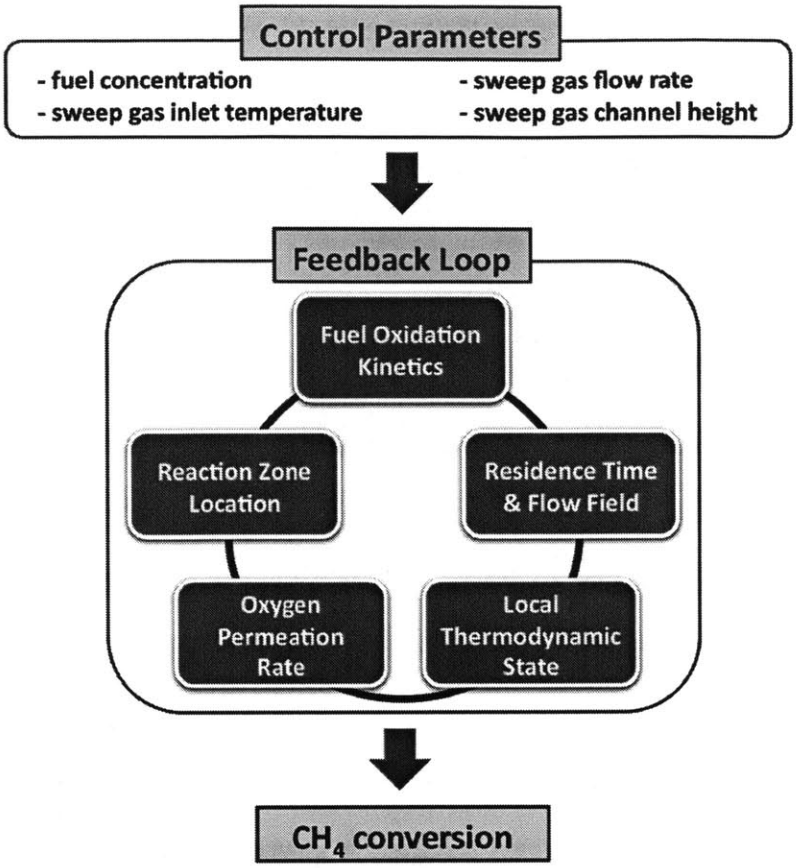

Figure 5-11 The feedback interactions among important dependent variables affecting the oxygen permeation rate and the CH_4 conversion with respect to the variation of the control parameters or independent variables

When a reactive gas is employed on the sweep side of an ITM, the local thermodynamic state changes significantly between the membrane surface and the opposite wall or sweep gas inlet, through the variations of the dependent variables by influencing the chemical reactions and the energy and species transport. The local thermodynamic state is governed by the diffusion-controlled oxidation reactions and the mass and heat transfer in the gas-phase, and vice versa. Therefore, bulk stream parameters measured at the outlet of an ITM reactor cannot predict correctly the thermodynamic state in the immediate vicinity of the membrane and hence the oxygen permeation rate in the case of an ITM reactor. To control and examine the permeation rate and the amount of fuel converted, the diffusion-controlled oxidation kinetics, the reactor geometry and mass and heat transfer have to be taken into account.

5.4. Conclusions

A parametric study using numerical simulations was conducted to investigate the interactions between fuel conversion and oxygen permeation on the sweep side of an ITM. Within an ITM reactor, the oxygen permeation rate is not known a priori and rather depends on the oxygen partial pressure in the immediate vicinity of the membrane and its temperature. The oxygen permeation rate, in part, determines the oxygen concentration in the reaction zone and hence the local mass ratio of oxygen to fuel, affecting fuel conversion processes. The local thermodynamic state (i.e., species concentration and temperature) govern the diffusion-controlled reactions, i.e., non-premixed reactants, and vice versa. Control parameters including the fuel concentration in the sweep gas stream, its inlet temperature, flow rate and channel height were considered for the parametric study.

The oxygen permeation rate and the CH_4 conversion are strongly interconnected through the fuel oxidation kinetics, the reaction zone location relative to the membrane, the residence time for the chemical reactions and the oxygen partial pressure and gas temperature near the membrane, all of which have significant effects on the local thermodynamic state and hence fuel conversion and oxygen permeation. The diffusion-controlled reactions in the gas-phase depend heavily on the local thermodynamic state and affect oxygen consumption, the heat transfer and the generation of the reaction products near the membrane, resulting in substantial fuel conversion and the enhancement of oxygen permeation even without catalytic surface activity. The location of the reaction zone relative to the membrane, governed by the fuel oxidation kinetics, has large influences on the transport of the reaction products and heat from the reaction zone towards the membrane, showing the effects of the mass and energy transfer on the local thermodynamic state near the membrane. These two effects determine the oxygen concentration in the immediate vicinity of the membrane and its temperature, respectively, and hence the oxygen permeation rate. Moreover, the heat transfer towards the membrane, i.e., heat loss from the reaction zone, impacts the reaction zone temperature and accordingly the fuel oxidation kinetics. If the heat loss is too extensive such that the reaction zone temperature is lowered to a large degree, slowing down the fuel oxidation kinetics, the extent of the chemical reactions and hence their effect on fuel conversion and oxygen permeation are significantly limited. The residence time and the flow field influence the amount of fuel that can be converted following the oxidation pathway and the heat and mass transfer away from the reaction zone. The oxygen permeation rate determines the local oxygen concentration in the reaction zone and the velocity associated with the oxidizer stream, affecting the oxidation kinetics and the reaction zone location. Sufficient oxygen permeation rate, gas temperature and the residence time are needed to support gas-phase fuel conversion processes on the sweep side of an ITM. Thus, the feedback interactions among the reaction zone location, the residence time, the fuel oxidation kinetics and the local thermodynamic state near the membrane highlight the importance of the chemical and mass and heat transfer effect on the CH_4 conversion and the oxygen permeation rate. When a reactive sweep gas is employed, the diffusion-controlled oxidation kinetics and the mass and heat transfer resistance have to be accounted for in order to examine and control the operating regimes of an ITM reactor. Fuel oxidation reactions in the gas-phase enable substantial fuel conversion and oxygen permeation in the absence of catalytic surface activity. The oxygen permeation rate obtained in the parametric analysis is comparable to the values reported in the literature [61], which is on the order of 0.2~9.0 μmol/cm^2/s and based on ITM reactors, which are believed to include catalytic fuel conversion.

Chapter 6 Heterogeneous Chemistry

6.1. Overview

Perovskite membranes have been shown to exhibit not only oxygen perm-selectivity suitable for air separation [30], but also catalytic activity for hydrocarbon conversion. These membranes have been shown to act as hydrocarbon conversion catalysts [83, 99], which, coupled with oxygen permeation, could enable their use as membrane reactors, i.e., ITM reactors, in which fuel conversion reactions take place on the sweep side in the absence of nitrogen. Multiple applications have been proposed for these reactors [61]. Methane is typically used as a feedstock, and its conversion to higher hydrocarbons, i.e., oxidative coupling of methane [39, 100-102], syngas, i.e., partial oxidation of methane [45, 103, 104], or complete oxidation to carbon dioxide and water, i.e., oxy-fuel combustion [40] has been investigated. In spite of these promising applications, little is known about catalytic fuel conversion processes on the sweep side of an ITM and their interactions with oxygen permeation and the homogeneous-phase flow, transport and chemical reactions.

Examining the key features of catalytic fuel conversion and how they couple with oxygen permeation and gas-phase reactions require detailed and complex models. Conventional catalytic reactors use a mixed fuel and air stream approaching the catalysts surface and typically operate at low temperature where gas-phase reactions are negligible. In contrast, ITM reactors supply pure oxygen, separated from air prior to the chemical reactions, through the membrane to the sweep side to which a fuel is introduced. The coupling between catalytic fuel conversion and oxygen permeation is significant [101]. Since the oxygen permeation rate is not known a priori but rather depends on the local thermodynamic state (the oxygen concentration on both sides of the membrane and its temperature), fuel conversion on the membrane surface may change the extent of oxygen permeation significantly, and vice versa. Perovskite membranes typically require temperatures above 800 °C to enable oxygen permeation [30], and they have been employed at 800 ~ 1000 °C when fuel conversion is considered [61]. In this high temperature regime, the fuel conversion may take place through homogeneous as well as catalytic surface reactions and ultimately impact the extent of fuel conversion and product selectivity. Therefore, to examine the interactions and control fuel conversion and oxygen permeation, a detailed analysis that accounts for the coupling of oxygen permeation, gas-phase flow and transport, and homogeneous and heterogeneous chemistry in terms of the local thermodynamic state at both sides of the membrane surface is needed. However, the heterogeneous chemistry on an ITM surface has not been described in detail.

In this chapter, I develop a heterogeneous kinetic mechanism for a perovskite membrane. My computational model builds on my previous work, which incorporates detailed chemical kinetics and transport in the gas-phase and resolves species concentration and temperature spatially and temporally. To develop the heterogeneous chemistry for $La_{0.6}Sr_{0.4}Co_{0.2}Fe_{0.8}O_{3-\delta}$ (LSCF) membranes, the model also incorporates conservation equations for the concentrations of surface and bulk (solid-state), i.e., incorporated into the lattice, species. I first estimate the kinetic parameters for oxygen surface exchange processes using experimentally measured mean oxygen permeation rates in which an inert gas is used on the sweep side. Next, incorporating these oxygen surface exchange kinetic parameters, I estimate the kinetic parameters for catalytic surface fuel reactions by comparing the predicted permeation rates to measurements using methane [39, 101], carbon monoxide [105] or hydrogen [106] as a reactive sweep gas.

6.2. Model formulation

The heterogeneous chemistry for a high temperature ion transport membrane surface, which is coupled with the oxygen permeation and homogeneous-phase reactions and transport, is now developed by using a spatially resolved physical model. In Chapter 2, I formulated a homogeneous-phase physical model for a planar, finite-gap stagnation-flow configuration (see **Figure 6-1**), under consideration of the spatially resolved gas-phase flow, transport and chemical reactions, all of which are coupled with the oxygen permeation flux and heat flux across the membrane.

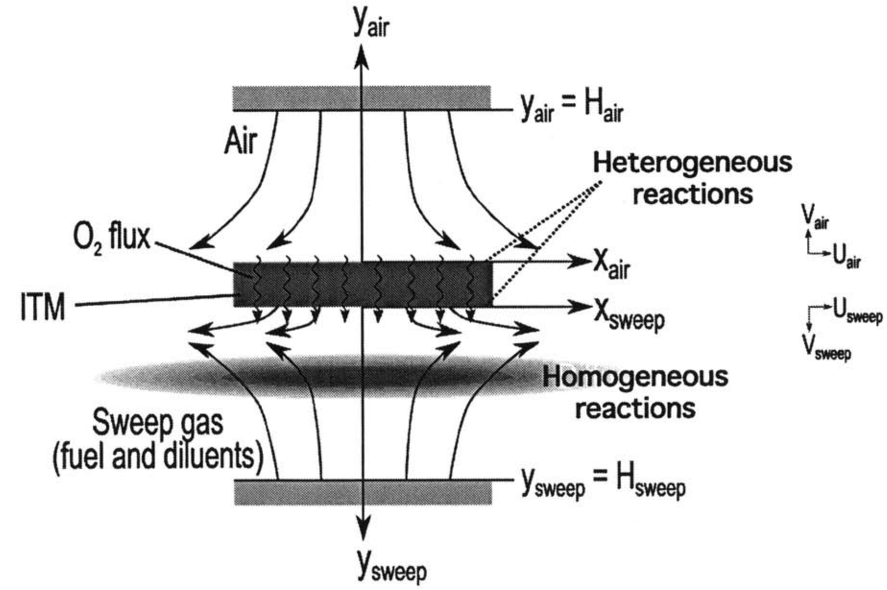

Figure 6-1 The planar, finite-gap stagnation flow configuration considered in this study, where H_{air} = air channel height and H_{sweep} = sweep gas channel height. $y_{air} = 0$ and $y_{sweep} = 0$ are located on the membrane surfaces of the air and sweep side, respectively.

In this chapter, this model is augmented to incorporate the heterogeneous chemistry. The governing equations for surface and bulk species are added, and the flux-matching boundary conditions at the membrane surface are revised to couple the surface reactions with the gas-phase local thermodynamic state near the membrane. Note that, to examine the key features of ITM reactors, detailed chemistry and transport in both homogeneous and heterogeneous phases should be considered [56, 57]. In this thesis, this is implemented by selecting the self-similar stagnation-flow configuration to keep the computational cost at a manageable level. This self-similar solution captures most of the features of typical laboratory scale reactors used to measure the permeation flux, while allowing sufficiently detailed analysis of the thermo-chemical-transport processes close to the membrane surface.

6.2.1. Species conservation equations and their coupling

The overall model, including the time dependent continuity, momentum, energy and species conservation equations, has been described in detail in Chapter 2, though here the species conservation equation is shown for illustration. The conservation equations for surface and bulk species and their reactions are implemented in the spatially resolved physical model of the stagnation flow reactor and are coupled by mass-flux-matching conditions. To account for surface reactions and the role of catalytic chemistry, the concentrations of surface and bulk species should be considered as part of the solution variables, and their conservation equations need to be taken into account. **Figure 6-2** shows how the overall field is divided into three domains and the species that belong to each domain. This includes two volumetric domains, which are the gaseous and bulk (solid) domains, and one interfacial domain between them. The transport-chemistry interaction in each domain is modeled using the appropriate form of the differential equations, while surface reactions are used to connect them, as shown in **Figure 6-2**.

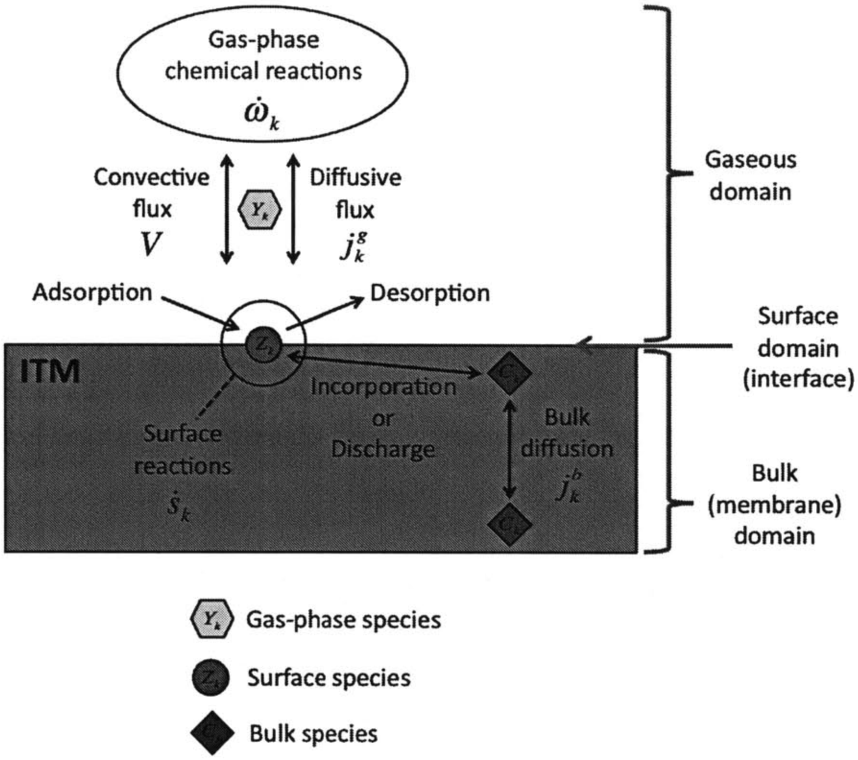

Figure 6-2 Three domains and the species belonging to each domain considered in this study. The gaseous and bulk domains are volumetric domains, whereas the surface domain is an interface domain between these two volumetric domains

The spatial variation of the gas-phase species concentration in the gaseous domain is influenced by convective and diffusive mass fluxes as well as homogeneous-phase chemical reactions. The species concentration in the gaseous domain is governed by the following equation:

$$\rho\frac{\partial Y_k}{\partial t}+V\frac{\partial Y_k}{\partial y}+\frac{\partial j_k^g}{\partial y}-\dot{\omega}_k W_k=0 \qquad \text{: Gas-phase species} \qquad \textbf{Eq. 6-1}$$

where, $j_k^g=-\rho D_{km}\left(\frac{\partial Y_k}{\partial y}+\frac{Y_k}{\bar{W}}\frac{\partial \bar{W}}{\partial y}\right)-\frac{D_k^T}{T}\frac{\partial T}{\partial y}$

where ρ is the gas-phase density [kg/m^3]; Y_k is the mass fraction of gas-phase species k; V is the convective mass flux [kg/m^2/s]; j_k^g is the diffusive mass flux of gas-phase species k [kg/m^2/s]; $\dot{\omega}_k$ is the molar production rate of gas-phase species k through homogeneous chemistry [kmol/m^3/s]; W_k is the molecular weight of gas-phase species k [kg/kmol]; D_{km} is the mixture-averaged diffusion coefficient [m^2/s]; D_k^T is the thermal diffusion (Soret effect) coefficient [kg/m/s]; $\overline{W}$ is the mixture molecular weight [kg/kmol]; T is the gas temperature [K]. A detailed chemical kinetic mechanism (GRI-Mech 3.0 [74]) is employed for the homogeneous-phase chemical reactions. Cantera [75] along with NASA polynomials is used to integrate the multi-step chemical reactions and evaluate thermodynamic and transport properties. The gaseous domains are connected with the surface domains by heterogeneous chemical reactions and other boundary conditions. At steady state, the gas-phase species produced or consumed by surface reactions should be balanced with convective and diffusive mass fluxes into or from the gaseous domain, respectively. Therefore, at the membrane surface boundary, the gaseous domain is coupled with the interface domain by the mass-flux-matching boundary conditions, described as follows:

$$V_{mem} = \sum_{k=1}^{N_g} \dot{s}_k W_k \qquad \textbf{Eq. 6-2}$$

$$j_{k,mem}^g + Y_{k,mem} V_{mem} = \dot{s}_k W_k \qquad (k = 1, \ldots, N_g) \qquad \textbf{Eq. 6-3}$$

where V_{mem} is the convective mass flux at the membrane surface [kg/m^2/s]; $j_{k,mem}^g$ is the diffusive mass flux at the membrane surface [kg/m^2/s]; $Y_{k,mem}$ is the mass fraction of gas-phase species k at the membrane surface boundary; $\dot{s}_k$ is the molar surface production rate of species k through heterogeneous chemistry [kmol/m^2/s]; N_g is the number of gas-phase species. These two matching conditions, Eq. 6-2 and Eq. 6-3, describe the transition from gas-phase to surface species.

Moreover, it is needed to relate gas-phase and surface species to the bulk (solid-state) species. The bulk species concentration immediately below the membrane surface is coupled with gas-phase and surface species by surface reactions. The model does not spatially resolve the bulk species concentration in the direction of the membrane thickness, which is governed by bulk diffusion, j_k^b (see **Figure 6-2**). The control volume approach is used to relate the volumetric bulk domain with the interface domain. The species concentration in the bulk domain is resolved by considering a small control volume $d\forall$ adjacent to the surface [107, 108]:

$$\int \hat{\rho}_{mem} \frac{\partial C_k}{\partial t} d\forall - \int \dot{s}_k \, dA + \int j_k^b \, dA = 0 \quad \text{: Bulk species} \qquad \textbf{Eq. 6-4}$$

where $\hat{\rho}_{mem}$ is the molar density of the membrane [kmol/m^3]; C_k is the concentration of bulk species k; j_k^b is the diffusive flux of bulk species k through the membrane [kmol/m^2/s]. Per the discussion in Section 6.3.1. I consider two bulk species: the oxygen vacancy and lattice oxygen ion. The bulk diffusion, j_k^b, is modeled using the charged-species transport. It has been argued that the oxygen vacancy is a mobile charged-species whose transport within the membrane represents the overall bulk diffusion process [61] and can be described by the following expression,

$$j^{b}_{V_O^{\bullet\bullet}} = -\hat{\rho}_{mem} D_{V_O^{\bullet\bullet}} \frac{\partial C_{V_O^{\bullet\bullet}}}{\partial y} \qquad \textbf{Eq. 6-5}$$

where $D_{V_O^{\bullet\bullet}}$ is the diffusivity of the oxygen vacancy inside the membrane [m^2/s]. At steady state, assuming the constant value for $D_{V_O^{\bullet\bullet}}$, this equation, Eq. 6-5, yields,

$$j^{b}_{V_O^{\bullet\bullet}} = -\frac{\hat{\rho}_{mem} D_{V_O^{\bullet\bullet}}}{L}\left(C_{V_O^{\bullet\bullet},sweep} - C_{V_O^{\bullet\bullet},air}\right) \qquad \textbf{Eq. 6-6}$$

where L is the membrane thickness [m]; $C_{V_O^{\bullet\bullet},sweep}$ and $C_{V_O^{\bullet\bullet},air}$ are the concentrations of the oxygen vacancy on the sweep and air sides of the membrane, respectively. The detailed derivation of Eq. 6-5 was discussed in Chapter 3. The diffusivity of the oxygen vacancy for an LSCF membrane was found in Chapter 3 and depends on the membrane temperature and crystalline structure. The flux of the oxygen vacancy from the sweep side to the air side is counter-balanced by the movement of bulk oxygen ions in the opposite direction. At isothermal, steady state conditions, and with small differences in the oxygen concentration across the membrane, the diffusivity of the oxygen vacancy can be assumed constant. Moreover, I assume no spatial diffusion or concentration gradients of bulk species in the transverse direction, i.e., along the membrane (x-direction in **Figure 6-1**). Thus, at steady state, the bulk species produced or consumed by surface reactions must be balanced with a diffusive flux into or from the bulk domain. At steady state, the bulk species conservation equation, Eq. 6-4, yields the flux balance or flux-matching condition at the interface,

$$\dot{s}_k = j_k^b \qquad (k = 1,\ldots,N_b) \qquad \textbf{Eq. 6-7}$$

where N_b is the number of bulk species. This condition describes the transition from surface to bulk species.

The species conservation within the interface domain is accounted for by surface reactions without species transport or mass fluxes. The following describes the surface species concentration in the surface domain:

$$\Gamma\frac{\partial Z_k}{\partial t} - \dot{s}_k = 0 \qquad \text{: Surface species} \qquad \textbf{Eq. 6-8}$$

where Γ is the total available surface site density [kmol/m^2]; Z_k is the concentration or surface site occupancy of surface species *k*. Per the discussion in Section 6.3.1, I consider two surface species: the vacant surface site and adsorbed surface oxygen anion. Note that I assume no surface diffusion or concentration gradients of surface species in the transverse direction, i.e., along the membrane (x-direction in **Figure 6-1**). At steady state, the surface species conservation equation, Eq. 6-8, yields the condition that the net production or consumption of surface species is zero,

$$\dot{s}_k = 0 \qquad (k = 1,\ldots,N_s) \qquad \textbf{Eq. 6-9}$$

where N_s is the number of surface species.

The heterogeneous kinetic mechanism developed in this chapter is based on the species concentration at and immediately below the surface domain and used for the coupling conditions between the three domains. The spatially resolved physical model enables an estimation of the kinetic parameters for surface reactions based on the local thermodynamic state, rather than the global state conventionally measured outside the reactor. In addition, as shown in Eq. 6-2 to Eq. 6-4 and Eq. 6-7 to Eq. 6-9, the species molar production rates through surface reactions relate the bulk domains and the interface domain. The production and consumption of all gas-phase, surface and bulk species from each surface reaction are considered in connecting these domains.

6.2.2. Thermal energy balance of the membrane

Heterogeneous chemical reactions may contribute to the balance of heat fluxes across the membrane. The thermal energy balance of the membrane is attributed to the conductive, convective and diffusive heat transfer with the gaseous domain (i.e., Q''_{air} and Q''_{sweep} [W/m^2]) and the heat release from surface reactions as well as the thermal radiation between the membrane and the reactor walls, which is expressed as follows:

$$Q''_{sweep} - Q''_{air} - 2\sigma\varepsilon_{mem}\left(T_{mem}^4 - T_\infty^4\right) - \sum_{k=1}^{N_s+N_b} \hat{h}_k \ \dot{s}_k = 0 \qquad \textbf{Eq. 6-10}$$

$$\textbf{where, } Q''_{air} = -\lambda \nabla T + \sum_{k=1}^{N_g}\left(j_{k,mem}^g + Y_{k,mem}V_{mem}\right)\hat{h}_k$$

$$Q''_{sweep} = \lambda \nabla T - \sum_{k=1}^{N_g}\left(j_{k,mem}^g + Y_{k,mem}V_{mem}\right)\hat{h}_k$$

where σ is the Stefan-Boltzmann constant [W/m^2/K^4]; ε_{mem} is the emissivity of the membrane; T_{mem} and T_{∞} are the membrane and surrounding wall temperature, respectively [K]; $\hat{h}_k$ is the molar enthalpy of species k [J/kmol]; λ is the mixture thermal conductivity [W/m/K]. Thermodynamic properties of surface and bulk species on perovskites are obtained from [109], assuming that they are similar to those on YSZ. Note that since typical membranes are very thin [61], I assume that no temperature gradient exists inside the membrane (i.e., uniform membrane temperature).

6.3. Heterogeneous chemistry

To characterize the catalytic activity of a perovskite membrane and examine its coupling with oxygen permeation and gas-phase transport and reactions, a description of the heterogeneous chemistry is needed. This should account for two important types of kinetics: oxygen surface exchange on both sides of the membrane and catalytic fuel conversion on the sweep side. Unlike conventional catalytic combustion in which air is fed along with a fuel approaching the catalyst surface together (i.e., co-feed), the oxygen is introduced into the reactor through the (catalytically active) membrane and the fuel as the sweep stream. Therefore, a heterogeneous kinetic mechanism must resolve catalytic fuel conversion, which is also coupled with oxygen permeation. To investigate oxygen surface exchange processes, we use data obtained using an inert sweep gas and measured by Xu and Thomson [31] and my spatially resolved physical model for flow, transport and chemistry across the entire domain. The model, expanded to include the oxygen surface exchange kinetics, is then used to estimate the kinetic parameters for catalytic fuel conversion, using the experimental data acquired when a reactive gas is introduced into the sweep side of the membrane [39, 101, 105, 106].

6.3.1. Oxygen surface exchange kinetics

6.3.1.1. Oxygen surface exchange mechanism

A multi-step oxygen permeation kinetic mechanism is considered and accounts for a sequence of surface exchange processes between the oxygen molecule in the gaseous domain and the bulk oxygen ions inside the membrane. To enable oxygen permeation through the membrane, the gaseous oxygen molecules must first be incorporated into the membrane crystalline structure. The sequence represents the interactions between the gas-phase oxygen molecules in the immediate neighborhood of the membrane, surface species, and the bulk ions inside the membrane. On the sweep side, the reverse process takes place to release the bulk ions into the gas-phase. The overall incorporation/discharge processes are described by the global oxygen surface exchange reaction shown below,

$$\frac{1}{2}O_2 + V_O^{\bullet\bullet} \leftrightarrow O_O^x + 2h^{\bullet} \qquad \textbf{Eq. 6-11}$$

where $V_O^{\bullet\bullet}$ is the oxygen vacancy; O_O^x is the lattice (bulk) oxygen ion (charge number = −2); $h^{\bullet}$ is the electron hole. This one step reaction has been widely used to model the overall surface exchange processes. However, when fuel conversion occurs on the membrane surface, this global reaction, Eq. 6-11, may not accurately capture the surface reactions because the fuel conversion reactions might influence some of the intermediate oxygen surface exchange processes. Thus, intermediate reactions need to be taken into account in order to resolve oxygen surface reactions with other species. As shown in **Figure 6-3**, it has been suggested that the global oxygen surface exchange reaction can be described by a sequence of five intermediate steps [25] summarized as follows (refer to **Figure 6-3** for step numbers, (i) through (v)):

i. adsorption/desorption of gas-phase oxygen molecules onto/from the membrane surface
ii. dissociation/association of adsorbed oxygen molecules into/from oxygen atoms
iii. electron transfer with the lattice to form singly-charged surface oxygen anions/oxygen atoms
iv. incorporation into/discharge from the crystalline structure by filling/forming an oxygen vacancy
v. electron transfer with the lattice to form fully-charged/singly-charged bulk oxygen anions

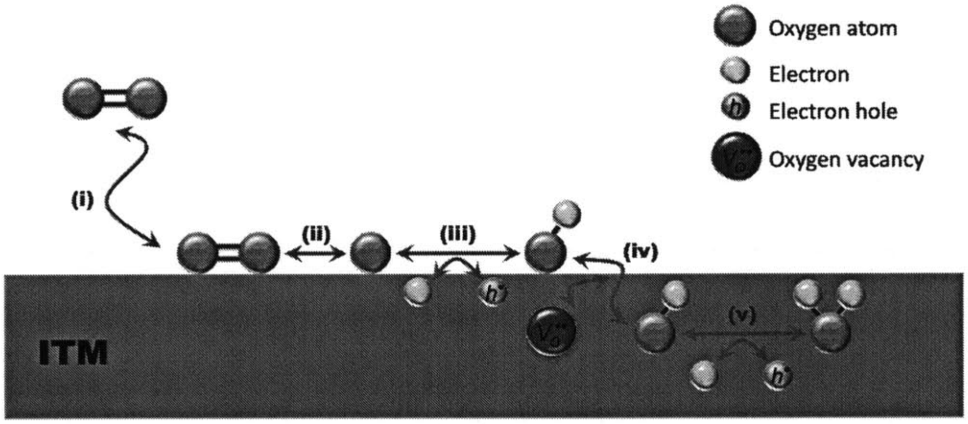

Figure 6-3 Five intermediate steps for the oxygen surface exchange process. The step (i) to (iii) corresponds to dissociative adsorption/desorption (surface reaction 1, Eq. 6-12), and the step (iv) to (v) refers to charge-transfer incorporation (surface reaction 2, Eq. 6-13)

With respect to oxygen transport, step (i) connects the gaseous domain and the interface domain, while steps (ii) and (iii) take place within the interface domain. Step (iv) relates the interface to the bulk domain, whereas step (v) occurs wholly inside the bulk domain. Using an oxygen isotope exchange technique, Boukamp et al. demonstrated that the kinetics of these five intermediate processes can be approximated by two rate-limiting single-electron transfer reaction steps [110, 111]. The first is the dissociative adsorption/desorption, Eq. 6-12, accounting for steps (i) to (iii), while the second is the charge-transfer incorporation, Eq. 6-13, describing steps (iv) and (v), as shown below,

$$O_2 + 2(s) \xleftrightarrow{k_{f,1}/k_{b,1}} 2O^-(s) + 2h^\bullet$$: Surface reaction 1 **Eq. 6-12**

$$O^-(s) + V_O^{\bullet\bullet} \xleftrightarrow{k_{f,2}/k_{b,2}} O_O^x + (s) + h^\bullet$$: Surface reaction 2 **Eq. 6-13**

where (s) is the vacant surface site on the membrane surface; $O^-(s)$ is the adsorbed singly-charged surface oxygen anion; $k_{f,i}$ and $k_{b,i}$ are the reaction rate constants of forward and backward reactions, respectively, of Eq. 6-12 and Eq. 6-13; the subscript number in the reaction rate constants is the corresponding reaction number. The reaction rate constants, $k_{f,i}$ and $k_{b,i}$, are assumed in an Arrhenius format, as shown below:

$$k = AT_{mem}^n \exp\left(\frac{-E_A}{RT_{mem}}\right)$$ **Eq. 6-14**

where A is the pre-exponential factor; n is the temperature exponent; E_A is the activation energy [J/mol]; R is the universal gas constant [J/mol/K]. To model the two rate-limiting steps, the concentrations of two surface species, (s) and $O^-(s)$, and two bulk species, $V_O^{\bullet\bullet}$ and O_O^x, are introduced as thermodynamic state variables in the analysis. Note that typical perovskite membranes have a high electronic conductivity, and hence, at steady state, the concentration of electron holes is considered constant throughout the membrane and its impact on the surface exchange reaction rate can be neglected. Then, the net reaction rates, $\dot{R}_i$ [kmol/m^2/s], of Eq. 6-12 and Eq. 6-13 are expressed as follows:

$$\dot{R}_1 = k_{f,1}\left(\frac{\rho Y_{O_2}}{W_{O_2}}\right)\left(\Gamma Z_{(s)}\right)^2 - k_{b,1}\left(\Gamma Z_{O^-(s)}\right)^2 \qquad \textbf{Eq. 6-15}$$

$$\dot{R}_2 = k_{f,2}\left(\Gamma Z_{O^-(s)}\right)\left(\hat{\rho}_{mem} C_{V_O^{\bullet\bullet}}\right) - k_{b,2}\left(\hat{\rho}_{mem} C_{O_O^x}\right)\left(\Gamma Z_{(s)}\right) \qquad \textbf{Eq. 6-16}$$

Summing up these two reaction rates, we obtain the molar production rate of each species participating in the oxygen surface exchange reactions:

$$\dot{s}_k = \sum_{i=1}^{N_R} \nu_{k,i}\, \dot{R}_i \qquad \textbf{Eq. 6-17}$$

where N_R is the number of surface reactions; the subscript *i* is the reaction number; $\nu_{k,i}$ is the stoichiometric coefficient of species *k* in the reaction *i*. As seen in Eq. 6-15 and Eq. 6-16, surface reactions and their reaction rates link gas-phase, surface and bulk species. Note that Y_k, C_k and Z_k shown in Eq. 6-15 and Eq. 6-16 are the local species concentration in the gas-phase or on the membrane surface (i.e., interface domain). Thus, the reaction rate constants, $k_{f,i}$ and $k_{b,i}$, should be determined in terms of these local thermodynamic state variables, as will be evident in

Section 6.4.

6.3.1.2. Estimation of kinetic rate parameters

The oxygen surface exchange kinetic parameters were estimated using the spatially resolved physical model, the surface kinetics model and the experimentally measured oxygen permeation rates. Using the LSCF membrane with an inert sweep gas, Xu and Thomson measured the oxygen permeation rates in a typical disc-type stagnation-flow permeation apparatus [31]. I use their data to estimate the kinetic parameters in Eq. 6-15 and Eq. 6-16. The experimental conditions at which the permeation rates were measured, including the air and sweep gas flow rates, the molar compositions, and temperature, were used as boundary conditions at the air and sweep gas reactor inlets for the spatially resolved physical model. Given these inlet conditions and measured average flux, the oxygen surface exchange kinetic parameters were manually adjusted, such that difference between the calculated and measured fluxes was minimized. Note that each surface reaction, Eq. 6-12 and Eq. 6-13, needs forward and backward reaction rate constants, k_f and k_b. That is, twelve parameters must be evaluated (refer to Eq. 6-14). Since the equilibrium constants of these two rate-limiting reactions are not known, the forward and reverse reaction rate constants were separately determined using the four reactions (i.e., forward and backward reactions of Eq. 6-12 and Eq. 6-13). First, because the oxygen permeation rates are predominantly governed by the membrane temperature, the sensitivity of each reaction to the temperature was examined by changing its activation energy, E_A, and temperature exponent, n. The activation energies and temperature exponents of the four reactions were tuned simultaneously until we achieved the same temperature dependency of the predicted permeation rates as that of the measurements. Second, the four pre-exponential factors are varied to obtain the same absolute oxygen permeation rates as the experimentally measured values. The estimated values of these twelve oxygen surface exchange kinetic parameters are shown in **Table 6-1**.

Table 6-1 The oxygen surface exchange kinetic parameters for the two rate-limiting reactions and the catalytic fuel conversion kinetic parameters for CH_4, CO and H_2 oxidation (the units of the pre-exponential factor, A, are in kmol, m^3, second)

Reaction number	Reactions	Reaction rate coefficients	Pre-exponential factor, A	Exponent for temperature, n	Activation energy, E_A [J/mol]
Oxygen surface exchange kinetics					
1	$O_2 + 2(s) \leftrightarrow 2O^-(s)$	$k_{f,1}$	1.00 E+30	0	2.68 E+05
		$k_{b,1}$	2.30 E+27	3.6	3.15 E+05
2	$O^-(s) + V_O^{\bullet\bullet} \leftrightarrow O_O^x + (s)$	$k_{f,2}$	1.20 E+13	5.2	3.66 E+05
		$k_{b,2}$	3.30 E+07	5.2	4.35 E+05
Catalytic fuel conversion kinetics					
3	$2CH_4 + O_O^x \rightarrow 2CH_3 + H_2O + V_O^{\bullet\bullet}$	$k_{f,3}$	3.20 E+14	0	2.17 E+05
4	$CO + O_O^x \rightarrow CO_2 + V_O^{\bullet\bullet}$	$k_{f,4}$	4.79 E+02	0	3.10 E+04
5	$H_2 + O_O^x \rightarrow H_2O + V_O^{\bullet\bullet}$	$k_{f,5}$	1.10 E+02	0.75	8.86 E+04

The oxygen permeation rates estimated considering this parameterization of the surface exchange kinetics are in good agreement with experimental results. As shown in **Figure 6-4**(a), the estimated oxygen surface exchange kinetic parameters result in an oxygen permeation rate that matches the measurements very well.

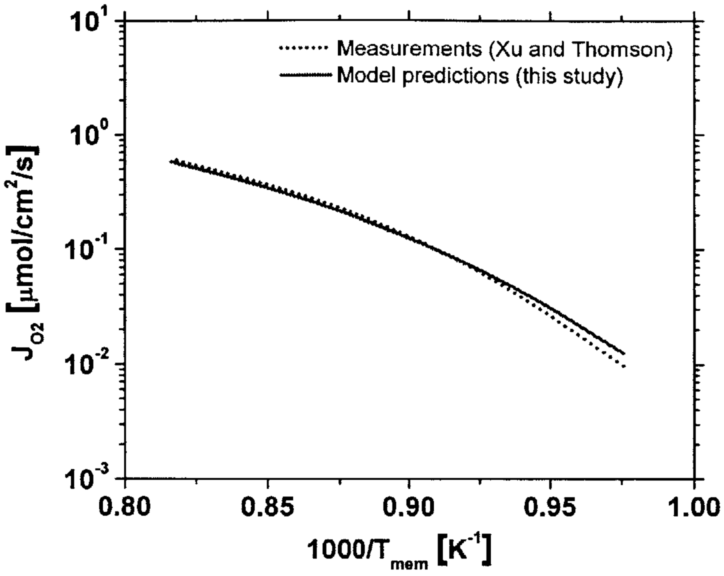

(a)

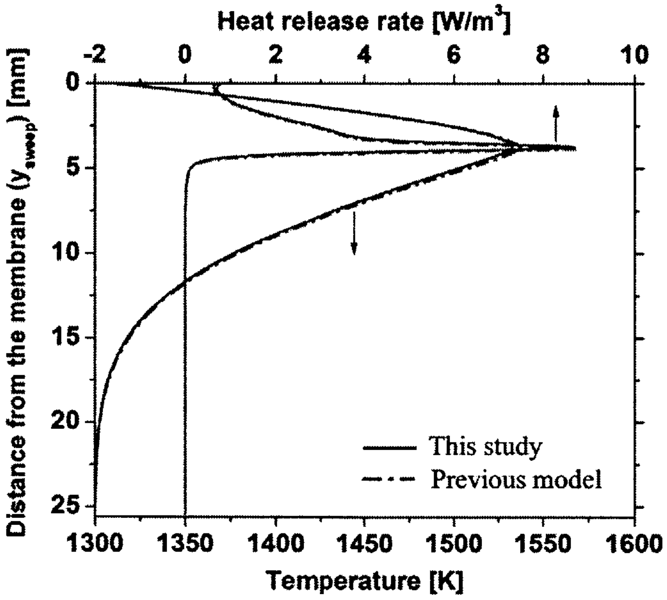

(b)

Figure 6-4 (a) Comparison between the oxygen permeation rates estimated using the oxygen surface exchange kinetic parameters obtained in this study and those measured by Xu and Thomson [31] and (b) comparison between the heat release rate and temperature evaluated using the oxygen surface exchange kinetic parameters obtained in this study and those estimated by the previous numerical model using a one-step oxygen permeation expression

The oxygen surface exchange kinetic parameters are also implemented at the sweep side of the membrane in cases when a reactive sweep gas is introduced. The reactive sweep gas conditions refer to Chapter 4, which include a methane concentration of 6% on a molar basis with the remainder being carbon dioxide, a sweep gas inlet temperature of 1300 K and a sweep gas flow rate of 4.39×10^{-4} m^3/s. At these conditions, it has been shown that reactants are mostly oxidized through gas-phase reactions and hardly reach the membrane surface, limiting the role of catalytic fuel conversion. Thus, only the oxygen surface exchange reactions take place at the membrane surface, enabling us to examine the estimated oxygen surface exchange kinetics when a reactive sweep gas is introduced, with the assumption of negligible catalytic fuel conversion kinetics. As shown **Figure 6-4**(b), the predicted temperatures and heat release rates are in very good agreement with those reported in Chapter 4.

Figure 6-5 shows the oxygen surface exchange reaction rates for LSCF estimated by here using our spatially resolved physical model on the same plot along with those for $(Y_2O_3)_{0.08}(ZrO_2)_{0.92}$ (YSZ), $La_2NiO_{4+\delta}$ (LNO) and $Ba_{0.5}Sr_{0.5}Co_{0.8}Fe_{0.2}O_{3-\delta}$ (BSCF) measured experimentally by Bouwmeester et al. [112]. The reaction rates calculated using the estimated kinetic parameters for LSCF fall in between those of YSZ and LNO. In all cases, the overall oxygen surface exchange processes are limited by the dissociative adsorption/desorption, Eq. 6-12 (R_I in **Figure 6-5**). This is consistent with the results by Bouwmeester et al., in which they measured the reaction rates of Eq. 6-12 and Eq. 6-13 for YSZ, LNO and BSCF using a pulse isotopic exchange technique and showed that the dissociative adsorption/desorption was rate-limiting. In addition, it is shown that oxygen surface exchange reactions estimated numerically for LSCF membrane are slower than those on LNO and BSCF, and faster than those on YSZ.

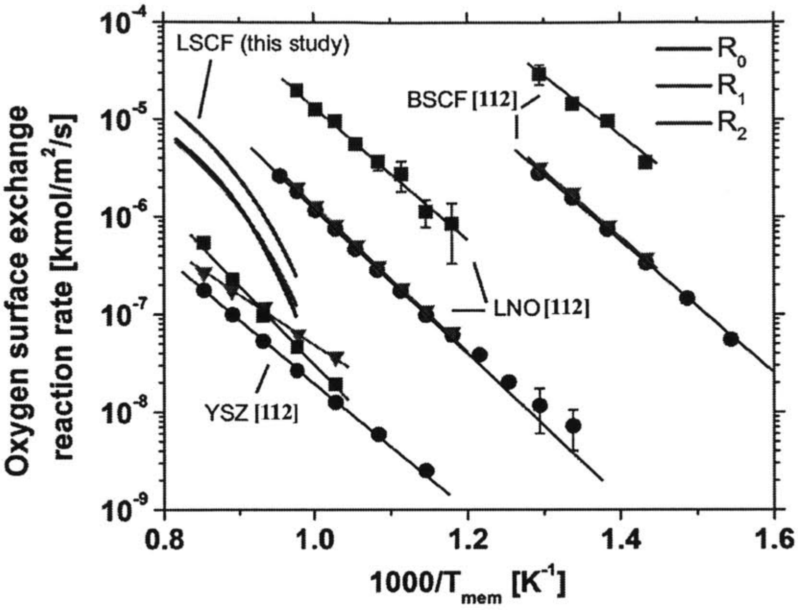

Figure 6-5 The oxygen surface exchange reaction rates for LSCF estimated by the spatially resolved physical model. Experimentally determined exchange rates for YSZ, LNO and BSCF [112]. R_0 is the global surface exchange reaction rate for Eq. 6-11, while R_1 and R_2 corresponds to Eq. 6-15 and Eq. 6-16 for the two rate-limiting reactions.

6.3.2. Catalytic fuel conversion kinetics

Perovskite membranes have been proposed for fuel conversion applications such as oxy-fuel combustion and oxidative coupling of methane and have been shown to have some catalytic activity towards hydrocarbon conversion [83]. When implemented as high temperature membrane reactors, they can be used for either oxy-fuel combustion to yield completely oxidized products, i.e., carbon dioxide and water [40] or oxidative coupling of methane to produce higher hydrocarbons, i.e., ethane or ethylene [99]. Although they have also been employed for syngas production, the product selectivity for syngas is substantially low without an additional catalyst mounted on the membrane surface [45]. The catalytic activity of perovskites for syngas production is not as strong as typical fuel conversion catalysts such as Nickel, Rhodium or

Platinum, and the extent of fuel conversion from these membrane reactors is significantly low [61]. In addition, the product selectivity is difficult to control when homogeneous chemistry plays a role and influences the final products. To control the fuel conversion and product selectivity effectively, the catalytic fuel conversion processes in a membrane reactor should be investigated further.

So far, the reaction mechanisms on a perovskite membrane surface have not been identified, and available measurements are not sufficient to formulate detailed surface reaction models. In light of this, I start with a set of global reactions for a number of reactants, i.e., methane, carbon monoxide and hydrogen, to model catalytic fuel conversion on the membrane surface. The reaction rate parameters for catalytic fuel conversion are estimated by using the spatially resolved physical model described so far and experimentally measured permeation rates introducing methane [39, 101], carbon monoxide [105] or hydrogen [106] to a sweep side. Among the measured fuel conversion, product selectivity and permeation rate, the oxygen permeation rates are most reliable, as the other two are more sensitive to gas-phase reactions. The experimental conditions at which the permeation measurements were carried out, i.e., the air and sweep gas flow rates, the molar compositions, and temperature, are used as boundary conditions at the air and sweep gas inlets for the model. Given these inlet conditions, the pre-exponential factor or activation energy or both for reaction rate constants was manually adjusted in order to obtain the same permeation rates as measured experimentally. Note that homogeneous chemistry is also implemented during the estimation of catalytic fuel conversion kinetic parameters in order to account for the possible influence of gas-phase reactions on the oxygen permeation and fuel conversion processes.

6.3.2.1. CH_4 catalytic conversion

Experimental work has suggested that methane is catalytically converted in an ITM reactor, which produces ethane or ethylene [39, 100-102]. Oxygen permeates through the membrane in the form of oxygen ions. The surface reactions of these oxygen ions with methane on the sweep side yield C_2 hydrocarbons while inhibiting the formation of CO_x through the homogeneous-phase chemical reactions by reducing the availability of gas-phase oxygen [61]. This increases the C_2 selectivity of ITM reactors. It has been shown that a C_2H_6/O_2 co-feed reactor with no catalyst results in higher CO_x yields than when an LSCF surface is placed in the reactor [101]. This implies that the production of CO_x takes place in the homogeneous phase and that LSCF can suppress the production of CO_x by acting as an oxidative coupling of methane catalyst. It should be noted, however, that this study was carried out under fuel rich conditions and this conclusion may not necessarily hold true for fuel/oxygen ratios closer to the stoichiometric ratio. On the other hand, Tan et al. [40] proposed that methane oxidation to carbon dioxide is also catalytically supported. However, they used a co-feed fixed bed reactor packed with granular LSCF, and hence their measurements are not representative of ITM reactors. To elucidate if perovskites can act as an oxidative coupling of methane catalyst or an oxidation catalyst, measurements such as product concentrations in the vicinity of the membrane are needed. Since they are not available, this study relies on the conventional wisdom that perovskites can contribute to catalytic conversion of methane to methyl radical [58] when they are primarily used for oxidative coupling of methane. If experimental evidence showing that CO_x is also a primary product from catalytic reactions is available, its reaction will need to be included in the surface kinetic model.

Most researchers agree that, in oxidative coupling, two successive steps can describe the overall processes [58], although the detailed conversion mechanism for methane on the ITM surface is still not resolved:

1. adsorption of methane, its conversion to methyl radicals by an oxygen ion on the membrane surface and the desorption of methyl radicals to the gas-phase
2. association of two methyl radical molecules in the gas-phase to form ethane or ethylene

With respect to the step (i), Wang and Lin [58] has proposed the following reaction,

$$2CH_4 + O_O^x \xrightarrow{k_{f,3}} 2CH_3 + H_2O + V_O^{\bullet\bullet} \quad \text{: Surface reaction 3} \qquad \textbf{Eq. 6-18}$$

In this step, the methane conversion reaction consumes the oxygen directly on the membrane surface, competing with the reaction discharging oxygen into the gas-phase (i.e., backward reaction of Eq. 6-11). The methyl radicals produced from this reaction can be oxidized or combined to form higher hydrocarbons such as ethane in the gas-phase (step (ii)), which is resolved by detailed homogeneous chemistry implemented in our numerical model. The reaction rate of Eq. 6-18 is expressed as,

$$\dot{R}_3 = k_{f,3}\left(\frac{\rho Y_{CH_4}}{W_{CH_4}}\right)^2 \left(\Omega C_{O_O^x}\right) \qquad \textbf{Eq. 6-19}$$

The activation energy of $k_{f,3}$ was evaluated by ten Elshof et al. [39] using their LSCF membrane reactor. To obtain the pre-exponential factor of $k_{f,3}$, we use the spatially resolved physical model and the experimental measurements of the oxygen permeation rates by Xu and Thomson [101] with methane in the sweep gas mixture. The experimental conditions at which they acquired the measurements, including the air and sweep gas flow rates, their molar compositions and temperature, are used as boundary conditions at the air and sweep gas inlets in the model. Given the inlet conditions, we conduct the numerical simulations while tuning the pre-exponential factor of $k_{f,3}$ in order to obtain the same permeation rates as measured experimentally. The estimated value of the parameter is shown in **Table 6-1** for a temperature range of 1073K to 1223K and methane concentrations 25% to 100% on a molar basis. Since the kinetic parameters for the methane decomposition reaction obtained in this study is based on an ITM reactor experiment, they are more representative of the membrane catalytic activity than the values previously estimated [58], in which it was assumed that perovskite membranes behave catalytically in a way similar to Li/MgO membranes leading to a significantly lower activation energy.

During the parameterization of the catalytic CH_4 conversion reaction using the overall model, the homogeneous-phase chemical reactions were found to be relevant only near the membrane surface. **Figure 6-6** shows the gas-phase molar production rates of methane, methyl radical, ethylene and ethane as estimated by the spatially resolved physical model incorporating the heterogeneous methane decomposition, given the sweep side conditions considered in the experiment. These are negligible in most of the gaseous domain on the sweep side, with the exception of the region approximately 1 mm from the membrane. Since the operating temperature, 1098 K, considered in the experiment is well below the ignition temperature for the onset of homogeneous chemistry, the effect of gas-phase reactions was suppressed. However, if the sweep gas inlet temperature is raised above this value, homogeneous chemistry can be initiated, and its coupling with catalytic surface reactions can be important. In the immediate vicinity of the membrane, the methyl radicals produced from the surface reaction, Eq.18, are combined in the gas-phase to form ethylene and ethane, indicating the oxidative coupling of methane.

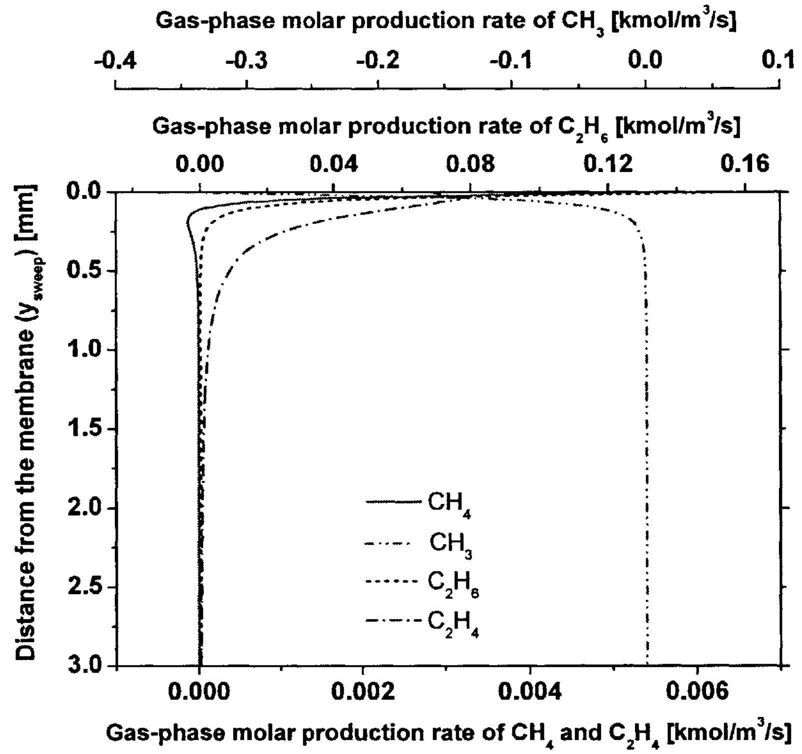

Figure 6-6 The molar production rate of CH_4, CH_3, C_2H_6 and C_2H_4 from the homogeneous-phase reactions as predicted by the spatially resolved physical model, given the sweep side conditions considered in experiments performed by Xu and Thomson [101]. The surface molar production rate of CH_4 is −1.02 kmol/m^2/s, while that of CH_3 is 1.02 kmol/m^2/s.

In addition, when this ethane reacts further with the methyl radicals produced from heterogeneous chemistry, the formation of methane in the gas-phase is favored through the following reactions,

$$CH_3 + C_2H_6 \leftrightarrow C_2H_5 + CH_4 \qquad \textbf{Eq. 6-20}$$

This effect reduces the extent of the overall CH_4 conversion, even if the conversion of methane is catalytically supported at the membrane surface. I conclude that the interactions between homogeneous and heterogeneous chemistry are important and should be considered in the analysis of fuel conversion processes in ITM reactors.

6.3.2.2. CO surface oxidation

In addition to methane conversion, the surface oxidation of carbon monoxide to carbon dioxide can be supported by the catalytic activity of perovskite membranes. van Hassel et al. [113] and ten Elshof et al. [105] demonstrated that the oxygen permeation rates increase when introducing carbon monoxide in the sweep side, in comparison with those at sweep side conditions using an inert sweep gas. They also showed that the oxygen permeation flux is raised with an increase of the carbon monoxide concentration in the sweep stream, arguing that the catalytic oxidation of carbon monoxide with oxygen on the membrane surface may contribute to the enhancement of the oxygen permeation rate. In addition, it has been shown that carbon monoxide produced from methane in the gas-phase reactions can reach the membrane surface when the gas-phase reaction zone approaches the membrane. Therefore, the following carbon monoxide oxidation reaction should be included in the development of heterogeneous chemistry,

$$CO + O_O^x \xrightarrow{k_{f,4}} CO_2 + V_O^{\bullet\bullet} \qquad \text{: Surface reaction 4} \qquad \textbf{Eq. 6-21}$$

The catalytic oxidation of carbon monoxide consumes the oxygen directly on the membrane surface, which enhances oxygen permeation. The reaction rate of Eq. 6-21 is expressed as,

$$\dot{R}_4 = k_{f,4}\left(\frac{\rho Y_{CO}}{W_{CO}}\right)\left(\Omega C_{O_O^x}\right) \qquad \textbf{Eq. 6-22}$$

The activation energy of $k_{f,4}$ was evaluated by ten Elshof et al. [105] using their LSF membrane reactor. Assuming that LSCF membranes show similar catalytic behavior to that of the LSF membrane, we use the same value of the activation energy. To obtain the pre-exponential factor of $k_{f,4}$, we use the spatially resolved physical model and the experimentally measured oxygen permeation rates by ten Elshof et al., introducing carbon monoxide to the sweep side. The operating conditions at which they acquired their measurements, including the air and sweep gas flow rates, the molar compositions and temperature, are used as boundary conditions at the air and sweep gas inlets. Given the inlet conditions, we perform the numerical simulations while changing the pre-exponential factor of $k_{f,4}$ in order to obtain the same permeation rates as those measured experimentally. The estimated value of the parameter is shown in **Table 6-1** for a temperature range of 1173K to 1323K and carbon monoxide concentrations of 5% to 25% on a molar basis.

During the estimation of the kinetic parameters for carbon monoxide catalytic oxidation, the effect of the homogeneous chemistry on CO oxidation and oxygen permeation were found to be negligible. **Figure 6-7** shows the gas-phase molar production rates of carbon monoxide and oxygen as estimated by the overall spatially resolved physical model incorporating the heterogeneous CO oxidation, given the sweep side conditions considered in the experiment.

These are negligible throughout the gaseous domain on the sweep side, indicating the suppression of the homogeneous-phase reactions. This can be attributed to the absence of the hydroxyl radical which is required to oxidize carbon monoxide in the gas-phase. Since we did not introduce hydrogen-containing gas in the sweep stream, the hydroxyl radical could not be formed or contribute to carbon monoxide oxidation in the gas-phase. In cases when methane is added to the sweep stream, it will provide the hydroxyl radical, and homogeneous oxidation will be accelerated. The relative roles of both depend on the condition and will be investigated in a future study.

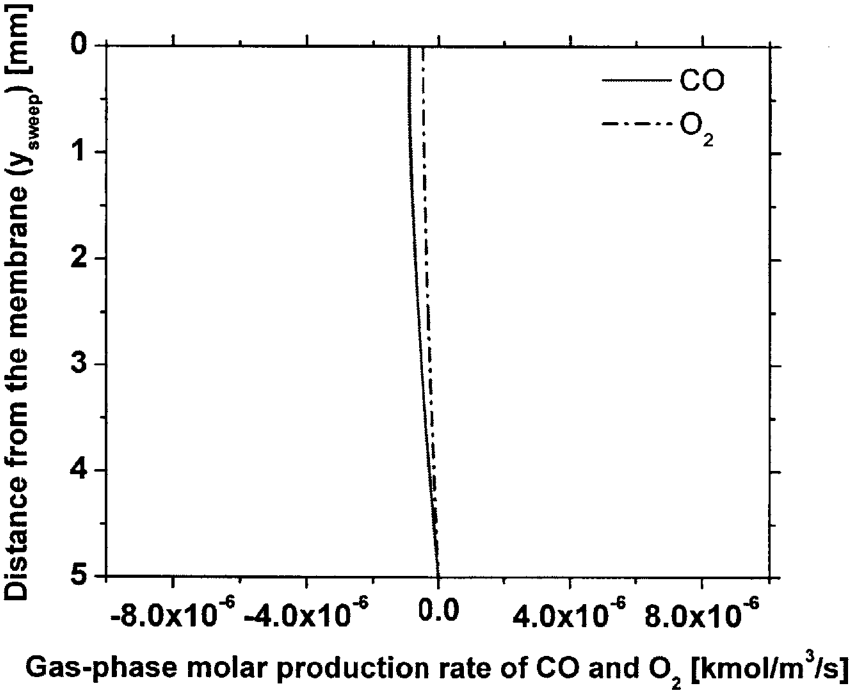

Figure 6-7 The molar production rate of CO and O_2 from the homogeneous-phase reactions as predicted by the spatially resolved physical model, given the sweep side conditions considered in experiments performed by ten Elshof et al. [105]. The surface molar production rate of CO is −5.51 kmol/m^2/s.

6.3.2.3. H_2 surface oxidation

Perovskite membranes may contribute to the catalytic oxidation of hydrogen. Tan et al. [106] showed evidence that the oxygen permeation flux is raised with an increase of the hydrogen concentration in the sweep stream, and a large amount of water is produced due to the reactions. Furthermore, I showed that hydrogen produced from methane in the gas-phase reactions can reach the membrane surface when the gas-phase reaction zone is established in the vicinity of the membrane. I therefore propose to use the following oxidation reaction to account for the perovskite membrane catalytic activity for hydrogen oxidation, when constructing heterogeneous chemistry,

$$H_2 + O_O^x \xrightarrow{k_{f,5}} H_2O + V_O^{\bullet\bullet} \qquad \text{: Surface reaction 5} \qquad \textbf{Eq. 6-23}$$

The catalytic oxidation of hydrogen consumes the oxygen directly on the membrane surface, increasing the oxygen permeation rate. The reaction rate of Eq. 6-23 is expressed as,

$$\dot{R}_5 = k_{f,5}\left(\frac{\rho Y_{H_2}}{W_{H_2}}\right)\left(\Omega C_{O_O^x}\right) \qquad \textbf{Eq. 6-24}$$

To obtain the activation energy, exponent for temperature and pre-exponential factor of $k_{f,5}$, we use the spatially resolved physical model and the experimentally measured oxygen permeation rates by Tan et al. [106] introducing hydrogen into the sweep side. They use the LSF membrane reactor in their experiments. Assuming that LSCF membranes show similar catalytic activity for hydrogen oxidation to that of the LSF membrane, we use their measurements against which the kinetic parameters of Eq. 6-23 are fitted. Again, the numerical boundary conditions are taken from the experimental investigation, and the activation energy, exponent for temperature and pre-exponential factor are manually adjusted to achieve optimal agreement between the measured and calculated fluxes. Since the oxygen permeation flux is predominantly dependent on the membrane temperature, the sensitivity of $k_{f,5}$ to the temperature is first examined. The activation energy and temperature exponent are varied simultaneously until achieving the same temperature dependency of the predicted permeation rates as that of the measurements. Then, the pre-exponential factor is tuned to obtain the same oxygen permeation rates as those measured by Tan et al. The estimation of the kinetics parameters is summarized in **Table 6-1** for a temperature range of 973K to 1273K and a hydrogen concentration of 30.8% on a molar basis.

In contrast to the other two cases in which methane or carbon monoxide was added to the sweep gas (refer to Section 6.3.2.1 and 6.3.2.2), a substantial impact of gas-phase reactions on hydrogen oxidation is demonstrated by the numerical simulations given the sweep side conditions considered in the experiment. **Figure 6-8** shows the contribution of the catalytic surface reactions and the gas-phase reactions to hydrogen oxidation predicted by the model. Whereas gas-phase reactions are slow at low temperature, their role in hydrogen conversion is substantial and comparable to the catalytic reaction at high temperature. It has been typically assumed that homogeneous chemistry does not play a role in oxygen permeation and fuel conversion within ITM reactors. However, as I show in this study, both homogeneous and heterogeneous chemistry should be taken into account.

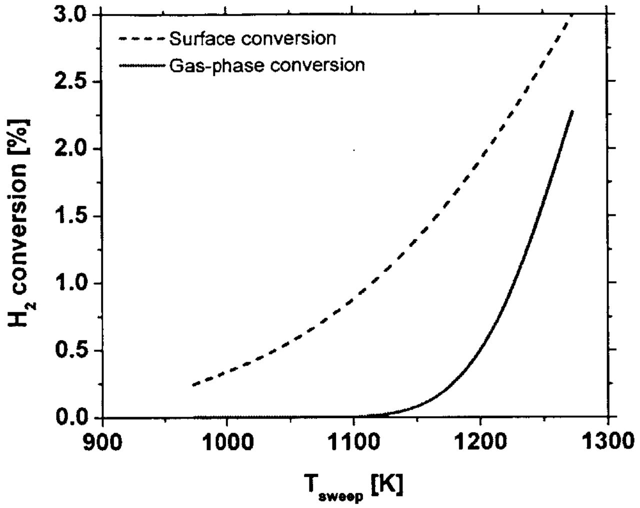

Figure 6-8 Contribution of catalytic surface reactions and homogeneous-phase reactions to hydrogen oxidation predicted by the numerical model, given the sweep side conditions considered in experiments performed by Tan et al. [106]

6.3.2.4. Evaluation of catalytic fuel conversion kinetic parameters

The kinetic parameters for catalytic fuel conversion acquired in this analysis are based on the local thermodynamic state in the immediate vicinity of the membrane surface, on both sides and above and below the surface, as represented by the species concentrations in Eq. 6-19, Eq. 6-22 and Eq. 6-24. The spatially resolved physical model accounts for these local concentrations. Mass transport and chemical reactions along the inlet and exit channels can change the species concentration and temperature significantly, which could lead to errors in the estimation of the kinetic parameters and the flux dependence on the operating conditions unless these effects are considered in the models. The spatially resolved physical model predicts this local thermodynamic state, and hence the kinetic parameters derived from it are more representative of what occurs on the membrane surface. As shown in **Figure 6-9**, the set of the reaction rate parameters for catalytic fuel conversion evaluated in this work provides estimates of the oxygen permeation rates that are in good agreement with measurements.

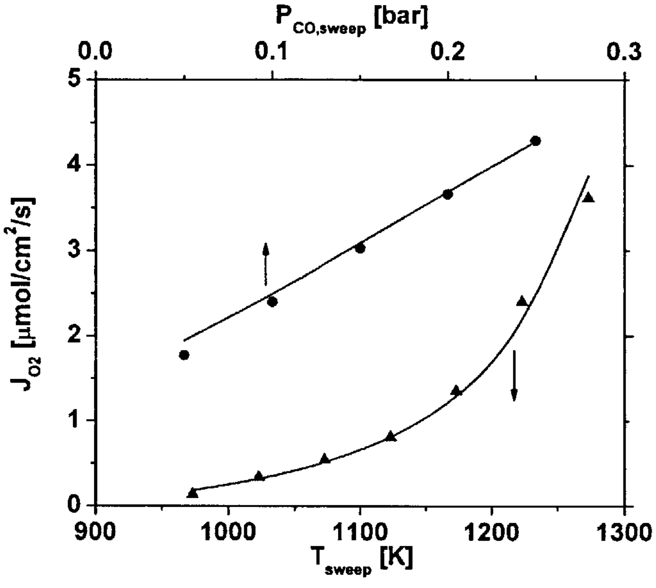

Figure 6-9 The comparison of the oxygen permeation rates estimated by the catalytic fuel conversion kinetic parameters obtained in this study and those measured by ten Elshof et al. [105] and Tan et al. [106]

The catalytic activity for methane conversion and carbon monoxide oxidation predominantly govern the overall surface reactions on the membrane surface. **Figure 6-10** shows the three reaction rate constants obtained in this study for CH_4 catalytic conversion CO and H_2 surface oxidation. The reaction rate constant of CH_4 catalytic conversion is strongly dependent on temperature, whereas those of CO and H_2 surface oxidation are less sensitive to temperature. As a result, at low temperature (< 850 °C) CO surface oxidation limits the overall kinetics, while CH_4 catalytic conversion is rate-limiting at high temperature (> 850 °C). Since ITM reactors operate at high temperature (i.e., above 900 °C), the CH_4 catalytic conversion reaction may play an important role in fuel conversion and the enhancement of oxygen permeation. Furthermore, comparing Eq. 6-19, Eq. 6-22 and Eq. 6-24, the CH_4 catalytic conversion reaction is a second-order reaction with respect to the gas-phase species concentration, while the other two are first-order reactions. Therefore, given the same gas-phase species concentration in the immediate neighborhood of the membrane, the catalytic CH_4 conversion reaction is faster than other two reactions, and its effect is stronger in determining fuel conversion and oxygen permeation.

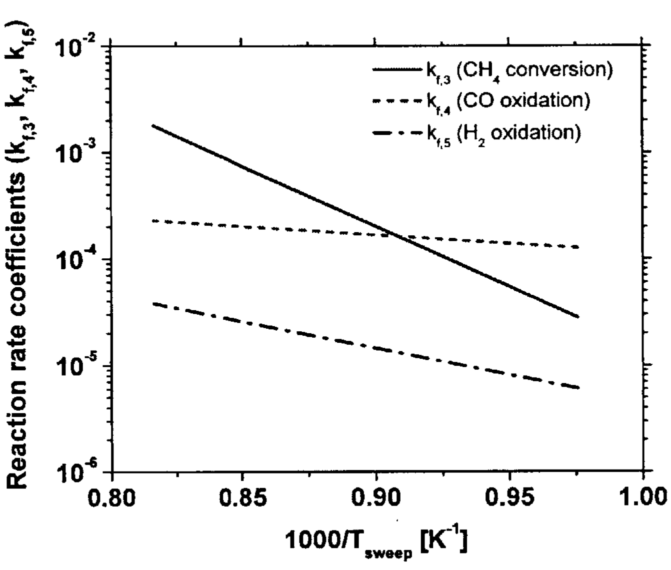

Figure 6-10 The kinetic parameters for catalytic fuel conversion estimated by the spatially resolved model ($k_{f,3}$ = CH_4 conversion reaction rate coefficient, $k_{f,4}$ = CO oxidation reaction rate coefficient, $k_{f,5}$ = H_2 oxidation reaction rate coefficient)

6.4. Local thermodynamic state

Heterogeneous chemistry parameters evaluated in this work are based on the local thermodynamic state at the membrane estimated by the spatially resolved physical model. The variables defining this state are difficult to measure experimentally and, at this point, can only be calculated using the model described here. When chemical reactions take place in the gas-phase and on the surface, the gas-phase species concentration and temperature measured outside the reactor can be substantially different from those in the immediate vicinity of the membrane. Thus, the spatially resolved physical model must be used to estimate the thermodynamic state and developing high fidelity heterogeneous chemistry. As shown in **Figure 6-11**, when the mass transfer in the gas-phase is substantial, the local thermodynamic state including species concentration and temperature varies significantly in the direction normal to the membrane, given the air and sweep gas inlet conditions considered when estimating the kinetic parameter of the oxygen surface exchange reactions (Section 6.3.1). As the temperature is raised, the gas-phase oxygen concentration varies more extensively throughout the air and sweep gas domain. These spatial variations in the thermodynamic state have also been observed experimentally, using a specially designated experimental ITM reactor [65]. The operating temperature of ITM reactors is nearly or above 900 °C, and hence the local species concentrations near the membrane could be significantly different from those measured outside the reactor.

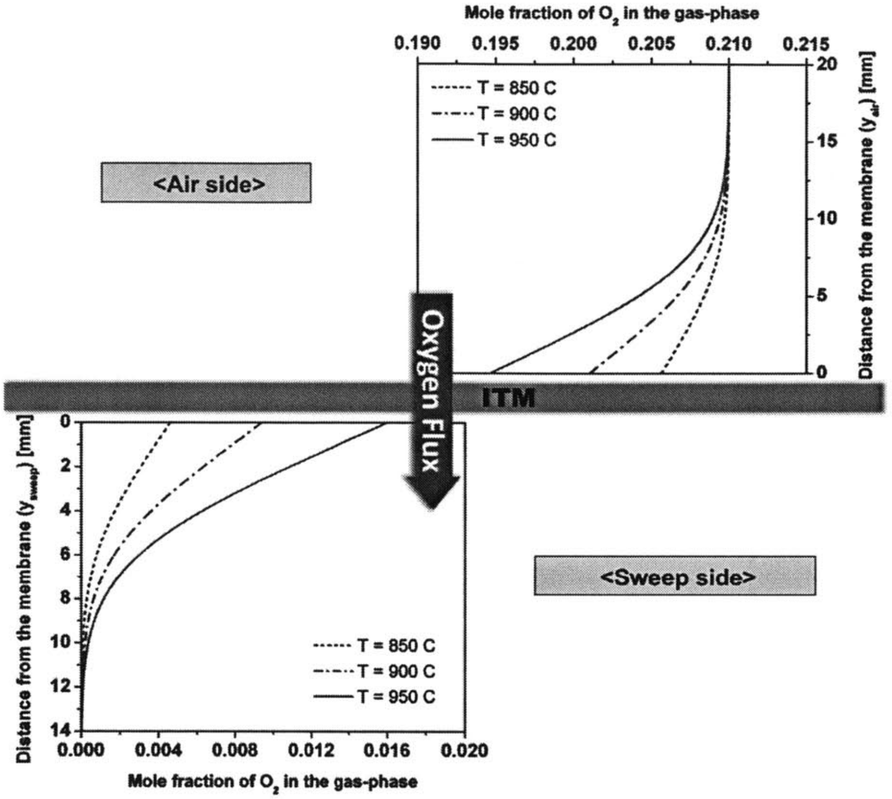

Figure 6-11 The spatially resolved gas-phase oxygen concentration in both sides of the membrane, given the air and sweep gas conditions considered in the estimation of the kinetic parameters for the oxygen surface exchange reactions

Figure 6-12 shows the bulk oxygen ion concentration and oxygen partial pressure near the membrane on the sweep side, along with the sweep gas inlet conditions, for the same conditions considered when evaluating the oxygen surface exchange kinetic parameters (Section 6.3.1) and catalytic fuel conversion (Section 6.3.2).

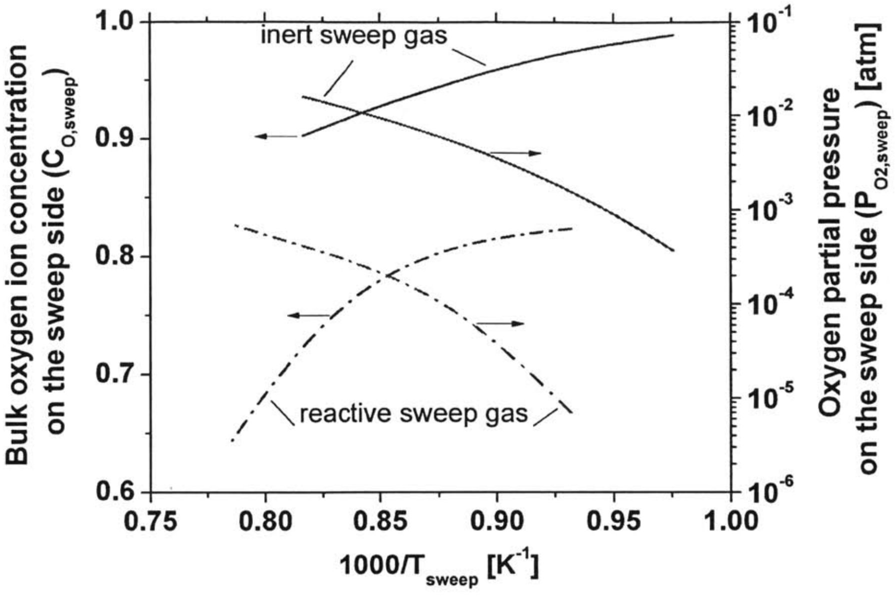

Figure 6-12 The bulk oxygen ion concentration and the oxygen partial pressure in the immediate vicinity of the membrane on the sweep side evaluated using the spatially resolved physical model given the sweep gas inlet conditions when an inert sweep gas [31] or a reactive sweep gas [106]

These results show that, when introducing a reactive sweep gas, the bulk oxygen ion on the sweep side is smaller than that of an inert sweep gas because catalytic fuel conversion consumes oxygen ions directly on the membrane surface. As discussed in Section 6.3, catalytic fuel conversion competes for oxygen ions with oxygen discharge to the gas-phase, which, coupled with gas-phase reactions, results in a lower oxygen partial pressure in the vicinity of the membrane. The results show that substantial differences in these local species concentrations between two conditions (i.e., inert sweep gas and reactive sweep gas), emphasizing the importance of considering the local thermodynamic state when modeling oxygen surface exchange and catalytic fuel conversion in the ITM reactor analysis.

6.5. Conclusions

Numerical simulations have been conducted to develop heterogeneous chemistry for a perovskite membrane in terms of the local thermodynamic state in the immediate neighborhood of the membrane and on its surface. In Chapter 2, I developed a spatially resolved physical model that resolves spatially the gas-phase flow, incorporates detailed homogeneous chemistry and accounts for oxygen permeation. In this chapter, this model is revised to incorporate heterogeneous chemistry on the membrane surface. The surface and bulk species and their reactions are coupled with the local thermodynamic state near the membrane in the gas phase. Using spatially averaged, i.e., reactor-level, measurements available in the literature, numerical simulations have been used to develop the heterogeneous chemistry that resolves both oxygen surface exchange and catalytic fuel conversion. A multi-step oxygen permeation mechanism is considered, which accounts for a sequence of bulk diffusion and surface exchange processes. While bulk diffusion is resolved by the charged-species transport, surface exchange processes are described by two rate-limiting reactions including dissociative adsorption/desorption and charge-transfer incorporation. In addition, I consider three surface reactions for methane, carbon monoxide and hydrogen oxidation reactions to describe the catalytic activity of perovskite membranes.

Oxygen surface exchange and catalytic fuel conversion are resolved by the local thermodynamic state including gas-phase, surface and bulk species concentrations and temperature, and rate-limiting reactions are elucidated. The reaction rates of heterogeneous chemistry are expressed and evaluated in terms of the local species concentrations and temperature near the membrane or on the membrane surface. We show that oxygen surface exchange is limited by dissociative adsorption/desorption of oxygen molecules onto/from the membrane surface. The estimated oxygen surface exchange reaction rates for LSCF fall in between the measured values for YSZ and LNO. In addition, while the catalytic conversion of methane to methyl radical governs the overall surface reactions at high temperature (> 850 °C), carbon monoxide oxidation on the membrane surface is dominant at lower temperature (< 850 °C). Given the experimental conditions, gas-phase reactions also play an important role, highlighting the importance of both homogeneous and heterogeneous chemistry. We conclude that the local thermodynamic state should be accounted for when constructing and examining heterogeneous chemistry, though it should be noted that there are only very limited studies considering the local thermodynamic state experimentally or numerically and that more work is needed. In addition, many of the kinetic rate parameters for the heterogeneous reactions presented in this work were inferred from permeation measurements obtained without knowledge of the local thermodynamic state (which was inferred using the numerical model). Thus, in addition to spatially resolved experimental characterization of the thermodynamic state within an ITM reactor, there is a need for a more direct characterization of the surface processes. This includes the experimental identification of the most relevant catalytic fuel conversion reactions over all operating regimes of an ITM reactor, as well as the parameterization of the associated rate expressions. Future work will consider both these needs.

Chapter 7 Conclusions

7.1. Summary

In this thesis, I examined the key features of oxygen permeation and fuel conversion processes within ITM reactors using numerical simulations for which an one-dimensional stagnation flow configuration is considered. The comprehensive physical model incorporates detailed chemistry and transport in the gas-phase, enabling us to obtain the spatially resolved profiles of species concentration, temperature, velocity and reaction rates. The model was first used to develop the oxygen permeation rate expression examined in terms of the local thermodynamic state in the immediate neighborhood of the membrane. Then, I investigated the influence of operating conditions on oxygen permeation, assuming an inert sweep gas introduced to the sweep side. Next, considering a reactive sweep gas such as methane, a homogeneous-phase reaction zone established on the sweep side of an ITM was characterized. In addition, the interactions between oxygen permeation and homogeneous-phase fuel oxidation reactions were examined. Moreover, the numerical model was used to obtain the kinetic parameters for heterogeneous oxygen surface exchange and catalytic fuel oxidation reactions on the membrane surface in terms of the local thermodynamic state in the immediate vicinity of or on the membrane surface.

The results from this study show that the local thermodynamic state should be considered when examining the oxygen permeation rate at the conditions relevant for ITM reactor operation. Given data on the thermodynamic state measured at the outside of the membrane facility, the oxygen permeation flux expression was parameterized in terms of the oxygen partial pressure near the membrane surface on both sides, which are estimated by the spatially resolved physical model. In comparison with the permeation rate evaluated by the species concentration measured at the outside of the membrane facility, the oxygen permeation flux calculated by this expression shows that the local thermodynamic state should be accounted for when constructing an oxygen transport model. It has been demonstrated that this is a more accurate and general representation that allows the application of the resulting expression over a wider range of conditions, in particular, at low sweep flow rate and high temperature, which is an operating regime of ITM reactors.

It is important to perform the detailed analysis with spatial resolutions to control hydrocarbon conversion processes in ITM reactors. The homogeneous-phase reaction zone established on the sweep side of the membrane features a laminar oxy-fuel non-premixed flame coupled with oxygen permeation. In such diffusion-supported reactions, the local thermodynamic state including species concentration and temperature play significant roles in establishing stable reactions and determining the reaction products. In addition, unlike typical diffusion-controlled combustion in which the temperature is so high that the overall hydrocarbon conversion rate is governed almost solely by diffusion, the temperature in an ITM reactor is kept low to protect the membrane, and hence chemical kinetics play an important role in determining the fuel conversion rate. In this regard, the spatially resolved physical model incorporating detailed chemistry and transport proposed in this study has elucidated the fuel conversion processes and captured the important features (e.g., the location, temperature, thickness and structure of a flame) of laminar oxy-fuel diffusion flames stabilized on the sweep side of an ITM.

To control and examine the permeation rate and the amount of fuel converted, the diffusion-controlled oxidation kinetics, the reactor geometry and mass and heat transfer have to be taken into account. When a reactive gas is employed on the sweep side of an ITM, the local thermodynamic state changes significantly between the membrane surface and the opposite wall or sweep gas inlet, through the variations of the dependent variables by influencing the chemical reactions and the energy and species transport. The local thermodynamic state is governed by the diffusion-controlled oxidation reactions and the mass and heat transfer in the gas-phase, and vice versa. Therefore, stream parameters measured at the outlet of an ITM reactor cannot predict correctly the thermodynamic state in the immediate vicinity of the membrane and hence the oxygen permeation rate in the case of an ITM reactor. A parametric study with respect to key operating conditions, which include the fuel concentration in the sweep gas, its temperature, flow rate and the geometry, elucidated the sweep side conditions at which substantial fuel conversion and oxygen permeation can be obtained attributed to homogeneous-phase chemical reactions. In addition, the conditions for which surface catalytic reactions along with homogeneous chemistry may play an important role on the sweep side of the membrane were examined.

The catalytic activity of perovskite membranes has been determined by the local thermodynamic state. The kinetic parameters for heterogeneous chemistry, which accounts for oxygen surface exchange and catalytic fuel conversion, have been obtained by using permeation rate measurements and the physical model. It has been shown that oxygen surface exchange is limited by dissociative adsorption/desorption of oxygen molecules onto/from the membrane surface. In addition, while the catalytic conversion of CH_4 to CH_3 governs the overall surface reactions at high temperature, CO oxidation on the membrane surface is dominant at low temperature. Given the sweep side conditions considered in ITM reactor experiments, gas-phase reactions also play an important role, indicating the importance of both homogeneous and heterogeneous chemistry and their coupling.

7.2. Future Work

7.2.1. Operating regimes (guidance for experiments)

Complex catalytic surface and gas-phase hydrocarbon conversion processes coupled with oxygen permeation require detailed analysis to elucidate feasible ITM reactor operating conditions and their effect on the fuel conversion and oxygen permeation rate. Since the oxygen permeation rate is not known a priori and rather depends on the local thermodynamic state of the membrane, i.e., oxygen concentration on both sides of the membrane and its temperature, hydrocarbon conversion reactions on the sweep side may alter the extent of oxygen permeation significantly, and vice versa. Whereas conventional catalytic reactors operate typically at low temperature, which reduces the chemical kinetic rates and results in negligible gas-phase reactions, a high temperature is required to yield oxygen permeation sufficient for fuel conversion processes. To enable oxygen permeation through the membrane, the temperature above 800 °C is required. When ITMs are employed for hydrocarbon conversion, a higher temperature of 800 ~ 1000 °C has been considered. In this high temperature regime, homogeneous-phase as well as catalytic surface reactions may play an important role in determining the extent of fuel conversion and the product selectivity. The coupling between homogeneous and heterogeneous fuel conversion and oxygen permeation is substantial. Therefore, to investigate ITM reactor operating regimes and control fuel conversion and oxygen permeation, the detailed numerical modeling work that accounts for the coupling of oxygen permeation and both homogeneous and heterogeneous chemistry is needed. This should be a good guiding map for experiments to follow.

7.2.2. Product selectivity

Product selectivity is one of key parameters that need to be controlled in ITM reactors. Although multiple applications including oxidative coupling, syngas production and oxy-fuel combustion have been proposed, what governs the product selectivity has not been addressed in detail. Since the oxygen permeation rate is not known a priori and rather depends on the local thermodynamic state, it is difficult to control or evaluate the product selectivity by experiments. To control the product selectivity and optimize ITM reactor operation, the reaction pathway analysis supported by detailed chemical kinetics and spatially resolved species concentration and temperature is necessary.

7.2.3. Radiation in the gas-phase

Gases introduced to the sweep side of the membrane could result in substantial radiation in the gas-phase. To control the reaction zone and membrane temperature, a large amount of diluents, such as carbon dioxide, is introduced to the sweep side along with a fuel. The diluents and fuel may contribute to radiative heat transfer, which changes the gas temperature and hence the reaction kinetics. Therefore, radiation in the gas-phase needs to be considered to see its effect on the overall heat transfer and fuel conversion processes.

Page left intentionally blank

References

1. DOE/NETL. *Cost and performance baseline for fossil energy plants, Volume 1: Bituminous coal and natural gas to electricity.* 2007, National Energy Technology Laboratory: Pittsburgh.
2. DOE/NETL. *Pulverized coal oxycombustion power plants, Volume 1: Bituminous coal to electricity.* 2007, National Energy Technology Laboratory: Pittsburgh.
3. B. Xu, R.A. Stobbs, V. White, R.A. Wall, J. Gibbins, M. Lijima, A. McKenzie. *Future CO_2 capture technology options for the Canadian market.* 2007, AEA Energy & Environment.
4. C.R. Bozzuto, N.Y. Nsakala, G.N. Liljedahl, M. Palkes, J.L. Marion, D. Vogel, J.C. Gupta, M. Fugate, M.K. Guha. *Engineering feasibility and economics of CO_2 capture on an existing coal-fired power plant, Volume 1: American electric power's conesville power plant unit No. 5 CO_2 capture retrofit study.* 2001, National Energy Technology Laboratory: Pittsburgh.
5. B. Metz, O. Davidson, H. Coninck, M. Loos, L. Meyer. *Carbon dioxide capture and storage.* 2005, IPCC: Cambridge, UK.
6. J. Hong, Master's thesis. Mechanical Engineering, Massachusetts Institute of Technology, (2009).
7. L. Chen, S.Z. Yong, A.F. Ghoniem, *Oxy-fuel combustion of pulverized coal: characterization, fundamentals, stabilization and CFD modeling,* Progress in Energy and Combustion Science, **38** (2) (2012) 156-214.
8. G.R. Wall T, Buhre B, Khare S, *Oxy-fuel (O_2/CO_2, O_2/RFG) technology for sequestration-ready CO_2 and emission compliance*, in *The Clearwater coal conference: the 30th international technical conference on coal utilization & fuel systems, coal technology: yesterday-today-tomorrow.* 2005: Clearwater USA.
9. IEA-Greenhouse-Gas-R&D-Program, *Improvement in power generation with post-combustion capture of CO_2,* **PH4/19** (2004).
10. Y. Hu, S. Naito, N. Kobayashi, M. Hasatani, *CO_2, NO_x and SO_2 emissions from the combustion of coal with high oxygen concentration gases,* Fuel, **79** (15) (2000) 1925-1932.
11. B.J.P. Buhre, L.K. Elliott, C.D. Sheng, R.P. Gupta, T.F. Wall, *Oxy-fuel combustion technology for coal-fired power generation,* Progress in Energy and Combustion Science, **31** (4) (2005) 283-307.
12. H.J.M. Bouwmeester, A.J. Burggraaf, *Fundamentals of inorganic membrane science and technology,* **Chapter 10: Dense ceramic membranes for oxygen separation** (1996).
13. B. Cales, J.F. Baumard, *Oxygen semipermeability and electronic conductivity in calcia-stabilized zirconia,* Journal of Materials Science, **17** (11) (1982) 3243-3248.
14. B. Cales, J.F. Baumard, *Mixed conduction and defect structure of ZrO_2-CeO_2-Y_2O_3 solid solutions,* Journal of the Electrochemical society, **131** (10) (1984) 2407-2413.
15. Y. Teraoka, T.N. Okamoto, K. Miura, N. Yamazoe, *Influence of constituent metal cations in substituted $LaCoO_3$ on mixed conductivity and oxygen permeability,* Solid State Ionics, **48** (3-4) (1991) 207-212.
16. Y. Teraoka, H.M. Zhang, S. Furukawa, N. Yamazoe, *Oxygen permeation through perovskite-type oxides,* Chemistry Letters, **11** (1985) 1743-1746.
17. Y. Teraoka, H.M. Zhang, S. Furukawa, N. Yamazoe, *Oxygen permeation through perovskite-type oxides,* Chemistry Letters, **14** (11) (1985) 1743.
18. Y. Teraoka, H.M. Zhang, K. Okamoto, N. Yamazoe, *Mixed ionic-electronic conductivity of $La_{1-x}Sr_xCo_{1-y}Fe_yO_{3-\delta}$ perovskite-type oxides,* Materials Research Bulletin, **23** (1) (1988) 51-58.
19. Y. Teraoka, H.M. Zhang, N. Yamazoe, *Oxygen-sorptive properties of defect perovskite-type $La_{1-x}Sr_xCo_{1-y}Fe_yO_{3-\delta}$,* Chemistry Letters, **9** (1985) 1367-1370.
20. A. Julbe, D. Farrusseng, C. Guizard, *Limitations and potentials of oxygen transport dense and porous ceramic membranes for oxidation reactions,* Catalysis Today, **104** (2-4) (2005) 102-113.

21. P.S. Manning, J.D. Sirman, J.A. Kilner, *Oxygen self-diffusion and surface exchange studies of oxide electrolytes having the fluorite structure,* Solid State Ionics, **93** (1-2) (1996) 125-132.
22. T. Ishihara, J.A. Kilner, M. Honda, N. Sakai, Y. Harumi, T. Yusaku, *Oxygen surface exchange and diffusion in $LaGaO_3$ based perovskite type oxides,* Solid State Ionics, **113-115** (1998) 593-600.
23. E. Ruiz-Trejo, J.D. Sirman, Y.M. Baikov, J.A. Kilner, *Oxygen ion diffusivity, surface exchange and ionic conductivity in single crystal Gadolinia doped Ceria,* Solid State Ionics, **113-115** (1998) 565-569.
24. J.A. Lane, J.A. Kilner, *Oxygen surface exchange on Gadolinia doped Ceria,* Solid State Ionics, **136-137** (2000) 927-932.
25. J. Fleig, *On the current-voltage characteristics of charge transfer reactions at mixed conducting electrodes on solid electrolytes,* Physical Chemistry Chemical Physics, **7** (2005) 2027-2037.
26. D.S. Mebane, M. Liu, *Classical, phenomenological analysis of the kinetics of reactions at the gas-exposed surface of mixed ionic electronic conductors,* Journal of Solid State Electrochemistry, **10** (8) (2006) 575-580.
27. S. Dou, C.R. Masson, P.D. Pacey, *Mechanism of oxygen permeation through lime-stabilized Zirconia,* Journal of the Electrochemical society, **132** (8) (1985) 1843-1849.
28. H.J.M. Bouwmeester, H. Kruidhof, A.J. Burggraaf, *Importance of the surface exchange kinetics as rate limiting step in oxygen permeation through mixed-conducting oxides,* Solid State Ionics, **72** (2) (1994) 185-194.
29. Y.S. Lin, W. Wang, J. Han, *Oxygen permeation through thin mixed-conducting solid oxide membranes,* AIChE Journal, **40** (5) (1994) 786-798.
30. J. Sunarso, S. Baumann, J.M. Serra, W.A. Meulenberg, S. Liu, Y.S. Lin, J.C. Diniz da Costa, *Mixed ionic-electronic conducting (MIEC) ceramic-based membranes for oxygen separation,* Journal of Materials Science, **320** (1-2) (2008) 13-41.
31. S.J. Xu, W.J. Thomson, *Oxygen permeation rate through ion-conducting perovskite membranes,* Chemical Engineering Science, **54** (17) (1999) 3839-3850.
32. L. Qiu, T.H. Lee, L.M. Liu, Y.L. Yang, A.J. Jacobson, *Oxygen permeation studies of $SrCo_{0.8}Fe_{0.2}O_{3-\delta}$,* Solid State Ionics, **76** (3-4) (1995) 321-329.
33. B.A. van Hassel, T. Kawada, N. Sakai, H. Yokokawa, M. Dokiya, H.J.M. Bouwmeester, *Oxygen permeation modelling of perovskites,* Solid State Ionics, **66** (3-4) (1993) 295-305.
34. X. Qi, Y.S. Lin, S.L. Swartz, *Electric transport and oxygen permeation properties of Lanthanum Cobaltite membranes synthesized by different methods,* Industrial & Engineering Chemistry Research, **39** (3) (2000) 646-653.
35. Z. Yang, Y.S. Lin, *A semi-empirical equation for oxygen nonstoichiometry of perovskite-type ceramics,* Solid State Ionics, **150** (3-4) (2002) 242-254.
36. S. Kim, Y.L. Yang, A.J. Jacobson, B. Abeles, *Diffusion and surface exchange coefficients in mixed ionic electronic conducting oxides from the pressure dependence of oxygen permeation,* Solid State Ionics, **106** (3-4) (1998) 189-195.
37. A. Leo, S. Liu, J.C. Diniz da Costa, *Development of mixed conducting membranes for clean coal energy delivery,* International Journal of Greenhouse Gas Control, **3** (4) (2009) 357-367.
38. G. Saracco, H.W.J.P. Heomagus, G.F. Versteeg, W.P.M. van Swaaij, *High-temperature membrane reactors: potential and problems,* Chemical Engineering Science, **54** (13-14) (1999) 1997-2017.
39. J.E. ten Elshof, H.J.M. Bouwmeester, H. Verweeij, *Oxidative coupling of methane in a mixed-conducting perovskite membrane reactor,* Applied Catalysis A: General, **130** (195-212) (1995).
40. X. Tan, K. Li, A. Thursfield, I.S. Metcalfe, *Oxyfuel combustion using a catalytic ceramic membrane reactor,* Catalysis Today, **131** (1-4) (2008) 292-304.
41. D. Lafarga, J. Santamaria, M. Menendez, *Methane oxidative coupling using porous ceramic membrane reactors. Part 1. Reactor development,* Chemical Engineering Science, **49** (1994) 2005-2013.

42. A.C. Bose, *Inorganic membranes for energy and environmental applications*, ed. A.C. Bose, Springer, Pittsburgh, 2009.

43. H. Wang, Y. Cong, W. Yang, *Oxidative coupling of methane in* $Ba_{0.5}Sr_{0.5}Co_{0.8}Fe_{0.2}O_{3-\delta}$ *membranes,* Catalysis Today, **104** (2-4) (2005) 160-167.

44. S. Bharadwaj, L.D. Schmidt, *Catalytic partial oxidation of natural gas to syngas,* Fuel Processing Technology, **42** (1995) 109-127.

45. U. Balachandran, J.T. Dusek, R.L. Mieville, R.B. Peoppel, M.S. Kleefisch, S. Pei, T.P. Kobylinski, C.A. Udovich, A.C. Bose, *Dense ceramic membranes for partial oxidation of methane to syngas,* Applied Catalysis A: General, **133** (19-29) (1995).

46. D.A. Hickman, L.D. Schmidt, *Synthesis gas formation by direct oxidation of methane over Pt monoliths,* Journal of Catalysis, **138** (1) (1992) 267-282.

47. D.A. Hickman, L.D. Schmidt, *Production of syngas by direct catalytic oxidation of methane,* Science, **259** (5093) (1993) 343-346.

48. A.P.E. York, T. Xiao, M.L.H. Green, *Brief overview of the partial oxidation of methane to synthesis gas,* Catalysis, **22** (3-4) (2003) 345-358.

49. R.W. Sidwell, H. Zhu, R.J. Kee, D.T. Wickham, *Catalytic combustion of premixed methane-in-air on a high-temperature hexaaluminate stagnation surface,* Combustion and Flame, **134** (2003) 55-66.

50. W. Jin, X. Gu, S. Li, P. Huang, N. Xu, J. Shi, *Experimental and simulation study on a catalyst packed tubular dense membrane reactor for partial oxidation of methane to syngas,* Chemical Engineering Science, **55** (14) (2000) 2617-2625.

51. W. Zhang, J. Smit, v.S. Annaland, J.A.M. Kuipers, *Feasibility study of a novel membrane reactor for syngas production, Part 1: Experimental study of* O_2 *permeation through perovskite membranes under reducing and non-reducing atmospheres,* Journal of Membrane Science, **291** (1-2) (2007) 19-32.

52. J. Smit, W. Zhang, v.S. Annaland, J.A.M. Kuipers, *Feasibility study of a novel membrane reactor for syngas production, Part 2: Adiabatic reactor simulations,* Journal of Membrane Science, **291** (1-2) (2007) 33-45.

53. X. Tan, K. Li, *Design of mixed conducting ceramic membranes/reactors for the partial oxidation of methane to syngas,* AIChE Journal, **55** (10) (2009) 2675-2685.

54. N.D. Mancini, A. Mitsos, *Ion transport membrane reactors for oxy-combustion - Part |: Intermediate-fidelity modelling,* Energy, **36** (8) (2011) 4701-4720.

55. N.D. Mancini, A. Mitsos, *Ion transport membrane reactors for oxy-combustion - Part ||: Analysis and comparison of alternatives,* Energy, **36** (8) (2011) 4721-4739.

56. F.T. Akin, J.Y.S. Lin, *Oxygen permeation through oxygen ionic or mixed-conducting ceramic membranes with chemical reactions,* Journal of Membrane Science, **231** (1-2) (2004) 133-146.

57. Z. Rui, Y. Li, Y.S. Lin, *Analysis of oxygen permeation through dense ceramic membranes with chemical reactions of finite rate,* Chemical Engineering Science, **64** (1) (2009) 172-179.

58. W. Wang, Y.S. Lin, *Analysis of oxidative coupling of methane in dense oxide membrane reactors,* Journal of Membrane Science, **103** (3) (1995) 219-233.

59. Z. Rui, K. Zhang, Y. Li, Y.S. Lin, *Simulation of methane conversion to syngas in a membrane reactor: Part I A model including product oxidation,* International Journal of Hydrogen Energy, **33** (9) (2008) 2246-2253.

60. Z. Rui, K. Zhang, Y. Li, Y.S. Lin, *Simulation of methane conversion to syngas in a membrane reactor. Part II Model predictions,* International Journal of Hydrogen Energy, **33** (10) (2008) 2501-2506.

61. Y. Liu, X. Tan, K. Li, *Mixed conducting ceramics for catalytic membrane processing,* Catalysis Reviews, **48** (2) (2006) 145-198.

62. T.V. Choudhary, S. Banerjee, V.R. Choudhary, *Catalysts for combustion of methane and lower alkanes,* Applied Catalysis A: General, **234** (1-2) (2002) 1-23.

63. R.J. Berger, G.B. Marin, *Investigation of gas-phase reactions and ignition delay occurring at*

conditions typical for partial oxidation of methane to synthesis gas, Industrial & Engineering Chemistry Research, **38** (7) (1999) 2582-2592.

64. B.C. Enger, R. Lodeng, A. Holmen, *A review of catalytic partial oxidation of methane to synthesis gas with emphasis on reaction mechanisms over transition metal catalysts,* Applied Catalysis A: General, **346** (1-2) (2008) 1-27.
65. P. Kirchen, D. Apo, A. Hunt, A.F. Ghoniem, *A novel ion transport membrane reactor for fundamental investigations of oxygen permeation and oxy-combustion under reactive flow conditions,* Proceedings of the Combustion Institute, **34** (2) (2013) 3463-3470.
66. Y.M. Marzouk, *The effect of flow and mixture inhomogeneity on the dynamics of strained flames,* Master's's thesis. Mechanical Engineering, Massachusetts Institute of Technology, (1997).
67. R.L. Speth, *Effects of curvature and strain on a lean premixed methane-hydrogen-air flame,* Master's's thesis. Mechanical Engineering, Massachusetts Institute of Technology, (2003).
68. H. Tsuji, *Counterflow diffusion flames,* Progress in Energy and Combustion Science, **8** (2) (1982) 93-119.
69. R.J. Kee, J.A. Miller, G.H. Evans, G. Dixon-Lewis, *A computational model of the structure and extinction of strained, opposed flow, premixed methane-air flames,* in *Proceedings of the Combustion Institute.* 1988: The Combustion Institute.
70. R. Ben-Mansour, M.A. Habib, M.A. Nemit-Allah, A.F. Ghoniem, P. Kirchen, J. Hong, *Oxygen separation and oxy-combustion in an ion-transfer membrane (ITM) reactor - Numerical modeling and simulation,* in *International Conference on Inorganic Membranes.* 2012. Enschede, the Netherlands.
71. R.J. Kee, M.E. Coltrin, P. Glarborg, *Chemically Reacting Flow: Theory & Practice,* Wiley-Interscience, 2003.
72. T.W. Chapman, G.L. Bauer, *Stagnation-point viscous flow of an incompressible fluid between porous plates with uniform blowing,* Applied Scientific Research, **31** (3) (1975) 223-239.
73. D. Apo, Master's thesis. Mechanical Engineering, Massachusetts Institute of Technology, (2011).
74. G.P. Smith, D.M. Golden, M. Frenklach, N.W. Moriarty, B. Eiteneer, M. Goldenberg, C.T. Bowman, R.K. Hanson, S. Song, W.C. Gardiner, V.V. Lissianski, Z. Qin. *GRI-Mech 3.0.* Available from: http://www.me.berkeley.edu/gri_mech/.
75. D.G. Goodwin. *Cantera.* Available from: http://www.aresinstitute.org/Cantera/cantera-cxx.pdf.
76. Lawrence-Livermore-National-Laboratory. *SUite of Nonlinear and DIfferential ALgebraic equation Solvers (SUNDIALS),* https://computation.llnl.gov/casc/sundials/main.html.
77. B.A. van Hassel, *Oxygen transfer across composite oxygen transport membranes,* Solid State Ionics, **174** (1-4) (2004) 253-260.
78. J.M. Gozalvez-Zafrilla, A. Santafe-Moros, S. Escolastico, J.M. Serra, *Fluid dynamic modeling of oxygen permeation through mixed ionic-electronic conducting membranes,* Journal of Membrane Science, **378** (1-2) (2011) 290-300.
79. M. Ikeguchi, T. Mimura, Y. Sekine, E. Kikuchi, M. Matsukata, *Reaction and oxygen permeation studies in* $Sm_{0.4}Ba_{0.6}Fe_{0.8}Co_{0.2}O_{3-\delta}$ *membrane reactor for partial oxidation of methane to syngas,* Applied Catalysis A: General, **290** (1-2) (2005) 212-220.
80. C. Tsai, A.G. Dixon, W.R. Moser, Y.H. Ma, *Dense perovskite membrane reactors for partial oxidation of methane to syngas,* AIChE Journal, **43** (11A) (1997) 2741-2750.
81. C.J. Sung, J.B. Liu, C.K. Law, *Structural response of counterflow diffusion flames to strain rate variations,* Combustion and Flame, **102** (4) (1995) 481-492.
82. J.R. Anderson, M. Boudart, *Catalysis: science and technology.* Vol. 5, Springer-Verlag, Berlin; New York, 1984.
83. J.G. McCarty, H. Wise, *Perovskite catalysts for methane combustion,* Catalysis Today, **8** (2) (1990) 231-248.
84. S. Engels, F. Beggel, M. Modigell, H. Stadler, *Simulation of a membrane unit for oxyfuel power*

plants under consideration of realistic BSCF membrane properties, Journal of Membrane Science, **359** (1-2) (2010) 93-101.

85. P. Glarborg, L.B. Bentzen, *Chemical effects of a high* CO_2 *concentration in oxy-fuel combustion of methane,* Energy & Fuels, **22** (1) (2008) 291-296.
86. S. Seepana, S. Jayanti, *Flame structure investigations of oxy-fuel combustion,* Fuel, **93** (2012) 52-58.
87. G. Dixon-Lewis, *Structure of laminar flames*, in *Proceedings of the Combustion Institute*. 1990: The Combustion Institute.
88. P. Popp, M. Baum, *Analysis of wall heat fluxes, reaction mechanisms, and unburnt hydrocarbons during the head-on quenching of a laminar methane flame,* Combustion and Flame, **108** (3) (1997) 327-348.
89. I.S. Wichman, *On diffusion flame attachment near cold surfaces,* Combustion and Flame, **117** (1-2) (1999) 384-393.
90. N. Peters, *Laminar flamelet concepts in turbulent combustion*, in *Proceedings of the Combustion Institute*. 1988: The Combustion Institute.
91. K. Seshadri, N. Peters, *Asymptotic structure and extinction of methane-air diffusion flames,* Combustion and Flame, **73** (1) (1988) 23-44.
92. S.R. Turns, *An introduction to combustion: concepts and applications*, 2nd ed, McGraw-Hill, Singapore, 2000.
93. K.T. Kang, J.Y. Hwang, S.H. Chung, *Soot zone structure and sooting limit in diffusion flames: comparison of counterflow and co-flow flames,* Combustion and Flame, **109** (1-2) (1997) 266-281.
94. D.X. Du, R.L. Axelbaum, C.K. Law, *The influence of carbon dioxide and oxygen as additives on soot formation in diffusion flames*, in *Proceedings of the Combustion Institute*. 1990: The Combustion Institute.
95. C. Zhang, A. Atreya, K. Lee, *Sooting structure of methane counterflow diffusion flames with preheated reactants and dilution by products of combustion*, in *Proceedings of the Combustion Institute*. 1992: The Combustion Institute.
96. M.C.J. Bradford, M.A. Vannice, CO_2 *reforming of* CH_4, Catalysis Reviews, **41** (1) (1999) 1-42.
97. M. Arnold, H. Wang, A. Feldhoff, *Influence of* CO_2 *on the oxygen permeation performance and the microstructure of perovskite-type* $(Ba_{0.5}Sr_{0.5})(CO_{0.8}Fe_{0.2})O_{3-\delta}$ *membranes,* Journal of Membrane Science, **293** (1-2) (2007) 44-52.
98. O. Czuprat, M. Arnold, S. Schirrmeister, T. Schiestel, J. Caro, *Influence of* CO_2 *on the oxygen permeation performance of perovskite-type* $BaCO_xFe_yZr_zO_{3-\delta}$ *hollow fiber membranes,* Journal of Membrane Science, **364** (1-2) (2010) 132-137.
99. Y.S. Lin, Y. Zeng, *Catalytic properties of oxygen semipermeable perovskite-type ceramic membrane materials for oxidative coupling of methane,* Journal of Catalysis, **164** (220-231) (1996).
100. Y. Zeng, Y.S. Lin, S.L. Swartz, *Perovskite-type ceramic membrane: synthesis, oxygen permeation and membrane reactor performance for oxidative coupling of methane,* Journal of Materials Science, **150** (1) (1998) 87-98.
101. S.J. Xu, W.J. Thomson, *Perovskite-type oxide membranes for the oxidative coupling of methane,* AIChE Journal, **43** (11A) (1997) 2731-2740.
102. X. Tan, Z. Pang, Z. Gu, S. Liu, *Catalytic perovskite hollow fibre membrane reactors for methane oxidative coupling,* Journal of Membrane Science, **302** (1-2) (2007) 109-114.
103. W. Jin, S. Li, P. Huang, N. Xu, J. Shi, Y.S. Lin, *Tubular lanthanum cobaltite perovskite-type membrane reactors for partial oxidaiton of methane to syngas,* Journal of Membrane Science, **166** (1) (2000) 13-22.
104. H.J.M. Bouwmeester, *Dense ceramic membranes for methane conversion,* Catalysis Today, **82** (1-4) (2003) 141-150.
105. J.E. ten Elshof, H.J.M. Bousmeester, H. Verweij, *Oxygen transport through* $La_{1-x}Sr_xFeO_{3-\delta}$ *membranes* ||. *Permeation in air/CO,* CO_2 *gradients,* Solid State Ionics, **89** (1-2) (1996) 81-92.

106. X. Tan, L. Shi, G. Hao, B. Meng, S. Liu, *$La_{0.7}Sr_{0.3}FeO_{3-\alpha}$ perovskite hollow fiber membranes for oxygen permeation and methane conversion,* Separation and Purification Technology, **96** (2012) 89-97.
107. O. Deutschmann, R. Schmidt, F. Behrendt, J. Warnatz, *Numerical modeling of catalytic ignition,* in *Proceedings of the Combustion Institute*. 1996.
108. L.L. Raja, R.J. Kee, L.R. Petzold, *Simulation of the transient, compressible, gas-dynamic behavior of catalytic-combustion ignition in stagnation flows*, in *Proceedings of the Combustion Institute*. 1998.
109. D.G. Goodwin, H. Zhu, A.M. Colclasure, R.J. Kee, *Modeling electrochemical oxidation of hydrogen on Ni-YSZ pattern anodes,* Journal of the Electrochemical Society, **156** (9) (2009) B1004-B1021.
110. B.A. Boukamp, K.J. de Vries, A.J. Burggraaf, *Non-stoichiometric compounds, surfaces, grainboundaries and structural defects*, ed. J. Nowotny and W. Weppner, Kluwer, 1989.
111. B.A. Boukamp, H. Verweij, A.J. Burggraaf, *Solid State Ionics* III, ed. G.A. Nazri, J.M. Tarascon, and M. Armand, Materials Research Society, 1993.
112. H.J.M. Bousmeester, C. Song, J. Zhu, J. Yi, M. van Sint Annaland, B.A. Boukamp, *A novel pulse isotopic exchange technique for rapid determination of the oxygen surface exchange rate of oxide ion conductors,* Physical Chemistry Chemical Physics, **11** (42) (2009) 9640-9643.
113. B.A. van Hassel, J.E. ten Elshof, H.J.M. Bouwmeester, *Oxygen permeation flux through $La_{1-y}Sr_yFeO_3$ limited by carbon monoxide oxidation rate,* Applied Catalysis A: General, **119** (2) (1994) 279-291.